Muon stopping sites in magnetic systems from density functional theory

HUDDART, BENJAMIN,MICHAEL

Muon stopping sites in magnetic systems from density functional theory

Benjamin Michael Huddart

A thesis presented for the degree of
Doctor of Philosophy

Department of Physics
Durham University
United Kingdom

January 2020

Muon stopping sites in magnetic systems from density functional theory

Benjamin Michael Huddart

Abstract

This thesis concerns the use of density functional theory (DFT) to determine muon stopping sites in crystalline solids. New tools for carrying out these calculations are introduced and these techniques are demonstrated through the results of calculations on the skyrmion-hosting semiconductors GaV_4S_8 and GaV_4S_8 and the heavy-fermion metals URu_2Si_2 and $CeRu_2Si_2$. The results of three studies on significantly different magnetic systems are presented, where in each case the interpretation of the results of muon-spin spectroscopy (μ^+SR) experiments is aided by knowledge of the muon site.

The results of μ^+SR measurements on the iron-pnictide compound FeCrAs are presented and indicate a magnetically ordered phase throughout the material below $T_N = 105(5)$ K. There are signs of fluctuating magnetism in a narrow range of temperatures above T_N involving low-energy excitations, while at temperatures well below T_N a characteristic freezing of dynamics is observed. Using DFT, a distinct muon stopping site is proposed for this system.

The results of transverse-field (TF) μ^+SR measurements on the molecular spin ladder compound $(Hpip)_2CuBr_4$, [Hpip=$(C_5H_{12}N)$] are reported. Characteristic behaviour in each of the regions of the phase diagram is identified in the TF μ^+SR spectra. Analysis of the muon stopping sites, calculated using DFT, suggests that the muon plus its local distortion can lead to a local probe unit with good sensitivity to the magnetic state.

Finally, the results of μ^+SR measurements on the charge density wave system 1T-TaS_2 are presented, which show three distinct phases versus temperature. The critical exponents for each of these phases are compared with the predictions of quantum spin liquid models. Using DFT, a quantum delocalised state for the muon between the TaS_2 layers is proposed, which is used in conjunction with its associated hyperfine interactions to determine the coupling of the muon to the diffusing spinons.

Declaration

The work in this thesis is based on research carried out in the Department of Physics, Durham University, UK. No part of this thesis has been submitted elsewhere for any other degree or qualification and it is all my own work unless referenced to the contrary in the text.

Publications

- K. J. A. Franke, **B. M. Huddart**, T. J. Hicken, F. Xiao, S. J. Blundell, F. L. Pratt, M. Crisanti, J. A. T. Barker, S. J. Clark, A. Štefančič, M. C. Hatnean, G. Balakrishnan and T. Lancaster. "Magnetic phases of skyrmion-hosting $GaV_4S_{8-y}Se_y$ (y = 0, 2, 4, 8) probed with muon spectroscopy". *Phys. Rev. B*, **98**, 054428 (2018).

- T. Lancaster, F. Xiao, **B. M. Huddart**, R. C. Williams, F. L. Pratt, S. J. Blundell, S. J. Clark, R. Scheuermann, T. Goko, S. Ward, J. L. Manson, Ch. Rüegg and K. W. Krämer. "Quantum magnetism in molecular spin ladders probed with muon-spin spectroscopy". *New J. Phys.*, **20**, 103002 (2018).

- A. Štefančič, S. H. Moody, T. J. Hicken, M. T. Birch, G. Balakrishnan, S. A. Barnett, M. Crisanti, J. S. O. Evans, S. J. R. Holt, K. J. A. Franke, P. D. Hatton, **B. M. Huddart**, M. R. Lees, F. L. Pratt, C. C. Tang, M. N. Wilson, F. Xiao and T. Lancaster. "Origin of skyrmion lattice phase splitting in Zn-substituted Cu_2OSeO_3". *Phys. Rev. Materials*, **2**, 111402(R) (2018).

- **B. M. Huddart**, J. Brambleby, T. Lancaster, P. A. Goddard, F. Xiao, S. J. Blundell, F. L. Pratt, J. Singleton, P. Macchi, R. Scatena, A. M. Barton and J. L. Manson. "Magnetic order and enhanced exchange in the quasi-one-dimensional molecule-based antiferromagnet $Cu(NO_3)_2(pyz)_3$". *Phys. Chem. Chem. Phys.*, **21**, 1014-1018 (2019).

- **B. M. Huddart**, M. T. Birch, F. L. Pratt, S. J. Blundell, D. G. Porter, S. J. Clark, W. Wu, S. R. Julian, P. D. Hatton and T. Lancaster. "Local magnetism, magnetic order and spin freezing in the 'nonmetallic metal' FeCrAs". *J. Phys.: Condens. Matter*, **31**, 285803 (2019).

- T. Lancaster, **B. M. Huddart**, R. C. Williams, F. Xiao, K. J. A. Franke, P. J. Baker, F. L. Pratt, S. J. Blundell, J. A. Schlueter, M. B. Mills, A. C. Maahs and K. E. Preuss. "Probing magnetic order and disorder in the one-dimensional molecular spin chains CuF_2(pyz) and $[Ln(\text{hfac})_3(\text{boaDTDA})]_n$ (Ln=Sm, La) using implanted muons". *J. Phys.: Condens. Matter*, **31**, 394002 (2019).

Acknowledgements

Thoughout my PhD, I have been priveleged to work closely with all three members of my supervisory team and have learned a great deal from each of them. I would first like to thank my primary supervisor Tom Lancaster for his guidance and continued enthusiasm for my research. I attribute much of my growth as a scientist to his encouragement, support and insightful feedback. The computational aspects of my research owe much to Stewart Clark and I thank him for his assistance in running CASTEP calculations and for providing invaluable programming advice. I have also enjoyed working with Francis Pratt, who has helped me expand my research interests to explore new and exciting areas.

I have been fortunate to work alongside excellent scientists in the Durham muon group: Thomas Hicken, Matjaž Gomilšek, Murray Wilson and Kévin Franke. Much of the progress made during my PhD resulted from fruitful discussions and collaborations with these colleagues and I have enjoyed our many enlightening conversations during beamtimes. Also in Durham, I thank Nikitas Gidopoulos for many interesting discussions about electronic structure. Further afield, I thank Stephen Blundell, from whom I have learned a great deal about muons and magnetism.

The experimental work presented in this thesis was carried out at the ISIS neutron and muon source and the Paul Scherrer Institute and I have benefitted greatly from the expert assistance of the instrument scientists at both of these facilities. I am particularly grateful to the ISIS muon group, who made me feel very welcome during my year spent based at the facility.

I have enjoyed a friendly and lively office environment while at Durham and thank Tim Callow, Tom Pitts, Ben Pearce and Zachary Hawkhead for many stimulating discussions about physics and beyond. I also thank my parents for their continued

support throughout my education and career.

Finally, I am grateful to St. Mary's College and the IOP for financial support towards attending conferences and thank STFC and Durham University Faculty of Science for funding my studentship.

Contents

Chapter 1

Introduction

After its growth from a method of applied particle physics practised by a small number of specialists, muon spectroscopy (μ^+SR) has become a mainstream technique in condensed matter physics [1]. However, questions are still raised by our lack of knowledge of the site of the stopped muon and the influence that the muon-probe has on its local environment. Interpretation of μ^+SR results is often hindered by the lack of knowledge of the muon stopping site. Muons act as a local probe of magnetic fields, allowing us to determine the magnetic properties of a variety of condensed matter systems. However, to obtain quantitative information about the magnetic structure and moment sizes in the material, one often needs to be able to identify the muon stopping site. Furthermore, concerns are often raised about the effect of the implanted muon on the local structure of the host material. As a positively charged defect, one might expect that the presence of the muon results in crystallographic or electronic distortions that modify the magnetism observed as compared with magnetic behaviour intrinsic to the material itself.

It is now possible to accurately determine the muon stopping site and its associated distortion to the crystal structure using density functional theory (DFT) [2]. This thesis aims to develop these techniques further, by applying them to systems relevant to our experimental μ^+SR programme. The next two chapters are introductory and concern μ^+SR and DFT, respectively. I then summarise the recent progress made in calculating muon sites using DFT and present my contributions to this research area, both in terms of the development of new tools and methods and

in the application of these techniques. Following this, the next three chapters each comprise an in-depth study of a novel magnetic system, where in each case μ^+SR measurements are supported by knowledge of the muon site, determined using DFT.

1.1 Layout of thesis

This thesis is organised as follows:

Chapter 2: I introduce the muon-spin spectroscopy (μ^+SR) experimental technique. I outline the experimental procedure and describe polarisation functions arising from commonly-encountered magnetic field distributions. Practical application of the technique is demonstrated using a case study on the molecular magnet $Cu(NO_3)_2(pyz)_3$.

Chapter 3: I review the theoretical foundations of density functional theory (DFT) and then focus on the considerations for practical calculations.

Chapter 4: I review the application of DFT in calculating muon stopping sites (DFT+μ) and introduce MuFinder, a program I have developed to help non-experts carry out these calculations. I demonstrate the DFT+μ method with two examples, each comprising a pair of isostructural compounds: the skyrmion-hosting systems GaV_4S_8 and GaV_4Se_8 and the heavy-fermion systems URu_2Si_2 and $CeRu_2Si_2$.

Chapter 5: I report the results of μ^+SR measurements and muon site calculations on the 'nonmetallic metal' FeCrAs. A single crystallographically distinct stopping site is proposed, with the structural distortions induced by the implanted muon at this site being minimal, suggesting that the muon remains a faithful probe of the magnetism in this system.

Chapter 6: I report the results of μ^+SR measurements on the molecular spin ladder compound $(Hpip)_2CuBr_4$, where features in the μ^+SR spectra correlate with the previously-determined phase diagram of this material. DFT calculations of the muon stopping site, in conjunction with dipolar field calculations, suggest that the sensitivity of the muon to the different phases derives from a local distortion it makes

to the crystal structure in its vicinity.

Chapter 7: I report the results of a μ^+SR study on the charge density wave system 1T-TaS_2 that found three distinct phases versus temperature, whose critical exponents are compared with those predicted by quantum spin liquid models. DFT calculations suggest the formation of a quantum delocalised state for the muon between the TaS_2 layers that provides sensitivity to the unpaired spins in two adjacent layers.

Chapter 8: The thesis is summarised and I discuss future avenues for the development and application of muon site calculations.

Chapter 2

Muon-spin spectroscopy

In this chapter I introduce the muon-spin spectroscopy (μ^+SR) technique that is the focus of this thesis. I summarise the properties of the muon that allow it to function as a probe of magnetism, namely the phenomenon of spin precession and the parity violating nature of muon decay. I then outline the experimental procedure that allows the time evolution of the spin polarisation of the muon ensemble to be followed, through the measurement of the asymmetry of the positrons emitted when the muons decay. I describe polarisation functions appropriate for several static and dynamic magnetic field distributions, which allow magnetic properties of the sample to be inferred from the asymmetry. Finally, I demonstrate how the μ^+SR technique is applied in practice, by reporting the results of measurements on the quasi-one-dimensional Heisenberg molecule-based antiferromagnet $Cu(NO_3)_2(pyz)_3$.

2.1 Introduction

The realisation that the muon, discovered as a constituent of cosmic rays in 1936 [3, 4], was a heavy version of the electron and not the particle predicted by Yukawa [5] to be mediatior of the strong force was so unexpected that it led the Nobel laureate I. I. Rabi to famously quip "who ordered that?". While this question was likely rhetorical, it could be justifiably answered "condensed matter physicists", as the muon has since proved to be a highly effective probe of magnetism, superconductivity and molecular dynamics [1]. This application was first hinted at by Garwin *et*

al. [6], whose seminal paper detailing the parity violating nature of muon decay concluded with the remark "it seems possible that polarized positive and negative muons will become a powerfool tool for exploring magnetic fields in nuclei, atoms and interatomic regions". In fact, the work of Garwin *et al.* [6] could be considered the first muon-spin spectroscopy experiment, where spin-polarised muons are implanted into a solid sample and the angular distribution of the emitted positrons followed, with the sample in this case being an eight inch-thick block of carbon.

Muon-spin spectroscopy (μ^+SR) is an experimental technique where the spin of the muon allows it act as a local probe of the magnetic fields in condensed matter. The measured quantity is the asymmetry in the angular distribution of the positrons emitted when the muon decays. The acryonym μ^+SR can stand for muon-spin *relaxation*, *rotation* or *resonance*. The use of μ^+ emphasises the fact that for experiments in condensed matter physics it is mainly the positive muon that is used (though there have been developments in the use of the negative muons for elemental analysis [7]). *Relaxation* refers to cases where spatially or temporally varying distributions of fields lead to a depolarisation of the muon spin ensemble. In a muon-spin *rotation* experiment the muon spin is rotated about an externally applied magnetic field, with this precession modulated by any internal fields present in the sample. *Resonance* can refer to the application of radio-frequency (RF) electromagnetic waves [8] or to the avoided level crossing (ALC) technique [9, 10], but is not discussed further in this thesis.

As a local probe of magnetism, μ^+SR can provide similar information to techniques such electron spin resonance (ESR), nuclear magnetic resonance (NMR) and Mössbauer spectroscopy. However, unlike these resonance techniques, no electromagnetic field is necessary for μ^+SR since the precessing muon can be followed directly. This makes μ^+SR a valuable tool for studying the zero-field magnetic structure of a system. The very large magnetic moment of the muon makes it highly sensitive to extremely small magnetic fields and thus very useful for the study of small moment magnetism (such as in molecular magnets as discussed in Section 2.7). Other areas where μ^+SR has enjoyed great success include the study of the vortex lattice in the mixed phase of type II superconductors [11] and the study of the be-

haviour of isolated hydrogen impurities in semiconductors [12], where the muon acts as an experimentally accessible analogue of a proton.

2.2 Basic principles

The viability of the μ^+SR technique relies crucially on two phenomena: the precession of a spin in a magnetic field and the parity-violating nature of muon production and decay. In this section I review the properties of the muon that allow it to function as an effective probe of magnetism. Muons are part of the second generation of leptons and are therefore $S = 1/2$ elementary particles. In μ^+SR, we use positive muons rather than negative due to their affinity for regions of high electron density (which are the most interesting for studies of magnetism and related phenomena) and, unlike for negative muons, they do not undergo muon capture (which would lead to a sample-dependent lifetime). While fundamentally a heavier version of the positron with mass $m_\mu = 105.7$ MeV $\approx 207 m_\mathrm{e}$, positive muons in condensed matter behave much like light protons with mass $m_\mu \approx m_\mathrm{p}/9$ and it is often helpful to think of them as such.

Possessing both a charge and a spin, a muon carries a magnetic moment [13]

$$\boldsymbol{m} = \gamma_\mu \boldsymbol{S}, \tag{2.1}$$

where $\boldsymbol{S}$ is the muon's spin angular momentum and γ_μ is the muon gyromagnetic ratio ($= 2\pi \times 135.5$ MHz T^{-1}). From classical electromagnetism [14], we know that a magnetic moment experiences a torque

$$\boldsymbol{G} = \boldsymbol{m} \times \boldsymbol{B} \tag{2.2}$$

when it is placed it a magnetic field $\boldsymbol{B}$. Such a torque will result in a change in the muon's angular momentum. Substituting (2.1) into (2.2) one obtains

$$\frac{\mathrm{d}\boldsymbol{S}}{\mathrm{d}t} = \gamma_\mu \boldsymbol{S} \times \boldsymbol{B}. \tag{2.3}$$

Thus in the presence of a magnetic field, the direction of the muon spin will precess about the field $\boldsymbol{B}$. The precession frequency ν is related to the magnitude of the

magnetic field at the muon site through $\nu = \gamma_\mu B/2\pi$. Though the preceding treatment has been classical and not strictly valid for the quantum mechanical muon, a full quantum mechanical analysis (presented in Section 2.6.1) produces identical results. Thus the strength of the magnetic field at the muon site can be obtained from precession frequency of the muon spin.

How do we then know in what direction the muon's spin is pointing? The answer lies in the fact the muon is unstable, with an average lifetime $\tau = 2.2$ μs. The muon decays into a positron via the weak interaction which is known to be parity violating [15, 16]; the positron is emitted preferentially in the instantaneous direction of the muon's spin. Hence, for an ensemble of muons, measurement of the angular distribution of the emitted positrons allows the spin-polarisation of the muon ensemble to be inferred. Thus, by implanting spin-polarised muons into condensed matter and measuring the time dependence of the angular distribution of the emitted positrons, we can obtain information about the magnetic field at the muon site. In the next section I outline the experimental procedure that allows this to be accomplished.

2.3 Experimental procedure

High energy proton beams (produced using a synchrotron or cyclotron) are fired into a graphite target to produce pions via $p + p \rightarrow \pi^+ + p + n$ [17, 18] and these pions decay into muons through $\pi^+ \rightarrow \mu^+ + \nu_\mu$, where ν_μ is a muon neutrino. The pion is a spin-zero particle and hence to conserve angular momentum the muon and neutrino must have opposite spins. The neutrino has negative helicity and therefore its spin is aligned antiparallel to its momentum [19]. As a two-body decay with zero spin in the initial state, the same must hold true for the muon. Hence by selecting pions which stop in the target (and are therefore at rest when they decay), beams of 100% spin-polarised muons can be produced.

These spin-polarised muons are steered towards and focussed on the target sample using dipolar and quadupolar magnets respectively. The muons then implant in the sample, losing their energy (initially ≈ 4.1 MeV) through a series of scattering,

ionisation and electron capture processes [20]. Crucially, all of these processes are Coulombic in origin, thus not interacting with the muon's spin, and occur on the nanosecond time scale such that the polarisation of the muon ensemble remains almost unchanged throughout the entirety of the stopping process. Furthermore, the energy barrier for vacancy production is high enough that muons retain sufficient energy to propagate a further few μm after dropping below this threshold [20, 21], such that the environment of the stopped muon will not show any effects of radiation damage. The implanted muon either forms a diamagnetic μ^+ state or captures an electron and forms a paramagnetic muonium state. Samples are typically sealed in an envelope of silver foil (with foil of thickness 12.5 μm or 25 μm typically used) and mounted on a silver backing plate. Silver is used because it diamagnetic (it has no electronic moment) and hence muons stopping outside of the sample will contribute only a slowly relaxing background signal. Additional sheets of silver may be placed in front of the sample to act as a degrader in which incident muons lose some of their kinetic energy. This can be useful for thin samples, where the total thickness of the degrader can be tuned to maximise the number of muons stopping in the sample. For small or weakly magnetic samples the background signal can be further reduced by using the *fly-past* geometry where the silver envelope is mounted on a fork such that muons not implanting in the sample are removed from the experiment.

A schematic diagram of a μ^+SR experiment is shown in Figure 2.1(a). Muons are implanted in the sample with their spins antiparallel to the muon momentum. In the presence of a magnetic field, the muon spin will precess about the total magnetic field $\boldsymbol{B}$ at the muon site with the precession frequency proportional to the magnitude of this field. The muon spins precess while inside the sample where they decay with a characteristic lifetime $\tau = 2.2$ μs into a positron, a neutrino and an antineutrion via $\mu^+ \rightarrow e^+ + \nu_e + \bar{\nu}_\mu$. This decay proceeds via the weak interaction and is therefore parity violating; the positron is emitted preferentially in the direction of the muon spin [6]. As shown in Figure 2.1(b), the probability of a positron with energy ϵ being emitted at an angle θ to the direction of the muon spin is given by $W(\epsilon, \theta) \propto 1 + a(\epsilon)\cos\theta$, where $a(\epsilon)$ increases monotonically with energy up to $a = 1$ for the maximum possible positron energy $E_{\text{max}} = 52.8$ MeV [8].

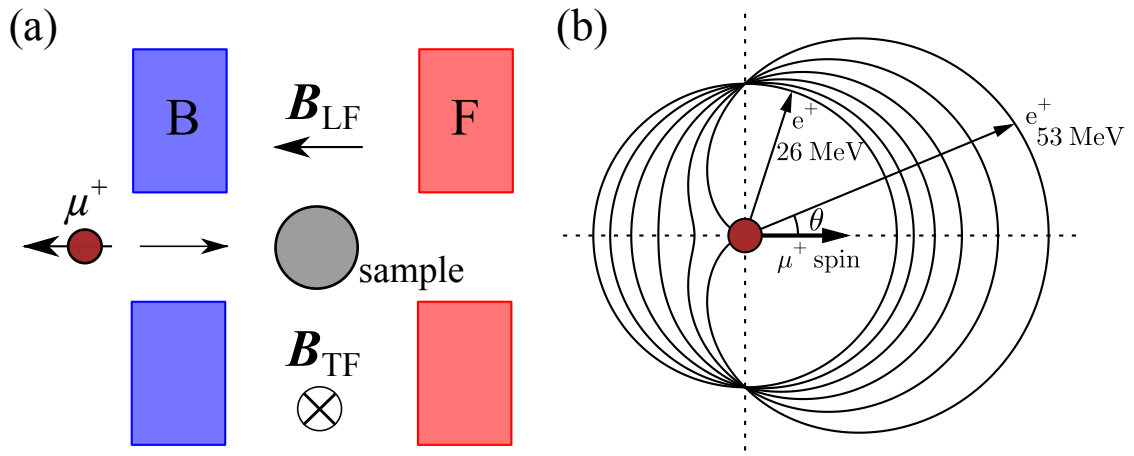

Figure 2.1: (a) A schematic of the experimental setup showing a muon entering the sample, situated between the forward detector F and the backward detector B. Also indicated are the directions of the applied magnetic field for the geometries. (b) The angular probability distribution $W(\epsilon, \theta)$ for decay positrons emitted with kinetic energies between $E_{\max}/2$ and $E_{\max}$.

The emitted positrons are detected by either the forward or backward detector, generating histograms $N_{\mathrm{F}}(t)$ and $N_{\mathrm{B}}(t)$ respectively. The quantity of interest is the asymmetry

$$A(t) = \frac{N_{\mathrm{B}}(t) - \alpha N_{\mathrm{F}}(t)}{N_{\mathrm{B}}(t) + \alpha N_{\mathrm{F}}(t)}, \tag{2.4}$$

where the experimental calibration constant α accounts for the relative efficiency of the detectors and differences in detector geometries in the two directions. The decay position asymmetry is proportional to the muon spin polarisation, i.e. $A(t) = a_0 P(t)$. In the ideal case, a_0 is obtained from the averaging of $a(\epsilon)$ over all possible positron energies, which gives $a_0 = \langle a \rangle = 1/3$. In practice, a_0 is reduced from this value by a number of factors, including incomplete solid angle coverage of the detectors, the efficiency of the detectors for positrons of different energies and the curved trajectories of postrons in magnetic fields, such that initial asymmetries of $\approx 25\%$ are typically achieved [22].

2.4 Time scales in μ^+SR

One of the most advantageous features of the μ^+SR technique is the magnitudes of magnetic fields and the time scale of magnetic fluctuations to which the muon is sensitive. These are dictated the muon's lifetime $\tau = 2.2$ μs and its gyromagnetic ratio $\gamma_\mu = 2\pi \times 135.5$ MHz T^{-1}, as well as the type of source used to produce the protons (and hence the muons) for the experiment. Protons produced using a synchroton generate a pulsed beam of muons (such as at the ISIS pulsed muon source at Rutherford Appleton Laboratory, UK), whereas those produced using a cyclotron result in a continuous beam of muons [such as at the Swiss muon source (SμS) at the Paul Scherrer Institut (PSI) in Villigen, Switzerland].

In a continuous source, a timer starts when a muon reaches the sample and stops when a decay positron is detected; this constitutes a single event. In order to unambiguously assign the positron detection time to the corresponding muon implantation time, only one muon can be in the sample at a time. This limits the count rate and time window for positron detection, which places an upper limit of around 10 μs on data collection. The upper limit of measurable fields is set by the instrument time resolution and the muon's gyromagnetic ratio. The source at PSI has a time resolution of 1 ns, corresponding to magnetic fields of around 10 T.

In a pulsed muon source, muons arrive in narrow pulses that are well separated compared with the muon lifetime. Pulses at ISIS have a FWHM of around 80 ns, which is significantly shorter than the muon lifetime of 2.2 μs. The high intensity of each pulse means that asymmetry data can be measured out to much longer times; the ISIS time window is 32 μs (the count rate is in fact limited by the detector dead time, the minimum time between the arrival of successive positron arrivals for them to be resolvable). The long time window makes pulsed sources well suited to studying slow dynamics. By considering the fact that muon spin precesses by an angle $\gamma_\mu Bt$ in time t and since an angle of 0.5 rad is measurable ($\cos 0.5 \approx 0.88$), it can be seen that this time window allows local fields as small as 0.04 mT to be detected [23]. The finite width of the pulse limits the temporal resolution compared with a continuous source. For measurements made at ISIS, the frequency resolution

of 10 MHz sets an upper limit of $\approx$ 10 mT on the magnitude of measurable fields.

μ^+SR is therefore sensitive to magnetic fields between 0.04 mT and 10 T and magnetic fluctuations with frequencies 10^4–10^{12} Hz [8]. Sensitivity to this wide range of fields and frequencies is not achievable within any single experiment, but instead represents those that are accessible given the appropriate type of source and experimental setup. Thus, μ^+SR measurements made at a continuous source and a pulsed source are often complementary, as they each allow the study of fields and fluctuations towards either end of these ranges. The time scale of magnetic fluctuations that can be probed by the muon makes μ^+SR complementary to other techniques such as neutrons (10^8–10^{13} Hz), NMR (10^{-2}–10^5 Hz) and ac susceptibility (10^0–10^4 Hz) [8].

2.5 Magnetic field at the muon site

The local magnetic field $\boldsymbol{B}$ at the muon site $\boldsymbol{r}_\mu$ is the vector sum of of the magnetic field arising from various sources [23, 8]

$$\boldsymbol{B} = \boldsymbol{B}_0 + \boldsymbol{B}_{\text{dia}} + \boldsymbol{B}_{\text{con}} + \boldsymbol{B}_{\text{trans}} + \boldsymbol{B}_{\text{dip}} + \boldsymbol{B}_{\text{L}} + \boldsymbol{B}_{\text{dem}}. \tag{2.5}$$

The origins of the first four terms are also follows:

- The field $\boldsymbol{B}_0 = \mu_0 \boldsymbol{H}_0$ is due to the externally applied field.
- The diamagnetic field $\boldsymbol{B}_{\text{dia}}$ is due to screening currents in superconductors.
- $\boldsymbol{B}_{\text{con}}$ is the contact hyperfine field resulting from the spin density at the muon site which is induced by the polarisation of the conduction electrons.
- $\boldsymbol{B}_{\text{trans}}$ is the transferred hyperfine field due to the Ruderman-Kittel-Kasuya-Yosida (RKKY) interaction [24, 25, 26] in metals.

The final three terms are due to the dipolar interaction between the muon spin and the lattice of localised magnetic moments. The total field due to these dipolar interactions is given by

$$\boldsymbol{B}'_{\text{dip}} = \frac{\mu_0}{4\pi} \sum_{i=1}^{N} \left[\frac{3(\boldsymbol{m}_i \cdot \boldsymbol{r}_i)\boldsymbol{r}_i}{r_i^5} - \frac{\boldsymbol{m}_i}{r_i^3} \right], \tag{2.6}$$

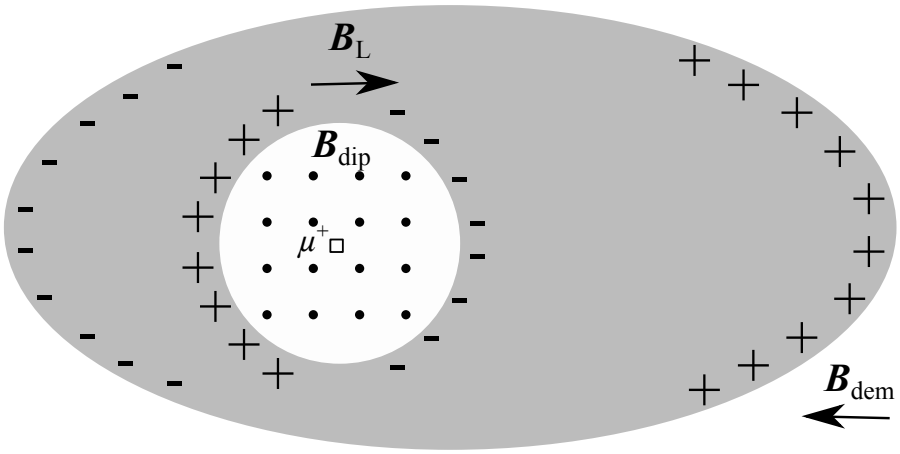

Figure 2.2: A schematic illustrating how dipolar fields at the muon site can be calculated using the Lorentz sphere method, with the sample represented by an ellipsoid. $\boldsymbol{B}_{\mathrm{dip}}$ is the dipolar field at the muon site due to only those moments lying inside the Lorentz sphere. Moments outside the Lorentz sphere give rise to macroscopic fields $\boldsymbol{B}_{\mathrm{L}}$ and $\boldsymbol{B}_{\mathrm{dem}}$ due to magnetic charges [14] at the surface of the Lorentz sphere and of the sample, respectively.

where $\boldsymbol{r}_i$ is the position of the moment $\boldsymbol{m}_i$ relative to the muon. The sum is over all of the N magnetic ions in the sample which makes it unwieldy to calculate. However, a trick due to Lorentz allows the dipolar field to be calculated in a much more practical manner. A large sphere (known as the Lorentz sphere) is drawn around the muon position $\mathbf{r}_\mu$ as shown in Figure 2.2. This allows the sum to be split into three parts

$$\boldsymbol{B}'_{\mathrm{dip}} = \boldsymbol{B}_{\mathrm{dip}} + \boldsymbol{B}_{\mathrm{L}} + \boldsymbol{B}_{\mathrm{dem}}. \tag{2.7}$$

The first term $\boldsymbol{B}_{\mathrm{dip}}$ has the same form as Equation (2.6), but with the sum restricted to only those moments lying inside the Lorentz sphere. The sum over the moments outside the Lorentz sphere gives rise to the second and third terms which reflect the fact that places where the magnetisation field abruptly finishes (such as the edges of the Lorentz sphere or the surface of a magnetic medium) act as sources of magnetic field $\boldsymbol{H}$ (see Figure 2.2).

- The Lorentz field $\boldsymbol{B}_{\mathrm{L}}$ is the dipole field due to a magnetic medium outside of the Lorentz sphere and is given by $\boldsymbol{B}_{\mathrm{L}} = \mu_0 \boldsymbol{M}_{\mathrm{sat}}/3$, where $\boldsymbol{M}_{\mathrm{sat}}$ is the magnetisation of the material.

- The demagnetising field $\boldsymbol{B}_{\text{dem}}$ arises from the edges of the sample and is given by $\boldsymbol{B}_{\text{dem}} = -\mu_0 \boldsymbol{N} \boldsymbol{M}_{\text{meas}}$ where $\boldsymbol{N}$ is the demagnetising tensor and $\boldsymbol{M}_{\text{meas}}$ is the bulk magnetisation of the sample. The demagnetising tensor $\boldsymbol{N}$ depends on the shape of the sample. Its form is known for some regular shapes, but it is difficult to compute in general, which often makes evaluating the contribution from the demagnetisating field challenging.

The two terms discussed above are both proportional to the magnetisation, so both vanish for the commonly-encountered case of an antiferromagnet in zero field.

2.6 Polarisation functions

2.6.1 Spin precession: Quantum treatment

In a μ^+SR experiment the measured quantity is the time evolution of the average muon-spin polarisation projected along the positron detector direction $\boldsymbol{d}_{\text{p}}$, which can be written [8]

$$P_{d_p}(t) = \text{Tr}\{\rho \boldsymbol{\sigma}(t) \cdot \boldsymbol{d}_{\text{p}}\}, \tag{2.8}$$

where ρ is the density operator of the muon-system ensemble and $\boldsymbol{\sigma}(t)$ is a time-dependent vector of Pauli spin matrices whose time evolution in the Heisenberg representation is given by $\boldsymbol{\sigma}(t) = \exp(iHt/\hbar)\boldsymbol{\sigma}\exp(-iHt/\hbar)$ where H is the (time-independent) Hamiltonian for the muon-system ensemble. Strictly speaking, ρ is a tensor product of the density operators for the muon and the system, i.e. $\rho = \rho_\mu \otimes \rho_{\text{sys}}$. However, here we will consider the muon to be isolated and therefore take the density operator for the system to be the unit operator such that $\rho = \rho_\mu$ (this would not be valid in cases where the muon is quantum entangled with the system, an example of which is given in Section 2.6.4). The density operator is time-independent in the Heisenberg representation. Therefore, the fact that the beam of muons is fully spin polarised (in a direction which we take to be the z axis) implies that

$$\rho = \frac{1}{2}(I + \sigma_z), \tag{2.9}$$

where I is the identity operator. In the the longitudinal geometry, the detector direction $\boldsymbol{d}_\mathrm{p} = \hat{\boldsymbol{z}}$ and hence we measure $P_z(t)$. In the case where the Hamiltonian is diagonalisable, using the fact that $\mathrm{Tr}\{\sigma_z\} = 0$, we then have

$$P_z(t) = \frac{1}{2}\,\mathrm{Tr}\{\sigma_z \sigma_z(t)\} = \frac{1}{2}\sum_{m,n} |\langle m|\,\sigma_z\,|n\rangle|^2 \cos(\omega_{mn} t), \tag{2.10}$$

where $|n\rangle$ are the energy eigenstates of H with energies $E_n = \hbar\omega_n$ and $\omega_{mn} = (E_m - E_n)/\hbar$.

We first consider the case of a single muon in a static magnetic field $\boldsymbol{B}$. The Hamiltonian for the system is $H = -\gamma_\mu \hbar \boldsymbol{S}\cdot\boldsymbol{B}$ where $\boldsymbol{S} = \frac{1}{2}\boldsymbol{\sigma}$ is the spin operator for the muon with gyromagnetic ratio γ_μ. For a magnetic field lying along the direction (θ,ϕ) in spherical polar coordinates, this Hamiltonian can be expressed in the basis $|\uparrow\rangle$ and $|\downarrow\rangle$ corresponding to the muon spin pointing parallel or antiparallel to the z axis as

$$H = -\frac{\gamma_\mu \hbar B}{2}\begin{pmatrix} \cos\theta & \sin\theta e^{-i\phi} \\ \sin\theta e^{i\phi} & -\cos\theta \end{pmatrix}. \tag{2.11}$$

Diagonalising this Hamiltonian yields eigenvectors

$$\begin{aligned} |+\rangle &= \sin(\theta/2)\,|\uparrow\rangle - \cos(\theta/2) e^{i\phi}\,|\downarrow\rangle \\ |-\rangle &= \cos(\theta/2)\,|\uparrow\rangle + \sin(\theta/2) e^{i\phi}\,|\downarrow\rangle\,, \end{aligned} \tag{2.12}$$

with energies $E_\pm = \pm\gamma_\mu \mu \hbar B/2$ respectively. The eigenvectors $|+\rangle$ and $|-\rangle$ represent the cases where the muon's spin is aligned antiparallel and parallel to $\boldsymbol{B}$, respectively. Substituting these results into Equation (2.10) yields

$$P_z(\theta, B, t) = \cos^2\theta + \sin^2\theta\cos(\gamma_\mu B t), \tag{2.13}$$

Thus the spin of the muon precesses about the direction of the field $\boldsymbol{B}$ with a frequency proportional to the magntitude of the field, as shown in Figure 2.3.

The result obtained above holds for the case of a single muon. However, in a μ^+SR experiment, we measure the average polarisation of many muons. In general, this requires averaging over a distribution $p(\boldsymbol{B})$ describing the magnitudes and directions of the fields experience by the muon ensemble. A commonly-encountered case is one in which the muons all experience fields with the same magnitude, but

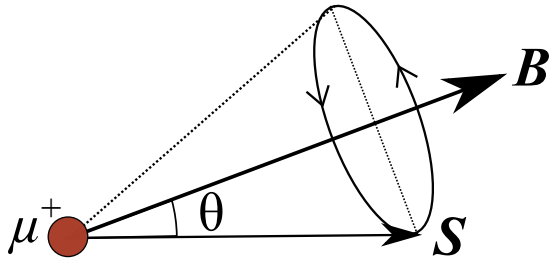

Figure 2.3: A muon spin $\boldsymbol{S}$ at an angle θ to the magnetic field $\boldsymbol{B}$ will precess about the field, describing the end of a cone of semi-angle θ.

that the field randomly points in all directions, with equal probability, with respect to the initial muon spin direction. This describes the state of affairs in a magnetically ordered powder sample, where each muon experiences an internal field of equal magnitude, but with the field at each site pointing in a different direction relative to the initial muon spin direction, owing to the random orientation of the many crystallites within the sample. Averaging over a random distribution of angles θ yields

$$P_z(B,t) = \langle P_z(\theta, B, t)\rangle_\theta = \frac{1}{3} + \frac{2}{3}\cos(\gamma_\mu B t). \tag{2.14}$$

Another simple case is that of a polycrystalline, magnetically ordered sample in which there is more than one magnetically distinct muon stopping site. In this case an appropriate polarisation function is

$$P_z(t) = \sum_i p_i P_z(B_i, t) = \frac{1}{3} + \frac{2}{3}\sum_i p_i \cos(\gamma_\mu B_i t), \tag{2.15}$$

where p_i is the fraction of muons occupying site i, where they experience a local field B_i. However, in all real magnetic materials there will be some variation between the magnetic field at each of the muon sites, which will lead to relaxation of the muon-spin polarisation. The effect of a distribution of fields $p(\boldsymbol{B})$ on the polarisation of the muon spin ensemble is discussed in the next section.

2.6.2 Static field distributions

In the previous section I derived the polarisation function for a muon subject to a magnetic field of magnitude B. However, in general the muon ensemble will be subject to a range of fields that follow a distribution. In this case, relevant

polarisation functions can be obtained by averaging over the probability density function (PDF) $p(\boldsymbol{B})$ for the magnetic field $\boldsymbol{B}$,

$$P_z(t) = \langle P_z(B,\theta,t)\rangle_{B,\theta} = \int \mathrm{d}^3\boldsymbol{B}\, p(\boldsymbol{B}) \left[\cos^2\theta + \sin^2\theta\cos(\gamma_\mu B t)\right]. \tag{2.16}$$

Thus the polarisation of the muon ensemble as a function of time depends on the Fourier cosine-transform of the field distribution.

If each of the components of the magnetic field at the muon site are taken from a Gaussian distribution of width Δ/γ_μ centred around zero field, the resulting PDF is

$$p(\boldsymbol{B}) = \left(\frac{\gamma_\mu^2}{2\pi\Delta^2}\right)^{3/2} e^{\frac{-\gamma_\mu^2 B^2}{2\Delta^2}}. \tag{2.17}$$

The choice of a Gaussian distribution is justified by the central limit theorem, which says that when independent random variables are added, their sum tends towards a normal distribution. A straightforward averaging over this distribution (which includes averaging over a random distribution of angles) gives a polarisation function

$$P_z(t) = \frac{1}{3} + \frac{2}{3}(1-\Delta^2 t^2)e^{-\Delta^2 t^2/2}, \tag{2.18}$$

a result which was first obtained by Kubo and Toyabe [27]. The Kubo-Toyabe (KT) function exhibits a minimum at $t = \sqrt{3}/\Delta$, after which there is a recovery of the initial asymmetry, as shown in Figure 2.4(a). The KT function is frequently used to model relaxation due to the magnetic fields arising from quasistatic nuclear moments.

As demonstrated by the KT function, distributions of fields will generally lead to relaxation of the polarisation. Whereas in a magnetically ordered state where there is a coherent precession of the muon spin ensemble, for a distribution of magnetic fields the spins will each precess at a different frequency, resulting in dephasing. Another interesting case to consider is one in which the sample is magnetically ordered such that there is a large internal field with average magnitude $\langle B\rangle$ at the muon site, but with the field at each muon site having a Gaussian distribution around this value, due to the presence of static disorder. Assuming the width of this distribution is narrow compared to the magnitude of $\langle B\rangle$, the direction of the field at the muon site does not change significantly after adding the Gaussian contribution and the

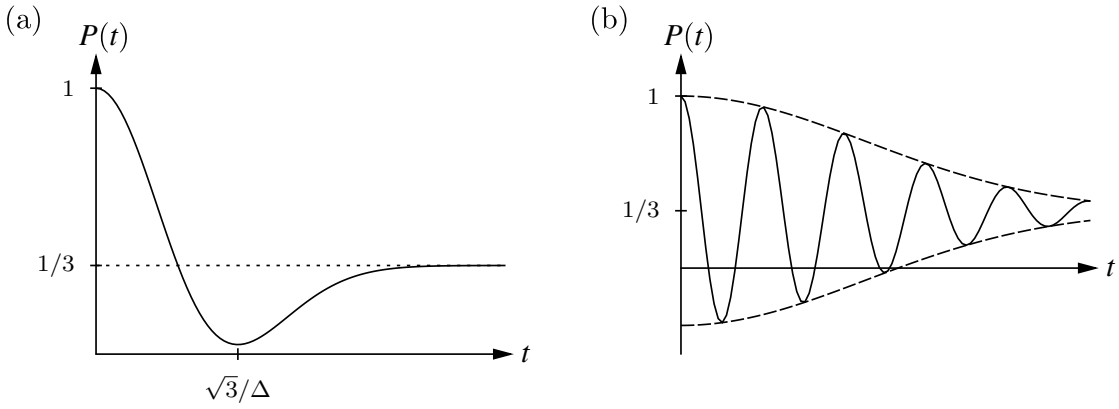

Figure 2.4: Distributions of the magnetic field at the muon site result in relaxation of the polarisation. The Kubo-Toyabe function shown in (a) is due to a Gaussian distribution of fields and exhibits a minimum at $t = \sqrt{3}/\Delta$, after which there is a recovery of the initial asymmetry. In a magnetically ordered system where fields at the muon site have a narrow Gaussian distribution centred on a large average field due to static disorder, the polarisation function consists of oscillations that decay with a Gaussian envelope as shown in (b).

PDF can be approximated by the (one-dimensional) distribution

$$p(B) = \left(\frac{\gamma_\mu^2}{2\pi\Delta^2}\right)^{1/2} e^{\frac{-\gamma_\mu^2(B-\langle B\rangle)^2}{2\Delta^2}}. \tag{2.19}$$

Substituting this into Equation (2.16) gives the polarisation function

$$P_z(t) = \frac{1}{3} + \frac{2}{3}e^{-\Delta^2 t^2/2}\cos(\gamma_\mu\langle B\rangle t). \tag{2.20}$$

Thus the oscillating part of the polarisation decays with a Gaussian envelope due to the distribution of fields experienced by the muons, as shown in Figure 2.4(b). At long times the precessing part of the asymmetry has decayed away and we are left with the so-called 1/3-tail.

The polarisation functions discussed so far have been appropriate for the zero-field geometry. In a transverse-field (TF) μ^+SR experiment the muon spin is rotated about an external magnetic field $\boldsymbol{B}_0$ applied perpendicular to the initial muon spin direction. One measures the transverse component of the muon spin polarisation $P_x(t)$, which, in the limit where the applied field is much larger than the internal

fields in the sample, is given by

$$P_x(t) = \int_{-\infty}^{\infty} \mathrm{d}B\, p(B) \cos(\gamma_\mu B t + \phi), \tag{2.21}$$

where $p(B)$ is the distribution of the component of the local magnetic field parallel to the applied field and ϕ is a phase arising due to detector geometry. The distribution of the local magnetic field $p(B)$ can then be determined from these measurements via a Fourier transform. If, in addition to a large applied field $\boldsymbol{B}_0$, the field at the muon site has a narrow Gaussian component centred on zero, $p(B)$ has the same form as Equation (2.19) and (omitting the phase ϕ) gives the polarisation function

$$P_x(t) = e^{-\Delta^2 t^2/2} \cos(\gamma_\mu B_0 t). \tag{2.22}$$

Thus the polarisation oscillates at a frequency corresponding to the applied field and decays with a Gaussian envelope whose width is related to the distribution of fields at the muon site. TF μ^+SR spectra are most often analysed in the frequency domain, where this distribution of fields manifests as a broadening of the Fourier amplitude centred on the applied field. A magnetically ordered state is indicated by the shifting of the peak in the Fourier amplitude away from the applied field or by the appearance of one or more satellite peaks (see Chapter 6 for examples of this).

2.6.3 Dynamics

The polarisation functions considered so far are for the case of static magnetic field distributions. However, magnetic fields can also vary temporally. These dynamics are often considered by using the strong collision approximation (SCA) [28, 29]. In this approximation the field is assumed to randomly change direction after time t with probability distribution $\rho(t) \propto \exp(-t/\tau)$, with the resulting field completely uncorrelated with the one preceding it. This causes the KT function to be reset at time t_i, with the new initial asymmetry being equal to $P^{(i)}(t - t_i)$. The resulting polarisation function, $P_z(t)$, is the envelope of static polarisation functions [see Figure 2.5(a)] and in the fast fluctuation limit $[1/(\tau\Delta) \geq 5]$ takes an exponential form [17]

$$P_z(t) = \exp(-\lambda t). \tag{2.23}$$

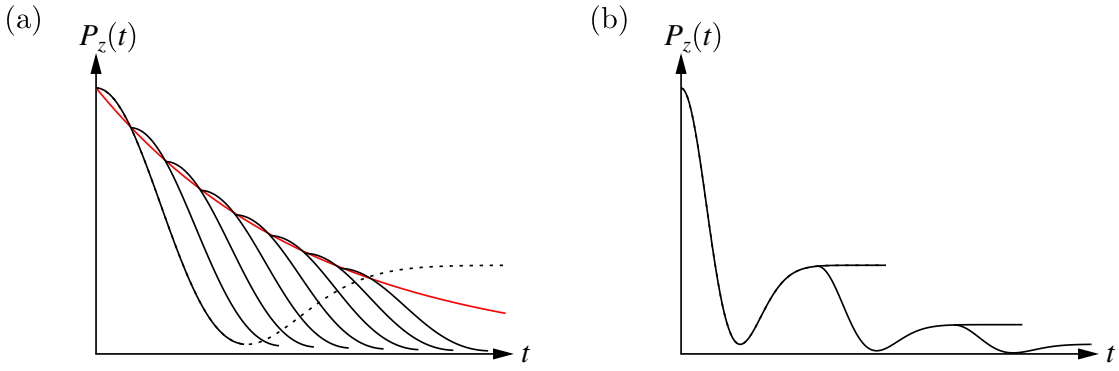

Figure 2.5: Polarisation functions arising from the strong collision model in the (a) fast and (b) slow limits. In the fast fluctuation limit (a), we obtain exponential relaxation as the envelope of static Kubo-Toyabe functions being reset after each "collision" occuring after an average time τ. In the slow limit (b), this resetting of the Kubo-Toyabe function results in the tail of the relaxation decaying away.

where the relaxation rate $\lambda = 2\Delta^2\tau$, with τ being the correlation time for the dynamical processes [28]. The relaxation rate demonstrates the effect of *motional narrowing*; the relaxation rate decreases as the fluctuation rate $\nu = 1/\tau$ increases. This is because faster fluctuations mean that precession barely rotates the spin between each "collision" and hence the loss of polarisation is smaller. Slower dynamics have the effect of squashing the tail of the KT function as seen in Figure 2.5(b). The effect of dynamics in resetting the KT function (which appears Gaussian at early times) often means that Gaussian relaxation is observed rather than the full KT function in the case of quasistatic fields due to the presence of residual dynamics in the system. In both limits it can be seen that the presence of dynamics results in the depolarisation of the 1/3-tail that was non-relaxing in the static case.

A relaxation function commonly used to describe polycrystalline samples in a magnetically ordered state is

$$P_z(t) = \frac{1}{3}e^{-\lambda_z t} + \frac{2}{3}e^{-\lambda_x t}\cos(\gamma_\mu \langle B \rangle t). \tag{2.24}$$

Here λ_z is the relaxation due to dynamical fluctuations perpendicular to z whereas λ_x is due to fluctuations parallel to z. While this function is phenomenological in origin it can be interpreted as a dynamicisation of Equation (2.20) in a similar way to how exponential relaxation results from the dynamicisation of the KT function.

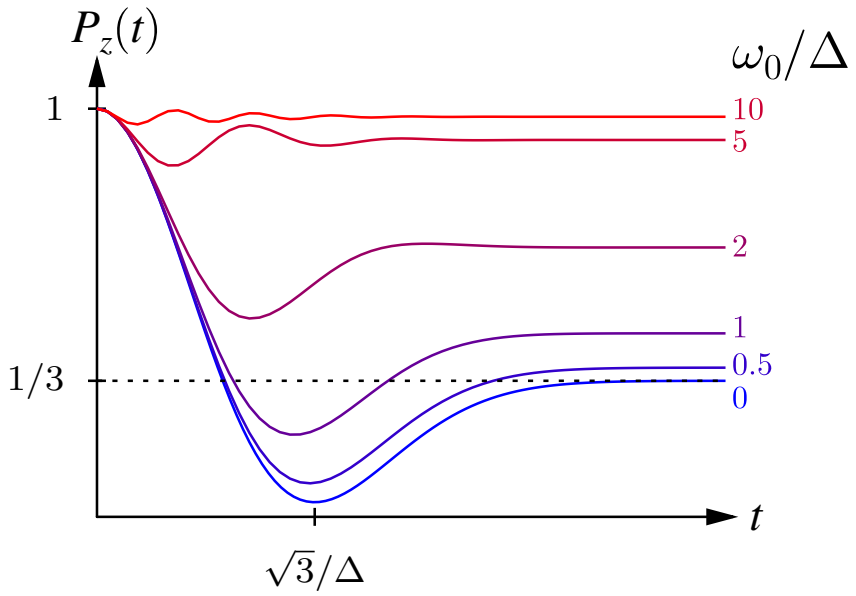

Figure 2.6: The longitudinal-field Kubo-Toyabe function shown for a range of applied fields $\omega_0 = \gamma_\mu B_0$. As $\omega_0 \to 0$ the zero-field Kubo-Toyabe function is recovered.

Thus, in general, the relaxation of the precessing part of the polarisation has contributions from both static disorder and dynamical fluctuations which can interact in a complicated manner.

The longitudinal field (LF) geometry provides a useful method of probing the dynamics of a system. In an LF muon-spin relaxation experiment a field is applied parallel to the direction of the initial muon spin. Being parallel to the muon spin, the applied field does not result in precession but instead 'locks in' the spin direction of the muon, since a large field component lies along the initial muon polarisation direction. This decoupling of the contribution from static magnetic fields allows us to probe the dynamics of the system, with time-varying magnetic fields at the muon site being able to flip muon spins.

When LF is applied to a system where the fields at the muon site follow a Gaussian distribution in the absence of this applied field $\boldsymbol{B}_0 = B_0\hat{\boldsymbol{z}}$, the resulting polarisation function is the LF Kubo-Toyabe function [28]

$$P_z(t) = 1 - \frac{2\Delta^2}{\omega_0^2}\left[1 - \exp\left(-\Delta^2 t^2/2\right)\cos\omega_0 t\right] + \frac{2\Delta^4}{\omega_0^3}\int_0^t \mathrm{d}\tau\, \exp\left(-\Delta^2 t^2/2\right)\sin\omega_0\tau, \tag{2.25}$$

where $\omega_0 = \gamma_\mu B_0$ and the field width Δ includes the applied field. This function is

plotted in Figure 2.6 for a range of values of ω_0/Δ, where it can be seen that for fields $\omega_0 \approx 10\Delta$ the relaxation due to static disorder is quenched and hence any loss of polarisation must be due to dynamics.

2.6.4 Muon-fluorine entangled states

In the polarisation functions discussed so far, the implanted muon has been taken to be a magnetic dipole that couples to the local magnetic field $\boldsymbol{B}$ through the Hamiltonian $H = -\gamma_\mu \hbar \boldsymbol{S} \cdot \boldsymbol{B}$. In this approach, the large number of spin centres surrounding the muon justifies the use of the local magnetic field approximation, in which all the interactions between the muon and these spin centres are contained within the mean field $\boldsymbol{B}$. However, in some experiments, muons are found to be dipole coupled to a small number of nuclei with magnetic moments [30, 31] through the Hamiltonian

$$\mathcal{H} = \sum_{i>j} \frac{\mu_0 \gamma_i \gamma_j}{4\pi |\boldsymbol{r}|^3} [\boldsymbol{S}_i \cdot \boldsymbol{S}_j - 3(\boldsymbol{S}_i \cdot \hat{\boldsymbol{r}})(\boldsymbol{S}_j \cdot \hat{\boldsymbol{r}})], \tag{2.26}$$

where $\boldsymbol{r}$ is the vector linking spins $\boldsymbol{S}_i$ and $\boldsymbol{S}_j$, which have gyromagnetic ratios $\gamma_{i,j}$. This strong interaction is found most often in materials containing fluorine as it is the most electronegative element, causing muons to preferentially localise in its vicinity and occurs as a single isotope (^{19}F) with an $I = 1/2$ nuclear spin. A common occurence in insulating metal fluorides [32] is where the muon sits midway between two F ions forming a strong linear "hydrogen bond" with an F$-$F separation of $d = 0.238$ nm (approximately twice the fluorine ionic radius). The resulting F$-\mu^+-$F complex is often considered as a molecule-in-a-crystal defect similar to the V_k centre found in the alkali halides [33], where the host weakly perturbs the molecular ion.

Extending the formulation of Equation (2.10) to include multiple interacting spins, the longitudinal polarisation can be written as [34]

$$P_z(t) = \frac{1}{N} \left\langle \sum_{m,n} |\langle m|\sigma_q|n\rangle\rangle|^2 \exp(i\omega_{mn} t) \right\rangle_q, \tag{2.27}$$

where $N = \Pi_i (2S_i + 1)$ normalises over possible spin configurations, $|m\rangle$ and $|n\rangle$ are eigenstates of the Hamiltonian $\mathcal{H}$, σ_q is the Pauli spin matrix corresponding to the

direction q and $\langle ... \rangle_q$ represents an appropriately weighted powder average over all directions. This formula allows us to obtain a polarisation function appropriate for a muon occupying an F$-\mu^+-$F complex. For the case where we consider coupling between the muon and the F^- only (i.e. neglecting coupling between the fluorine ions) the Hamiltonian in Equation (2.26) can be diagonalised analytically. Inserting the eigenvalues and eigenstates into Equation (2.27) yields

$$P_z(t) = \frac{1}{6}\left[3 + \cos\left(\sqrt{3}\omega t\right) + \left(1 - \frac{1}{\sqrt{3}}\right)\cos\left(\frac{3-\sqrt{3}}{2}\omega t\right) + \left(1 + \frac{1}{\sqrt{3}}\right)\cos\left(\frac{3+\sqrt{3}}{2}\omega t\right)\right], \quad (2.28)$$

where $\omega = \mu_0\gamma_\mu\gamma_F/4\pi r^3$, γ_F is the ^{19}F nuclear gyromagnetic ratio and r is the μ^+-F separation [32]. Thus from the frequencies observed in this characteristic polarisation function, one can evaluate the the μ^+-F bond length and hence obtain information about the muon stopping site and the distortion the muon causes to the nearby F^- ions. There are many other possible geometries for muon localisation sites close to fluorine ions [35], which will each result in different polarisation functions. However, in each case, the frequencies of the resulting polarisation function depend on the μ^+-F distances. This has proved useful in validating the results of density functional theory calculations of muon stopping sites in fluorine-containing compounds [36, 37].

2.7 Molecular magnets: A μ^+SR case study

Following the introduction of the basic principles and theory behind muon spectroscopy, I now illustrate how the technique is applied in practice. In this section, I report the results of μ^+SR measurements on the Heisenberg antiferromagnetic chain system $Cu(NO_3)_2(pyz)_3$, which form part of a larger study on its magnetic properties, published in Ref. [38]. The application of μ^+SR to this molecular magnet demonstrates how changes in the shape of the spectra as a function of temperature can indicate the onset of magnetic order, which may be difficult to detect using other techniques due to the small magnetic moments in these systems. Here and through-

out this thesis, μ^+SR data have been analysed using the WiMDA program [39].

2.7.1 Introduction

Molecular magnets comprise spin centres (typically transition metal ions) whose principal exchange interactions are mediated via molecular ligands. In some notable cases, large intermolecular spacing and pseudo Jahn-Teller (JT) distortions result in exchange interactions between transtion metal ions being facilitated by bridging ligands such as pyrazine (=pyz=$C_4H_4N_2$). This allows for the construction of polymeric networks whose primary exchange occurs along one, two or three dimensions [40]. In the low-dimensional cases, these chains or planes pack to form crystalline solids, leading to small but non-zero interchain/interplane exchange interactions. Recent progress in the field of molecular magnetism has shown the clear potential for gaining control over the structural building blocks of molecular materials in order to engineer low-dimensional magnetic properties. The manipulation of these building blocks, combined with further ingredients such as counterions [41] and additional ligands [42], enables the synthesis of materials with a wide range of magnetic properties. Furthermore, such systems act as experimental realisations of simple and well-studied model systems, such as the one-dimensional [43] and two-dimensional [44] $S = 1/2$ quantum Heisenberg antiferromagnet.

The $S = 1/2$ one-dimensional quantum Heisenberg antiferromagnet (1DQHAFM) [43] is one of the most important theoretical models in condensed matter physics, with its description revealing a rich range of correlations and an exotic spectrum of excitations [45]. In addition to the principal exchange J along the chains, experimental realisations of this model exhibit some degree of interchain coupling J', resulting in a Hamiltonian of the form

$$H = J \sum_{<ij>} \boldsymbol{S}_i \cdot \boldsymbol{S}_j + J' \sum_{<ij'>} \boldsymbol{S}_i \cdot \boldsymbol{S}_{j'}, \tag{2.29}$$

where the sum $\langle ij \rangle$ is over *unique* pairs of nearest-neighbour spins on the same chain and i and j' label spins on adjacent chains. Models of magnetism in dimensions $d \leq 2$ with continuous symmetry will not show long-range ordering for $T > 0$ due to the divergence of infrared fluctuations [46]. However, the presence of interchain coupling

J' means that real quasi-one-dimensional (Q1D) systems are expected to order at a small but non-zero temperature. The reduced dimensionality of these systems results in quantum fluctuations that significantly reduce the size of the ordered moments [47], making them potentially very small, and difficult to observe with magnetic susceptibility measurements. Finite, but possibly very long, correlation lengths may exist above the ordering temperature, reducing the entropy in the system. Consequently, the entropy change on ordering will be much reduced compared to a more isotropic system and may prevent specific heat measurements from detecting a transition [48]. These factors mean that μ^+SR is likely to be the most sensitive method for determining the ordering temperature T_N by unambiguously detecting the onset of 3D order, as has been done successfully for a number of molecular spin chains [49, 50, 51]. The ratio $T_N/|J|$ is a useful figure of merit for measuring the extent to which Q1D (or Q2D) behaviour has been accomplished as it should be zero in the ideal case and close to unity for an isotropic material. Hence the magnitude of T_N, obtained from μ^+SR, can be used to ascertain how well these materials approximate low-dimensional magnetic systems.

2.7.2 $Cu(NO_3)_2(pyz)_3$

The molecule-based antiferromagnet $Cu(NO_3)_2(pyz)$ (**1**) represents a highly-ideal experimental realisation of the one-dimensional quantum Heisenberg antiferromagnet (1DQHAFM) [52]. Exchange coupling between Cu^{2+} ions is facilitated by pyz ligands [see Figure 2.7(a)] with an exchange constant $J = 10.3(1)$ K determined from magnetic susceptibility [52]. Weak interchain coupling J' results in a state of 3D long range magnetic order at $T_N = 0.107$ K, which was detected using muon-spin relaxation [53]. These measurements give an estimate $|J'/J| = 4.4 \times 10^{-3}$ for the ratio of interchain to intrachain coupling [53].

Like **1**, the Heisenberg antiferromagnetic chain system $Cu(NO_3)_2(pyz)_3$ (**2**) comprises Heisenberg $S = 1/2$ Cu^{2+} ions connected via pyz ligands to form a chain along the a axis [Figure 2.7(b)] [54]. Different from **1**, each metal centre has two further trans-coordinated non-bridging pyz ligands extending perpendicular to the chains, keeping them well separated [Figure 2.7(b)]. This results in regular octahedral co-

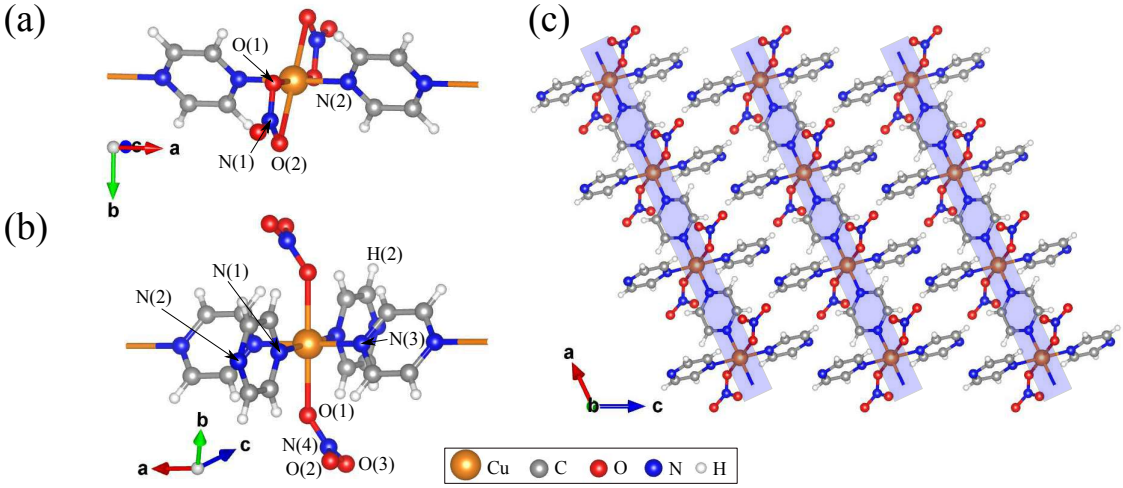

Figure 2.7: Local environments of the Cu^{2+} ions in (a) **1** and (b) **2**. (c) Structure of **2** demonstrating the packing of chains.

ordination of the Cu^{2+} ions in **2**, which has a much higher degree of symmetry than the distorted octahedral environment for Cu^{2+} in **1** [Figure 2.7(a)]. For **2**, our collaborators obtained an intrachain coupling of $J = 13.7(1)$ K (30% larger than in **1**) from measurements of magnetic susceptibility and pulsed-field magnetisation and we argued that different local environments for the Cu^{2+} ions is the main factor responsible for this higher intrachain coupling [38].

Implanted muons are very sensitive to small magnetic fields and were therefore used to probe the low-temperature magnetic behaviour of **2**. Zero-field muon-spin relaxation (ZF μ^+SR) measurements were made on a polycrystalline sample using the low temperature facility (LTF) spectrometer at the Swiss Muon Source. Example μ^+SR spectra are shown in Figure 2.8 (inset). For $T < 0.105$ K we resolve oscillations at a single frequency in the asymmetry, $A(t)$, characteristic of quasistatic long range magnetic order (LRO) at one magnetically distinct muon site. I note that, in an earlier work on **1**, oscillations in the μ^+SR spectra were observed at two distinct frequencies [53]; the additional pyz branches in **2** may block muons from occupying one of the candidate muon sites. The spectra were fitted to the functional form

$$A(t) = A_1 e^{-\lambda_1 t} + A_2 e^{-\lambda_2 t} \cos(2\pi\nu t + \phi) + A_{\mathrm{bg}}, \tag{2.30}$$

where the components with amplitudes A_1 and A_2, due to muons stopping in the sample, have relaxation rates λ_1 and λ_2 respectively and the component with ampli-

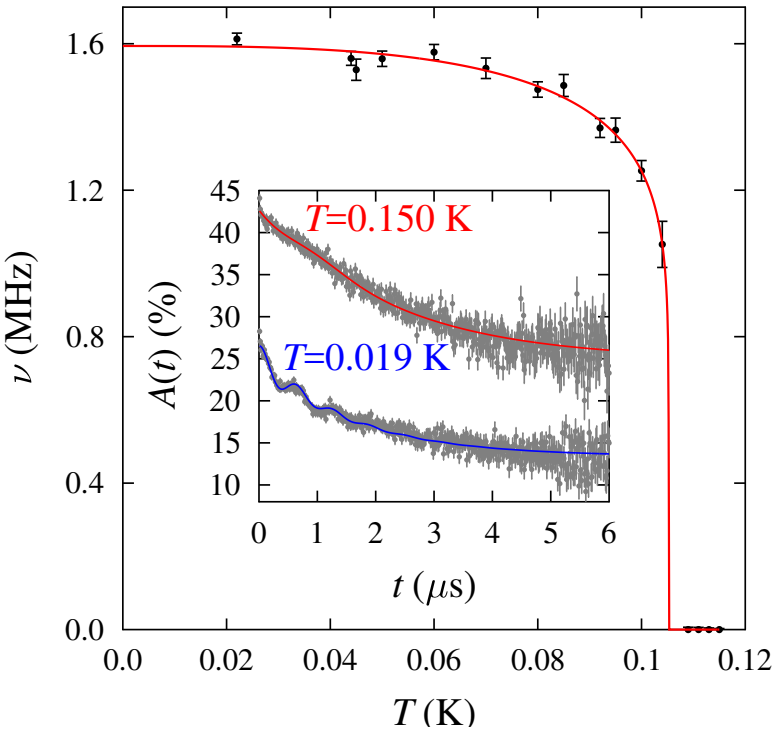

Figure 2.8: Temperature dependence of the muon precession frequency ν for the fits described in the text. Inset: example μ^+SR spectra for **2** measured above and below the magnetic ordering temperature.

tude A_2 oscillates with a frequency ν. A_{bg} is the constant background asymmetry due to muons in the sample holder or those with their spins aligned parallel to the internal field. Above $T = 0.105$ K the spectra change shape and I instead fit the data to the sum of a Gaussian and an exponential relaxation. The change in shape of the spectra reflects the fact that, above the ordering temperature, the electronic moments fluctutate rapidly compared to the muon time scale and hence their contribution is motionally narrowed from the spectra, leaving the muon sensitive to quasistatic nuclear moments, which result in Gaussian relaxation. The oscillation frequency ν (Figure 2.8) is related to the magnitude of the magnetic field at the muon site through $\nu = \gamma_\mu B/2\pi$ where γ_μ is the muon gyromagnetic ratio and serves as an effective order parameter for the system. A fit to the phenomenological function $\nu(T) = \nu(0)[1-(T/T_N)^\alpha]^\beta$ with $\alpha = 3$ (fixed) yields $\nu(0) = 1.59(1)$ MHz, $\beta = 0.12(2)$ and $T_N = 0.105(1)$ K. A precipitous drop in ν on approaching T_N and an accompanying small value for the critical exponent β is also observed in **1**, for which

$\beta = 0.18(5)$ [53], and likely reflects the reduced dimensionality of these systems.

The interchain coupling J' can be estimated from measurements of J and T_N using an empirical formula based on the results of Monte Carlo simulations [55]

$$|J'|/k_B = \frac{T_N}{4c\sqrt{\ln\left(\frac{a|J|}{k_B T_N}\right) + \frac{1}{2}\ln\ln\left(\frac{a|J|}{k_B T_N}\right)}}, \tag{2.31}$$

where $a = 2.6$ and $c = 0.223$. Substituting $|J|/k_B = 13.7$ K and $T_N = 0.105(1)$K we obtain $|J'|/k_B = 0.045$ K and $|J'/J| = 3.3 \times 10^{-3}$. These values are very similar to those obtained for **1** [53]. Furthermore, we can obtain an estimate of the magnetic moment of Cu^{2+} in this system through $m \approx 1.017\left|J'/J\right|^{1/2}$ [47] and obtain $m \approx 0.059\ \mu_B$. The moment is very small, highlighting the effect of quantum fluctuations in suppressing the ordered moment in this low-dimensional system. It is worth noting that the ratio of larger muon precession frequency observed for **1** and the corresponding frequency for **2** is similar to the ratio of the Cu^{2+} magnetic moments in these two systems. This suggests that the muon site in **2** is similar to the higher frequency site in **1**, but with a smaller local field as a result of the slightly smaller Cu^{2+} moment.

In conclusion, the spin-1/2 chain compound $Cu(NO_3)_2(pyz)_3$ exhibits a larger intrachain coupling $J = 13.7$ K and a lower magnetic ordering temperature $T_N = 0.105$ K than $Cu(NO_3)_2(pyz)$, making it a more successful realisation of a 1DQHAFM. The slightly enhanced J is likely due to the details of the local Cu^{2+} environment, while effective chain isolation is maintained by non-bridging pyz branches. μ^+SR played a vital role in the study of this system, as it allowed the detection of a magnetic ordering transition that would be difficult to observe using other techniques, given the very small size of the ordered moment.

Chapter 3

Density functional theory

In this chapter I review the theoretical foundations of density functional theory (DFT) and then focus on the considerations for practical calculations. DFT is a computational quantum mechanical modelling method that is widely used to investigate the electronic structure of atoms, molecules and condensed matter. In this thesis, DFT is used to determine muon stopping sites in crystalline solids and to subsequently analyse their properties.

3.1 Introduction

The foundation for the theory of electronic structure of matter is the non-relativistic, time-independent Schrodinger equation for the many-electron wavefunction Ψ,

$$H\Psi = E\Psi, \tag{3.1}$$

with the Hamiltonian having the form (in Hartree atomic units where $m_\mathrm{e} = \hbar = 4\pi\epsilon_0 = e = 1$)

$$\begin{aligned} H &= -\frac{1}{2}\sum_i \nabla^2_{\boldsymbol{r}_i} + \frac{1}{2}\sum_{i\neq j}\frac{1}{|\boldsymbol{r}_i - \boldsymbol{r}_j|} + \sum_{j,I}\frac{Z_I}{|\boldsymbol{r}_j - \boldsymbol{R}_I|} \\ &= T_\mathrm{e} + V_\mathrm{ee} + V_\mathrm{en}, \end{aligned} \tag{3.2}$$

where $\boldsymbol{r}_i$ are the positions of the electrons and $\boldsymbol{R}_I$ are the positions of the nuclei with charge Z_I. The origin of each of the terms in Equation (3.2) is as follows: T_e is the kinetic energy of the electrons, V_ee is the electron-electron interaction and V_en is

the potential due to the interaction between electrons and nuclei. This Hamiltonian reflects the Born-Oppenheimer (BO) approximation [56], in which, for the purpose of studying the electronic structure, the much heavier nuclei are considered fixed in space. The wavefunction depends on the positions and spin of each of the N electrons in the system, thus

$$\Psi = \Psi(\boldsymbol{r}_1, \boldsymbol{r}_2, ..., \boldsymbol{r}_N, \sigma_1, \sigma_2, ..., \sigma_N). \tag{3.3}$$

Furthermore, because electrons are fermions, Ψ must be antisymmetric under the exchange of any two electrons, i.e. $P_{ij}\Psi = -\Psi$, where P_{ij} exchanges the position and spin coordinates of electrons i and j. In the BO approximation the wavefunctions depend on the nuclear positions $\boldsymbol{R}_I$ parametrically.

For simple systems such as He or H_2, the Schrödinger equation can be solved using variational methods [57, 58]. The main difficulty in solving the Schrödinger equation for the Hamiltonian in Equation (3.2) comes from the electron-electron interaction V_{ee}, which prevents us from writing the solution as a simple (antisymmetrised) product of single-particle wavefunctions. As the system size grows, the number of variational parameters required grows exponentially and we hit an "exponential wall" [59] that renders traditional wavefunction-based methods unfeasible for systems larger than roughly 10 electrons. Electronic structure theory seeks to obtain approximate solutions to the Schrödinger equation in Equation (3.1) that are sufficiently accurate to describe material properties. One of the most popular such theories, and the one that is used in this thesis, is density functional theory (DFT).

In DFT the central quantity is not the wavefunction Ψ, but the electron density $n(\boldsymbol{r})$. The density must satisfy the properties

$$\int \mathrm{d}\boldsymbol{r}\, n(\boldsymbol{r}) = N, \quad n(\boldsymbol{r}) \geq 0. \tag{3.4}$$

Density functional theory formulates the total energy as a functional of the density, that is $E = E[n(\boldsymbol{r})]$. The first example of a density functional theory was the Thomas-Fermi approximation [60, 61], which, while useful for describing some qualitative trends, such as the *total* energies of atoms, was of limited use in questions of chemistry and materials science due to its inability to bind atoms to form molecules. Despite these obvious failings, Thomas-Fermi theory hinted towards DFT

as we know it today, as it provided a (highly-oversimplied) one-to-one link between the electron density and the external potential. While it was clear that Thomas-Fermi theory was a rough approximation to the exact many-body solution to the Schrödinger equation, it was not initially clear how to establish a strict connection between them, since Thomas-Fermi theory is expressed in terms of the electron density $n(\boldsymbol{r})$ whereas the Schrödinger equation is written in terms of the wavefunction Ψ [59]. Hohenberg and Kohn [62] were able to show that a complete, exact description of electronic structure in terms of $n(\boldsymbol{r})$ is possible in principle. The status of the electron density $n(\boldsymbol{r})$ as the basic variable for describing a system is the subject of the two Hohenberg-Kohn (HK) theorems [62], which I now discuss.

3.2 Hohenberg-Kohn theorems

The first Hohenberg-Kohn theorem (HK1) [62] establishes a one-to-one correspondence between the external potential V_{en} which defines the system and the ground-state electronic density. The proof comes in two parts, presented here for a non-degenerate ground state:

1. *Two potentials differing by more than a constant lead to different ground state wavefunctions.*

   Consider the Schrödinger equation for the systems defined by the external potentials V and V' with ground state wavefunctions ψ and ψ' respectively,

   $$(T + V_{\text{ee}} + V)\psi = E\psi \tag{3.5}$$

   $$(T + V_{\text{ee}} + V')\psi' = E'\psi'. \tag{3.6}$$

   Subtracting Equation (3.6) from Equation (3.5) and letting $\psi = \psi'$ yields

   $$(V - V')\psi = \lambda\psi, \tag{3.7}$$

   where $\lambda = E - E'$. Dividing both sides by ψ makes clear the contradiction: $V - V' = \lambda$, which is a constant. Thus different potentials resulting in the same ground state wavefunction ψ can differ only by a constant. Potentials differing by more than a constant therefore lead to different ground state wavefunctions.

2. *Different ground state wavefunctions ψ, ψ' originating from different potentials V, V' lead to different ground state densities n, n'.*

   Again, we use proof by contradiction. Using ψ' as a trial wavefunction for the Hamiltonian defined by V (which is assumed to have a non-degenerate ground state) we have, from the variational principle,

$$E = \langle\psi|\, T + V_{\text{ee}} + V\,|\psi\rangle < \langle\psi'|\, T + V_{\text{ee}} + V\,|\psi'\rangle\,. \tag{3.8}$$

   Letting ψ be a trial wavefunction for the Hamiltonian for V' we also have

$$E' = \langle\psi'|\, T + V_{\text{ee}} + V'\,|\psi'\rangle \leq \langle\psi|\, T + V_{\text{ee}} + V'\,|\psi\rangle\,. \tag{3.9}$$

   where we use $\leq$ because the non-degeneracy of ψ' was not assumed. Adding Equation (3.8) and Equation (3.9) and rearranging we obtain

$$\int \mathrm{d}\boldsymbol{r}\,[V(\boldsymbol{r}) - V'(\boldsymbol{r})][n(\boldsymbol{r}) - n'(\boldsymbol{r})] < 0. \tag{3.10}$$

   Thus if $n(\boldsymbol{r}) = n'(\boldsymbol{r})$ we arrive at the contradiction $0 < 0$.

We have therefore established that for a given external potential, the ground state density is uniquely defined. This requirement of non-degeneracy can be easily lifted [63], but for a degenerate ground state the mapping is no longer one-to-one. In this case, any of the degenerate ground state densities determine the external potential uniquely.

The first HK theorem allows us to write the properties of the ground state of an interacting many-electron system as a unique functional of the electron density. We write

$$\begin{aligned} E[n] &= T[n] + E_{\text{ee}}[n] + E_{\text{en}}[n] \\ &= F_{\text{HK}}[n] + \int \mathrm{d}\boldsymbol{r}\, n(\boldsymbol{r}) V_{\text{en}}(\boldsymbol{r}), \end{aligned} \tag{3.11}$$

where I have defined the Hohenberg-Kohn density functional $F_{\text{HK}}[n] = T[n] + E_{\text{ee}}[n]$. F_{HK} is the holy grail of DFT. It is a universal functional (it does not depend on the external potential) and if it were known we would have solved the Schrödinger equation exactly.

The second Hohenberg-Kohn theorem (HK2) [62] states that $E[n]$ gives the lowest energy if and only if the input density is the true ground state density. We recall from HK1 that a trial density $\tilde{n}$ [satisfying the conditions in Equation (3.4)] defines its own Hamiltonian $\tilde{H}$ and hence its own ground state wavefunction $\tilde{\psi}$. Taking this wavefunction as a trial wavefunction for the Hamiltonian H generated by the true external potential V_{en} we have, from the variational principle,

$$\langle\tilde{\psi}|H|\tilde{\psi}\rangle = E[\tilde{n}] \geq E[n] = \langle\psi|H|\psi\rangle\,. \tag{3.12}$$

Thus for densities $\tilde{n}$ that are not the true ground state density, $E[\tilde{n}]$ provides an upper bound to the true ground state energy.

3.3 Kohn-Sham formulation

The universal functional F_{HK} is not known and the kinetic energy part $T[n]$ is particularly difficult to approximate accurately. In the Kohn-Sham (KS) formulation [64], one approximates the kinetic energy $T[n]$ of N interacting particles with the kinetic energy T_{s} of N non-interacting particles having the same density $n(\boldsymbol{r})$. We also extract from $E_{\text{ee}}[n]$ the direct (Hartree) mean-field contribution. Thus we write

$$\begin{aligned} F_{\text{HK}}[n] &= T[n] + E_{\text{ee}}[n] \\ &= T_{\text{s}} + \frac{1}{2}\int \mathrm{d}\boldsymbol{r}\,\mathrm{d}\boldsymbol{r}'\,\frac{n(\boldsymbol{r})n(\boldsymbol{r}')}{|\boldsymbol{r}-\boldsymbol{r}'|} + E_{\text{xc}} \\ &= T_{\text{s}} + U_{\text{H}}[n] + E_{\text{xc}}, \end{aligned} \tag{3.13}$$

where the exchange-correlation energy

$$E_{\text{xc}} = (T[n] - T_{\text{s}}) + (E_{\text{ee}}[n] - U_{\text{H}}[n])\,, \tag{3.14}$$

expresses our ignorance of the energy in the interacting case. The kinetic energy T_{s} can be cast as a functional of the density $n(\boldsymbol{r})$ by writing it as the sum of the kinetic energies of the single-particle wavefunctions describing a non-interacting system with ground state density $n(\boldsymbol{r})$,

$$T_{\text{s}}[\{[\phi_i[n]\}] = -\frac{1}{2}\sum_{i=1}^{N}\int \mathrm{d}\boldsymbol{r}\,\phi_i^*(\boldsymbol{r})\nabla^2\phi_i(\boldsymbol{r}). \tag{3.15}$$

Using the partitioning in Equation (3.13), the ground-state energy of the interacting system is obtained from a minimisation of $E[n]$ with respect to $n(\boldsymbol{r})$,

$$\begin{aligned} 0 = \frac{\delta E[n]}{\delta n(\boldsymbol{r})} &= \frac{\delta T_{\mathrm{s}}[n]}{\delta n(\boldsymbol{r})} + V_{\mathrm{en}}(\boldsymbol{r}) + \frac{\delta U_{\mathrm{H}}[n]}{\delta n(\boldsymbol{r})} + \frac{\delta E_{\mathrm{xc}}[n]}{\delta n(\boldsymbol{r})} \\ &= \frac{\delta T_{\mathrm{s}}[n]}{\delta n(\boldsymbol{r})} + V_{\mathrm{en}}(\boldsymbol{r}) + v_{\mathrm{H}}(\boldsymbol{r}) + v_{\mathrm{xc}}(\boldsymbol{r}), \end{aligned} \tag{3.16}$$

where the Hartree potential is given by

$$v_{\mathrm{H}}(\boldsymbol{r}) = \int \mathrm{d}\boldsymbol{r}' \, \frac{n(\boldsymbol{r}')}{|\boldsymbol{r} - \boldsymbol{r}'|}. \tag{3.17}$$

This minimisation is equivalent to the minimisation

$$0 = \frac{\delta E_{\mathrm{s}}[n]}{\delta n(\boldsymbol{r})} = \frac{\delta T_{\mathrm{s}}[n]}{\delta n(\boldsymbol{r})} + \frac{\delta V_{\mathrm{s}}[n]}{\delta n(\boldsymbol{r})} = \frac{\delta T_{\mathrm{s}}[n]}{\delta n(\boldsymbol{r})} + v_{\mathrm{s}}(\boldsymbol{r}), \tag{3.18}$$

where $E_s[n]$ represents the total energy of a non-interacting system subject to the potential

$$v_{\mathrm{s}}(\boldsymbol{r}) = V_{\mathrm{en}}(\boldsymbol{r}) + v_{\mathrm{H}}(\boldsymbol{r}) + v_{\mathrm{xc}}(\boldsymbol{r}). \tag{3.19}$$

Hence, one can calculate the ground-state density for the interacting system by solving the Schrödinger equation for the non-interacting KS system experiencing the effective potential $v_{\mathrm{s}}(\boldsymbol{r})$,

$$\left[-\frac{\nabla^2}{2} + v_{\mathrm{s}}(\boldsymbol{r})\right] \phi_i(\boldsymbol{r}) = \epsilon_i \phi_i(\boldsymbol{r}), \quad i = 1, ..., N. \tag{3.20}$$

We can then obtain the corresponding density through

$$n(\boldsymbol{r}) = \sum_{i=1}^{N} |\phi_i(\boldsymbol{r})|^2. \tag{3.21}$$

The total energy of the interacting system can then be obtained as $E = E[n]$.

Since $v_{\mathrm{H}}(\boldsymbol{r})$ and $v_{\mathrm{xc}}(\boldsymbol{r})$ both depend on $n(\boldsymbol{r})$, which is constructed from $\phi_i(\boldsymbol{r})$, Equation (3.20) must be solved iteratively. A calculation will typically start with an initial guess for $n(\boldsymbol{r})$, calculate the corresponding potential $v_{\mathrm{s}}(\boldsymbol{r})$ and then solve Equation (3.20) to obtain the single-particle wavefunctions $\{\phi_i\}$. The wavefunctions $\{\phi_i\}$ can be used to obtain a new estimate for the ground state density using Equation (3.21) and then this process repeats until convergence (either of the total energy, density or some other observable) is achieved.

3.4 Exchange-correlation functionals

While DFT is, in principle, exact, in practice one has to rely on approximations of the exchange and correlation functional since the exact form of $E_{\mathrm{xc}}[n]$ is not known. However, a number of practical, approximate functionals have been developed, which have had great success in describing material properties. In this section I outline two of the most commonly used approximations: the local spin density approximation (LSDA) and the generalised gradient approximation (GGA). Before discussing these approximations it is worth noting that, while in the discussion so far, the energy has been a functional of the density $n(\boldsymbol{r})$, DFT can be extended to spin-polarised systems [65], in which case the energy is a functional of two spin densities, i.e. $E = E[n^{\uparrow}, n^{\downarrow}]$.

3.4.1 Local spin density approximation (LSDA)

In the local spin density approximation (LSDA) we treat the (inhomogenous) density of an electronic system as locally homogeneous and then employ the exchange-correlation energy as it is calculated from the uniform electron gas. We calculate the exchange-correlation energy as

$$\begin{aligned} E_{\mathrm{xc}}[n^{\uparrow}, n^{\downarrow}] &= \int \mathrm{d}\boldsymbol{r}\, n(\boldsymbol{r}) \epsilon_{\mathrm{xc}}^{\mathrm{hom}}[n^{\uparrow}(\boldsymbol{r}), n^{\downarrow}(\boldsymbol{r})] \\ &= \int \mathrm{d}\boldsymbol{r}\, n(\boldsymbol{r}) \left[\epsilon_{\mathrm{x}}^{\mathrm{hom}}[n^{\uparrow}(\boldsymbol{r}), n^{\downarrow}(\boldsymbol{r})] + [\epsilon_{\mathrm{c}}^{\mathrm{hom}}[n^{\uparrow}(\boldsymbol{r}), n^{\downarrow}(\boldsymbol{r})]\right] . \end{aligned} \tag{3.22}$$

The exchange energy $\epsilon_{\mathrm{x}}^{\mathrm{hom}}$ for a homogeneous electron gas can be calculated analytically. The correlation energy $\epsilon_{\mathrm{c}}^{\mathrm{hom}}$ is not known analytically and is instead obtained from a parametrisation of the results of Monte Carlo calculations on the free electron gas [66]. For unpolarised systems the local density approximation (LDA) is found simply by setting $n^{\uparrow}(\boldsymbol{r}) = n^{\downarrow}(\boldsymbol{r}) = n(\boldsymbol{r})/2$.

This is the simplest approximation for the exchange-correlation energy and it favours more homogeneous systems. While chemical trends are normally correct, it tends to over-bind solids and molecules. The L(S)DA fails in atomic systems where large variations in density are important and in describing weak molecular bonds (such as hydrogen bonds).

3.4.2 Generalised gradient approximation (GGA)

The generalised gradient approximation (GGA) contains the next term in a derivative expansion of the electron density:

$$E_{\mathrm{xc}}[n^{\uparrow}, n^{\downarrow}] = \int \mathrm{d}\boldsymbol{r}\, n(\boldsymbol{r}) \epsilon_{\mathrm{xc}}^{\mathrm{GGA}}[n^{\uparrow}(\boldsymbol{r}), n^{\downarrow}(\boldsymbol{r}), \boldsymbol{\nabla} n^{\uparrow}(\boldsymbol{r}), \boldsymbol{\nabla} n^{\downarrow}(\boldsymbol{r})]. \tag{3.23}$$

This is typically more accurate than the LDA. GGAs greatly reduce the bond dissociation energy error, and generally improve transition-state barriers. Unlike the LDA, there is no single universal form for the GGA. In this thesis, I make extensive use of the Perdew-Burke-Ernzerhof (PBE) exchange-correlation functional [67]. This is a parameter-free GGA that achieves an inclusion of gradient corrections without introducing experimentally fitted parameters. This makes the functional accurate for a wide range of systems.

3.5 Practical calculations

In this section I outline some of the techniques used to allow practical calculations using DFT. Particular emphasis is placed on approaches used in the plane wave basis-set electronic structure code CASTEP [68], which has been used to obtain all of the DFT results presented in this thesis.

3.5.1 Brillouin zone sampling

Bloch's theorem states that, for a periodic system, the eigenstates of the one-electron Hamiltonian can be chosen to be a plane wave multiplied by a function with the periodicity of the Bravais lattice, that is (for the band with index n)

$$\psi_{n\boldsymbol{k}}(\boldsymbol{r}) = e^{i\boldsymbol{k}\cdot\boldsymbol{r}} u_{n\boldsymbol{k}}(\boldsymbol{r}), \tag{3.24}$$

where $u_{n\boldsymbol{k}}(\boldsymbol{r})$ has the same periodicity as the Bravais lattice, i.e.

$$u_{n\boldsymbol{k}}(\boldsymbol{r}) = u_{n\boldsymbol{k}}(\boldsymbol{R} + \boldsymbol{r}). \tag{3.25}$$

If we make the substitution $\boldsymbol{k} \rightarrow \boldsymbol{k} + \boldsymbol{G}$, where the reciprocal lattice vector $\boldsymbol{G} = l_1\boldsymbol{b}_1 + l_2\boldsymbol{b}_2 + l_3\boldsymbol{b}_3$ with $\boldsymbol{a}_i \cdot \boldsymbol{b}_j = 2\pi\delta_{ij}$, Equation (3.24) continues to hold. This allows

us to define the eigenstates only within the reciprocal unit cell. All $\boldsymbol{k}+\boldsymbol{G}$ states with $\boldsymbol{G} \neq 0$ are not needed and it is sufficient to know the energy dispersions only within the first Brillouin zone (BZ).

To obtain many quantities in a periodic system it is necessary to integrate over the Brillouin zone. Usually a finite number of k-points are used and the integration becomes a sum

$$\bar{f}_i = \frac{\Omega_{\text{cell}}}{(2\pi)^3} \int_{\text{BZ}} \mathrm{d}\boldsymbol{k}\, f_i(\boldsymbol{k}) = \sum_j w_j f_i(\boldsymbol{k}_j), \tag{3.26}$$

where Ω_{cell} is the unit cell volume and w_j are weighting factors. Special points are chosen for efficient integration of smooth periodic functions. The general method proposed by Monkhorst and Pack [69] is the most widely used because it leads to a uniform set of points determined by a simple formula valid for any crystal [70],

$$\boldsymbol{k}_{n_1,n_2,n_3} \equiv \sum_{i=1}^{3} \frac{2n_i - N_i - 1}{2N_i} \boldsymbol{G}_i, \tag{3.27}$$

where $\boldsymbol{G}_i$ are the primitive vectors of the reciprocal lattice and $n_i = 1, 2, ..., N_i$. This formula leads to a rectangular grid of points of dimensions $N_1 \times N_2 \times N_3$, spaced evenly throughout the Brillouin zone. Integrals over the BZ can be replaced by integrals over only the irreducible BZ (IBZ), comprising only the symmetry-distinct k-points. In this case the weights w_j in Equation (3.26) are taken to be proportional to the number of *distinguishable* k-points related by symmetry to $\boldsymbol{k}_j$. In high-symmetry systems this can greatly reduce the computational cost. In a large supercell, sampling only the Γ point ($\boldsymbol{k}$=0) leads to a substantial speed-up of the calculation since the eigenfunctions become real.

3.5.2 Plane waves

The periodic nature of $u_{n\boldsymbol{k}}(\boldsymbol{r})$ means we can write it as a Fourier series

$$u_{n\boldsymbol{k}}(\boldsymbol{r}) = \sum_{\boldsymbol{G}} c_{n,\boldsymbol{G}} e^{i\boldsymbol{G}\cdot\boldsymbol{r}}. \tag{3.28}$$

Combining (3.24) and (3.28) allows the wavefunction to be written as an infinite sum of plane waves

$$\psi_{n\boldsymbol{k}}(\boldsymbol{r}) = \sum_{\boldsymbol{G}} c_{n,\boldsymbol{k}+\boldsymbol{G}} e^{i(\boldsymbol{k}+\boldsymbol{G})\cdot\boldsymbol{r}}. \tag{3.29}$$

In electronic structure codes using a plane wave basis [71], it is the plane wave coefficients $c_{n,\boldsymbol{k}+\boldsymbol{G}}$ which are to be calculated. In practical calculations this summation has to be truncated at finite $\boldsymbol{G}$. We define a cutoff energy

$$E_{\text{cutoff}} \geq \frac{1}{2}|\boldsymbol{k}+\boldsymbol{G}|^2, \tag{3.30}$$

that determines the largest $\boldsymbol{G}$ included in the summation and controls the accuracy of the basis set. When performing calculations one must be careful to select an appropriate sampling of k-points and plane wave cutoff energy to obtain accurate results. This is usually done by performing calculations with increasingly fine k-point grids and higher cutoff energies until the total energy (or another quantity of interest) no longer changes. This is known as convergence testing.

3.5.3 Pseudopotentials

For electrons in the the vicinity of the nuclei, the steep Coulomb potential results in wavefunctions that vary rapidly in space in this core region (see Figure 3.1), which would require a prohibitively large number of plane waves to be described accurately. Capturing these rapid oscillations is usually unecessary, as we are most often interested in atomic bonding, which only requires an accurate description of the region where the valence electrons overlap. The core region is removed through the use of pseudopotentials [72, 73, 74]. A pseudopotential replaces the strong Coulomb potential of the nucleus and the effects of a tightly bound core electrons by an effective ionic potential acting on the valence electrons. The pseudopotential V_{pseudo} agrees with the all-electron potential for $r > r_{\text{c}}$, but is much weaker than the Coulomb potential closer to the nucleus (as shown in Figure 3.1). The corresponding wavefunction $\tilde{\psi}$ is therefore much smoother in this region compared to the all-electron wavefunction, which significantly reduces the number of plane waves that are needed to describe it accurately.

Ab initio pseudopotentials are generated by the inverse solution of the Kohn-Sham equation for atoms. Accurate and transferrable pseudopotentials are obtained by enforcing the norm-conserving [75] condition that the total charge density inside the core region exactly matches the all-electron one together with the requirement

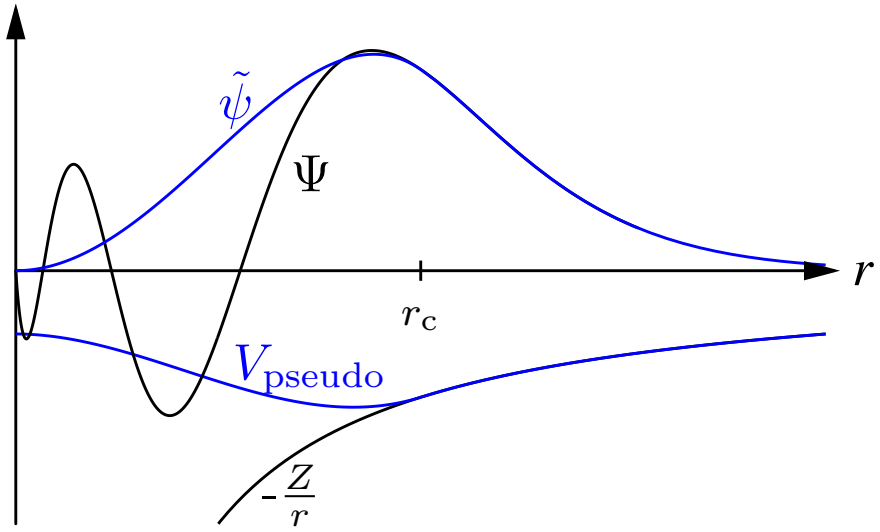

Figure 3.1: Schematic illustration of the pseudopotential concept. For $r > r_c$, both the pseudo-wavefunction $\tilde{\psi}$ and the pseudopotential V_{pseudo} are equal to the all-electron functions.

that, for a given atomic configuration, the pseudopotential provides the exact eigenvalues of the all-electron potential. Norm-conservation comes at the expense of softness (i.e. how smoothly-varying the wavefunctions are) and norm-conserving pseudopotentials often require exceedingly high cutoff energies for the first-row elements and transition metals. Vanderbilt addressed this issue by introducting ultrasoft pseudopotentials [76], which relieve the norm-conserving condition for the smooth wavefunctions, but guarantee the correct evaluation of the core charge by introducing an auxiliary function around each ion core that represents the rapidly varying part of the density. Ultrasoft pseudopotentials are generally more accurate and more efficient than norm-conserving pseudopotentials. All of the calculations in this thesis have been carried out using CASTEP's "on the fly"-generated ultrasoft pseudopotentials.

3.6 Forces

The Schrödinger equation for the nuclei in the BO approximation is

$$H = T_n + V_{ext} + V_{nn}, \tag{3.31}$$

where T_{n} is the nuclear kinetic energy, V_{nn} is the nuclear interaction term and V_{ext} is an external potential. The force (Hellman-Feynman) theorem [77] provides a clever way to evaluate the forces acting on the nuclei as

$$\boldsymbol{F}_I = -\frac{\partial E}{\partial \boldsymbol{R}_I} = -\langle \Phi_{\boldsymbol{R}} | \frac{\partial H}{\partial \boldsymbol{R}_I} | \Phi_{\boldsymbol{R}} \rangle \,, \tag{3.32}$$

where $|\Phi_{\boldsymbol{R}}\rangle$ is the ground state wavefunction for the electrons and the nuclei. This is a general result (not specific to DFT) and relies on the fact that at the exact ground state energy is extremal with respect to all possible variations of the wavefunction. This expression allows one to obtain forces from ground state calculations, which can then be used to analyse vibrational modes in phonon calculations or to perform structural relaxations in geometry optimisation calculations.

3.6.1 Phonons

There are several approaches to calculating phonon frequencies from DFT. One of these is the direct approach, also known as the *frozen phonon* method. This involves creating a structure perturbed by a guessed eigenvector and evaluating the ground-state energy as a function of phonon amplitude, from which the phonon frequency can be obtained by taking the second derivative. This is not a general method and is useful only for small, high-symmetry systems, where the phonon eigenvectors can be deduced from symmetry arguments. Another method is the *linear response* approach [78], in which density functional perturbation theory (DFPT) [79] is used to obtain the linear response of the wavefunction with respect to atomic displacements with wavevector $\boldsymbol{q}$. These derivatives can be used to compute the force constants (the second derivatives of the energy with respective to these displacements) which are used to populate a force constant matrix (FCM). Fourier transforming the FCM obtains the dynamical matrix, which when diagonalised yields the phonon frequencies and corresponding eigenvectors. CASTEP also implements schemes based on numerical differentiation of forces when atoms are moved small distances from their equilibrium positions. This approach, known as the *finite displacement* method, can be used in cases when a DFPT calculation can not. These include when the system is metallic or magnetic, or when the use of ultrasoft pseudopotentials is essential

(these are limitations of CASTEP, rather than of DFPT in general). While the linear response method can be used to study vibrational excitations at any wavevector, the frozen phonon and finite displacement methods can only be used to calculate phonons at $\boldsymbol{q} = 0$. The latter two methods can both be extended to arbitrary $\boldsymbol{q}$ through the use of supercells.

3.6.2 Geometry optimisation

The force [77] and stress theorems [80] enable the computation of forces on the nuclei from the ground state density. This allows DFT to be used to perform optimisations of the ionic positions and unit cell dimensions. Starting from an initial structure, a geometry optimisation calculation proceeds as follows:

1. Calculate the Hellman-Feynman forces on each of the nuclei and use these to optimise the ionic positions according to quasi-Newton methods [81];

2. For the new configuration of ionic positions, optimise the electronic configuration using a conjugate gradients method [82];

3. Compare the total energy and ionic positions with the previous configuration and calculate the forces for the new configuration;

4. If the forces and the changes in total energy and atomic positions are all within the tolerance limits, stop. Otherwise, return to step (1).

Upon exiting this cycle, the energy should be a local minimum with respect to the ionic configuration. For geometry optimisation calculations in this thesis, structures were allowed to relax until forces on the atoms were all $< 5 \times 10^{-2}$ eV Å^{-1} and the total energy and atomic positions converged to 2×10^{-5} eV and 1×10^{-3} Å, respectively (the default values in CASTEP).

There a couple of additional considerations that need to be taken into account when carrying out calculations on systems containing defects or impurities (such as the muon site calculations described in this thesis). Periodic boundary conditions mean that for a point defect in a three-dimensional (3D) system, a 3D periodic array of defects is actually simulated. This necessitates the use of supercells that

are sufficiently large to minimise the effects of spurious interactions between defects. Geometry optimisation calculations can either be carried out with a fixed or variable unit cell. However, for calculations involving defects, fixed cells should be used, with the lattice parameters either optimised for the bulk unit cell or taken from experiment. Otherwise, the lattice constants obtained would be those appropriate for a system containing an ordered array of highly concentrated defects. For calculations in this thesis, lattice constant are fixed at their experimental values unless stated otherwise. For charged defects (such as a postive muon), a neutralising uniform background charge is required to avoid the divergence of the electrostatic energy.

Chapter 4

DFT+μ: Computational prediction of muon stopping sites using density functional theory

In this chapter I review the use of density functional theory to predict muon stopping sites. These types of calculations (coined DFT+μ) have aided the interpretation of muon spectroscopy measurements for a range of systems. There has been much progress in developing these methods over the past few years, including the development of tools to facilitate these calculations. One such tool, introduced here, is the MuFinder program I have developed, which aims to make it easier for non-experts to carry out muon site calculations. I then demonstrate the DFT+μ method using two muon site investigations I have carried out, with each case study comprising pairs of structurally similar systems. I find that the muon stopping sites in the skyrmion-hosting materials GaV_4S_8 and GaV_4Se_8 are the same, but that the chemical substitution of S with Se changes the energetic ordering of the sites and results in a different lowest-energy site in each case. The heavy fermion systems URu_2Si_2 and $CeRu_2Si_2$ are found to have the same stopping site, with these sites lying close to the minima in their electrostatic potentials. The site found for $CeRu_2Si_2$ is different to the site previously proposed on the basis of Knight shift measurements, but I argue that the site obtained here is still consistent with these measurements.

4.1 Introduction

Two of the most fundamental limitations of the muon spectroscopy (μ^+SR) technique are the lack of knowledge of the muon stopping site and the uncertainty surrounding the degree to which the muon distorts its local environment. In some cases it has been possible to determine the muon stopping site experimentally: through the angular dependence of the muon frequency shift in an applied field [83, 84], level-crossing resonances [85, 86] or from the entanglement between the muon's spin and the spins of a small number of surrounding nuclei [32, 35]. The subset of systems for which each of these approaches are applicable is limited and they therefore do not represent general methods for muon site assignment. However, there has recently been significant progress in calculating muon stopping sites using *ab initio* methods.

While there are earlier examples [87, 88, 89] of studies of muons in condensed matter using density functional theory (DFT), the recent concerted research effort in this area began with two independent studies of muon sites in insulating fluorides [36, 37]. Möller *et al.* [36] calculated muon stopping sites for the non-magnetic insulators LiF/NaF (rock salt structure), CaF_2 and BaF_2 (fluorite structure) and the antiferromagnetic insulator CoF_2 (rutile-type structure), considering the cases of both μ^+ and muonium (the bound state of μ^+ and an electron). The calculated structures also allow the distortion induced by the muon to be quantified. It was found that the distortions induced by μ^+ are significant, but short-ranged, whereas the distortions induced by muonium are much smaller. A benefit of carrying out muon site calculations for fluorine-containing compounds is that the quantum entanglement between the muon's spin and the spins of the ^{19}F nuclei leads to a characteristic precession signal whose frequencies depends on the μ^+-F bond length [32] (as discussed in Section 2.6.4). The μ^+-F distances obtained from first-principles calculations can therefore be compared with those corresponding to the measured precession frequencies. In LiF, NaF, CaF_2 and BaF_2 the calculations correctly predict the experimentally known geometries [32] with great accuracy, obtaining bond lengths that are within 3% of the experimental values. In the study by Bernadini *et al.* [37], the authors were able to show that a bent F$-\mu^+-$F state with a bond angle of about 144°, obtained from *ab initio* calculations, results in a polarisation function

that fits the measured spectra for YF_3 better than the function arising from the more commonly assumed linear F$-\mu^+-$F state [32]. A review of these studies and other muon site calculations carried out at around the same time (now referred to as DFT+μ) can be found in Ref. [2]. These techniques have since been applied to a wide range of systems which also includes organic magnets [90], quantum spin ices [91] and coordination polymers [92].

There are two distinct approaches that have been used to determine muon stopping sites. In the Unperturbed Electrostatic Potential (UEP) method, the electrostatic potential of the host crystal is calculated using DFT. For a positively charged defect such as μ^+, the minima of the electrostatic potential are likely stopping sites. (Here and throughout this thesis the electrostatic potential refers to the potential seen by a small positive test charge; in DFT it is common to instead define the electrostatic potential as the potential for an electron). This method has been found to give a good approximation for the muon stopping site in metallic systems [93, 94, 95], where screening of the μ^+ charge prevents strong bonding. However, for ionic systems such as the insulating fluorides discussed above [36, 37], it is found the stable muon sites do not generally coincide with the minima of the electrostatic potential, a finding that reflects the strong muon–lattice interactions in these systems [2]. Moreover, the UEP method cannot be used to determine stopping sites for muonium as, being electrically neutral, there is no reason why it should localise in an electrostatic minimum. An alternative approach based on structural relaxations provides a more robust method of determining muon stopping sites. Here, the muon (modelled by a proton) is placed in randomly-chosen low-symmetry sites in the structure and all of ions are then allowed to relax. This is more computationally expensive than the UEP method, as each initial muon position requires a geomety optimisation calculation. The computational cost is increased further by the fact that this approach often requires the use of supercells in order to minimise the interaction of the muon with its periodic images. A strength of the structural relaxation approach is that it allows the muon-induced distortions of the host crystal to be evaluated, with these potentially having a significant effect on the response of the muon to the system under study. A particularly striking case is that of Pr-based pyrochlores, where the

anisotropic distortion field induced by the muon splits the crystal field levels of Pr^{3+}, resulting in a muon response that is dominated by the distortion it induces, rather than the intrinsic properties of the sample [91].

Knowledge of the muon stopping site makes it possible for μ^+SR measurements to provide estimates for magnetic moment sizes or to compare different candidate magnetic structures. Symmetry analyses of zero-field and transverse-field μ^+SR spectra allowed the magnetic structures in the helical [96] and conical [97] phases of MnSi, respectively, to be determined. These analyses required knowledge of the muon stopping sites, which were determined from the angular dependence of the muon precession frequencies and confirmed using DFT [98]. In α-$RuCl_3$, muon stopping sites calculated using DFT were used to show that the two measured muon precession are consistent with two inequivalent muon sites within a previously-proposed zigzag antiferromagnetic structure [99]. In the spin Jahn-Teller driven antiferromagnet $CoTi_2O_5$, the relative stability of two magnetically distinct muon stopping sites under the shearing of the unit cell that accompanies the magnetic transition was used to explain the fractions of muons occupying each of these sites [100]. In the isostructural compound $FeTi_2O_5$, the dipolar fields calculated at the muon stopping sites (obtained using DFT) were used in conjunction with ZF μ^+SR to restrict the possible moment size and directions of the Fe^{2+} ions [101].

In addition to the growing list of applications there have also been significant advances in developing these methods further. The accurate evaluation of the muon's zero-point energy (ZPE) is often vital for muon site identification; interstitial sites that might be stable for a heavier particle have been shown to be unstable for the muon when this is taken into account [102]. A revision of the Double Adiabatic Approximation (DAA) allows the ZPE of candidate muon sites to be evaluated beyond the harmonic approximation and hence the stability of these sites evaluated [103]. The anharmonicity of the muon's ZPE was further studied using the stochastic self-consistent harmonic approximation, with the delocalised muon wave function obtained from this approach improving estimates of the muon's contact hyperfine field [104]. There has also been progress in developing approaches for muon site prediction based on *ab initio* random structure searching (AIRSS) [105] and machine

learning [106]. The AIRSS approach, based on structural relaxations of a large number of initial structures is computationally expensive. However, it was subsequently found that for organic molecular crystals calculations using the much faster lower-level approximation of Density Functional Tight Binding (DFTB) [107, 108] obtained sites that showed good agreement with those found using DFT and this method could therefore serve as a viable alternative, especially for treating very large organic systems such as polymers or proteins [109]. Tools to facilitate muon site calculations are likely to play a vital role in the widespread adoption of these methods. Examples of such tools include the Muon Spectroscopy Computational Project software suite [109] and the MuFinder program. The Muon Spectroscopy Computational Project software suite is a collection of Python scripts and utilities for determining and analysing the muon stopping sites. MuFinder facilitates the process of calculating muon sites using the structural relaxation method by allowing these calculations to be run through a graphical user interface (GUI), which can also be used to calculated the dipolar field at the obtained sites.

This chapter is structured as follows: in Section 4.2 I introduce the MuFinder program I have developed, in Section 4.3 I report the results of muon site calculations on the skyrmion-hosting systems GaV_4S_8 and GaV_4Se_8, while the result of muon sites calculated for the heavy fermion systems URu_2Si_2 and $CeRu_2Si_2$ are presented in Section 4.4. Finally, I summarise the results of both case studies in Section 4.5, where I also discuss their implications for future muon site calculations.

4.2 MuFinder

I have developed MuFinder, a program for determining and analysing muon stopping sites. The program is written in Python, but is distributed as a standalone executable (that can be run without an existing Python installation) and there are versions of the program for Windows, macOS and linux. MuFinder makes use of several specialised Python libraries. The Atomic Simulation Environment (ASE) [110] is used to manipulate, analyse and visualise atomic structures. The Soprano library [111] is used to handle collections of structures. The dipolar field at the muon

site is calculated using MUESR [112].

The aim of MuFinder is to make it easier for non-experts to carry out muon site calculations similar to those reported in this thesis. It is designed to facilitate the following workflow (illustrated in Figure 4.1) through a simple GUI: first input structures consisting of a muon embedded in the system of interest are generated; these structures are relaxed, with MuFinder providing tools to run these calculations locally or on a remote cluster; the relaxed structures are then clustered into distinct stopping sites and finally the dipolar field at the muon stopping sites can be calculated. The intended workflow is reflected in the design of the MuFinder GUI [Figure 4.2 (left)], where the user works their way along the tabs at the top of the window.

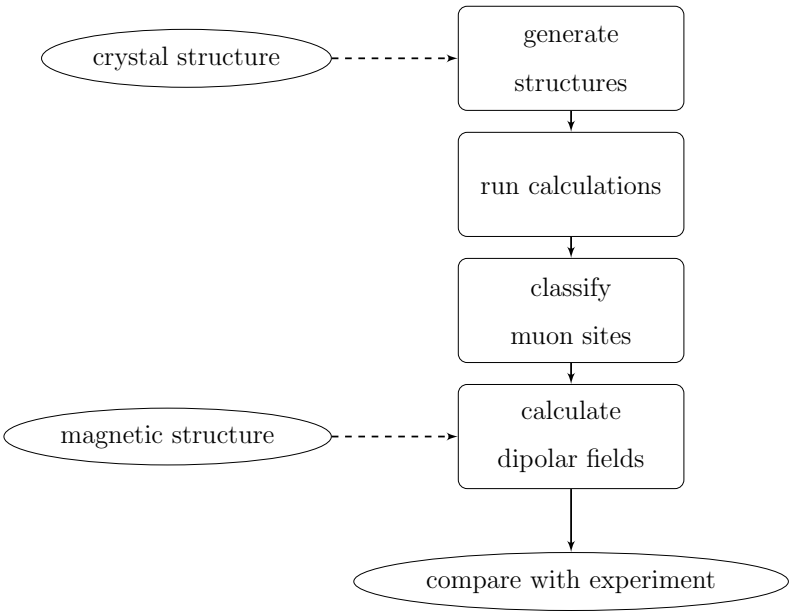

Figure 4.1: The workflow for a muon site calculation using MuFinder.

The muon site calculations for URu_2Si_2 and $CeRu_2Si_2$ (Section 4.4) and those for 1T-TaS_2 in Chapter 7 were carried out using the MuFinder program. All other calculations reported in this thesis predate the development of MuFinder. In the rest of this section I highlight novel features of MuFinder.

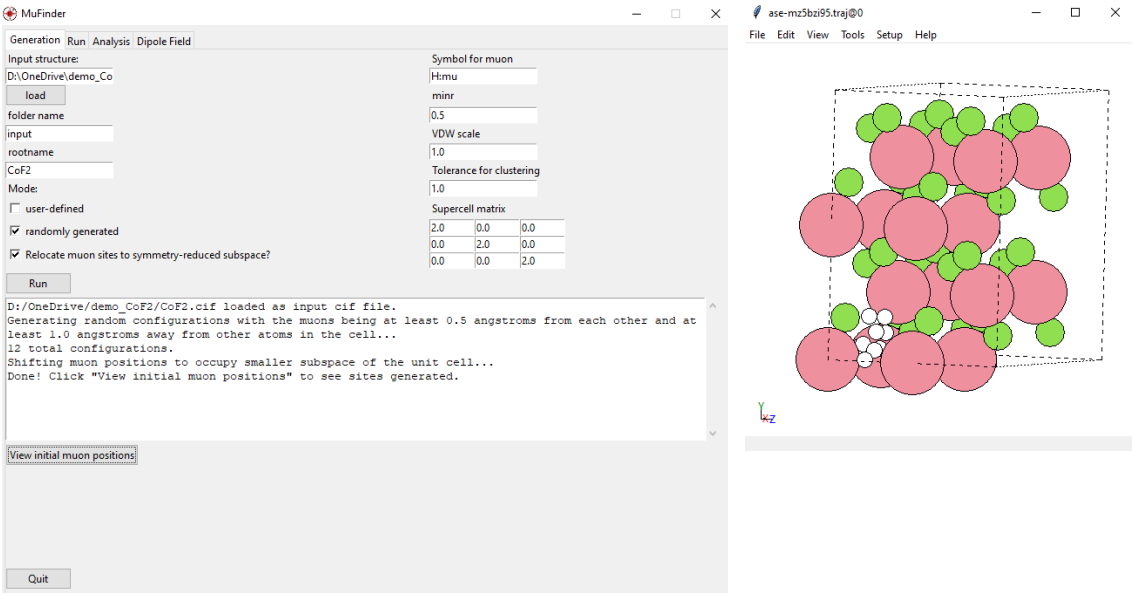

Figure 4.2: A screenshot of the MuFinder program, demonstrating initial muon position generation. *Left:* the main GUI window. *Right:* initial muon positions in a $2 \times 2 \times 2$ supercell of CoF_2 visualised using ase-gui.

4.2.1 Initial position generation

In the structural relaxation approach to calculating muon stopping sites, the possibilty of multiple local minima in the potential energy surface for the muon requires a number of initial muon positions to be sampled in order to successfully identify all of these minima. However, each of these initial muon positions must be relaxed using a geometry optimisation calculation and hence the computational cost increases linearly with the number of initial positions. Thus is it important to be able to generate sets of initial positions that effectively sample the potential energy landscape while minimising the number of initial positions (and hence geometry optimisation calculations).

The algorithm used by MuFinder for generating initial muon positions is based on the one described in Ref. [106] and is as follows:

1. Generate random positions within the conventional unit cell.

2. Accept each position if it and its symmetry equivalent positions are all:

   (i) at least r_{min} away from the other muon positions and

(ii) at least r_{VDW} away from all of the atoms in the cell.

3. Repeat until 30 new positions are rejected.

The number of initial structure generated will depend on r_{min} and r_{VDW} with smaller values leading to a greater number of structures. The choice of the muon–muon distance r_{min} is dictated by the expected shape of the potential energy surface for the muon. For a surface with a large number of minima, finer sampling of the unit cell will be required to successfully locate all of these minima. The muon–atom distance r_{VDW} should be chosen to exclude unphysical situations where the muon sits very close to an atom in the structure. Values of r_{VDW} can be chosen using physical intuition based on typical muon–ion distances, with the MuFinder default value $r_{\mathrm{VDW}} = 1.0$ Å being the typical μ^{+}−O bond length. The main difference between the algorithm used by MuFinder and the one in Ref. [106] is the additional consideration of symmetry equivalent positions in MuFinder (though I note that the authors of Ref. [106] have since adopted a similar approach of generating symmetry equivalent muon positions in their clustering methodology [109]). As the multiplicity of any arbitrary position in the unit cell under the symmetry operations of crystal is the same (provided it is not a high-symmetry point, which is extremely unlikely for a randomly generated position), the positions generated represent an unbiased sampling of the unit cell, which is important if one wishes to make inferences about the basin of attraction of each muon site from the number of initial structures that relax into this site.

Once all of the initial positions have been generated, the positions are clustered according to the algorithm detailed in Section 4.2.2 (albeit with a much larger tolerance than would be used to cluster the output structures). Sites in each cluster are then moved to the symmetry equivalent position closest the member of the cluster that is closest to the origin (while remaining inside the unit cell). The results of the site generation algorithm along with this clustering can be seen for a $2 \times 2 \times 2$ supercell of CoF_2 in Figure 4.2 (right). Clustering the initial positions in this manner results in a roughly uniform sampling of a smaller subspace of the unit cell, that is sufficient to effectively sample all of the symmetry-distinct positions in the unit cell. The rationale behind clustering the initial positions is that it should make it

easier to identify nearly-identical sites in the output, as these sites will lie close in physical space (rather than just sitting at symmetry equivalent positions).

For each muonated structure, MuFinder produces a CASTEP [68] .cell file to use as the starting point for a geometry optimisation calculation. MuFinder provides an interface to run these calculations either locally or on a remote cluster.

4.2.2 Clustering

After carrying at the required geometry optimisation calculations using DFT, each initial position generated following the procedure outlined above will result in a relaxed structure comprising a muon in the host crystal. However, assuming the number of initial positions sampled is sufficiently large, it is unlikely that each of these will correspond to a unique geometry for the muon. One therefore wishes to group the resulting structures based on the local environment of the muon. A possible approach involves inspecting each structure 'by eye' and noting where the muon sits in relation to the nearby atoms in each case. However, this can be tedious and becomes unfeasible in cases where there is of order one hundred or more structures to inspect. It is therefore important to develop algorithms for clustering muon sites.

The clustering algorithm used in MuFinder is based on graph theory. To generate a graph for a set of relaxed muon positions we first construct a distance matrix $\mathbf{D}$, where the component D_{ij} is the minimum distance between muon sites i and j, taking into account symmetry equivalent positions. We then define an adjacency matrix $\mathbf{A}$, where

$$A_{ij} = \begin{cases} 1 & i \neq j, D_{ij} < d_{\max} \\ 0 & \text{otherwise} \end{cases}, \tag{4.1}$$

with $d_{\max}$ being a user specified distance used to determine whether any two muon sites are *connected*. The matrix $\mathbf{A}$ defines a graph where the muon sites form connected nodes; if $A_{ij} = 1$, there is an edge between nodes i and j whereas if $A_{ij} = 0$ there is none. Clusters of distinct sites correspond to the connected components [113] of this graph, determined using the NetworkX library [114]. A connected component of an undirected graph is a subgraph in which any two nodes are connected to each other by paths, and which is connected to no additional nodes in the supergraph (see

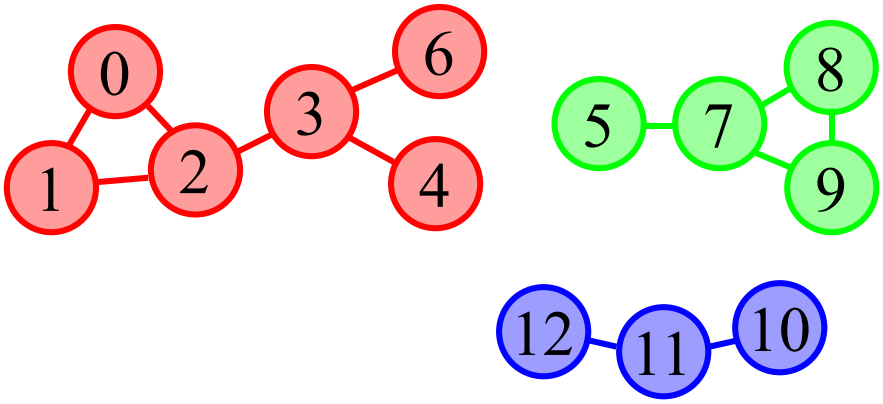

Figure 4.3: A graph comprising a set of nodes (which could each represent a muon stopping site) connected by edges. The graph can be separated into three components (coloured red, green and blue) in which any two nodes within the subgraph are connected to each other by paths, with no paths between nodes belonging to different subgraphs.

Figure 4.3). As seen in Figure 4.3, it is not necessary for each node in a component to be directly connected to each other node in the same component. This can be helpful in cases where the potential energy landscape for the muon has broad minima. Depending on the force tolerance used in the calculations, the shallow gradient of the potential near a minimum could result in a number of final muon positions in the proximity of this minimum, which, because of the broad nature of the minimum, are not all within $d_{\max}$ of each other. However, for two sites at the extremities of this minimum it should be possible to form a path between them using other sites that relaxed towards the same minimum. For sites belonging to distinct minima it should not be possible to form a path between them in this manner and hence the algorithm will correctly identify them as being distinct.

The distance $d_{\max}$ is specified by the user, with no *a priori* optimal value. In practice, the user will vary $d_{\max}$ until they get a satisfactory clustering. If $d_{\max}$ is very large then all of the muon positions will be connected and the algorithm will return only a single cluster. Conversely, a very small $d_{\max}$ will lead to a large number of sparsely populated clusters that will be unwieldy to carry forward for future analysis. Once the muon sites have been divided into distinct clusters, the symmetry operations of the crystal can be used to bring the relaxed muon positions

as close as possible to the position of the lowest energy muon site within the same cluster. This results in a 'clumping' of muon positions in space and can make it easier to visualise the distinct clusters found by the algorithm.

In the clustering algorithm described here, the relaxed structures are clustered by the position of the muon only. It can be easily extended to include the energy E such that each structure is represented by a vector (E, x, y, z), where (x, y, z) is the muon position, and then looking for 'closeness' in this four-dimensional space. However, I often found that energy was not a good discriminator between sites, especially for molecular systems with complex potential energy landscapes (such as the molecular spin ladder $(\mathrm{Hpip})_2\mathrm{CuBr}_4$ discussed in Chapter 6) where sites of the same type can have a wide range of energies that overlap significantly with those of sites that are clearly different. I therefore made the decision to cluster sites on the basis of position alone. MuFinder can also cluster muon sites via k-means clustering as implemented in the Soprano code and described in Ref. [106], which does take the energies of the relaxed structures into account.

4.2.3 Dipolar field at the muon site

MuFinder calculates the dipolar field at the muon site using the MUESR library [112]. MUESR uses the propagation vector formalism [115] and supports calculations for commensurate and incommensurate magnetic structures (limited to single wavevector structures). The dipolar tensor at the muon stopping site can also be evaluated. By default, the fields calculated by MuFinder also include the Lorentz contribution (see Section 2.5), though the user can choose to omit this term should they wish to. The position of the muon site can either be specified manually or obtained automatically from the output of structural relaxations. If the latter method is chosen, MuFinder will also have information about the fully relaxed geometry of the unit cell and it is therefore possible to include the effects of distortions to the magnetic ions induced by the muon when evaluating the field at the muon site.

In most cases the ionic distortions induced by the muon are short-ranged and persist only over several angstroms [36]. A reasonable approximation to the magnetic moments seen by the muon can be therefore obtained by embedding a relaxed

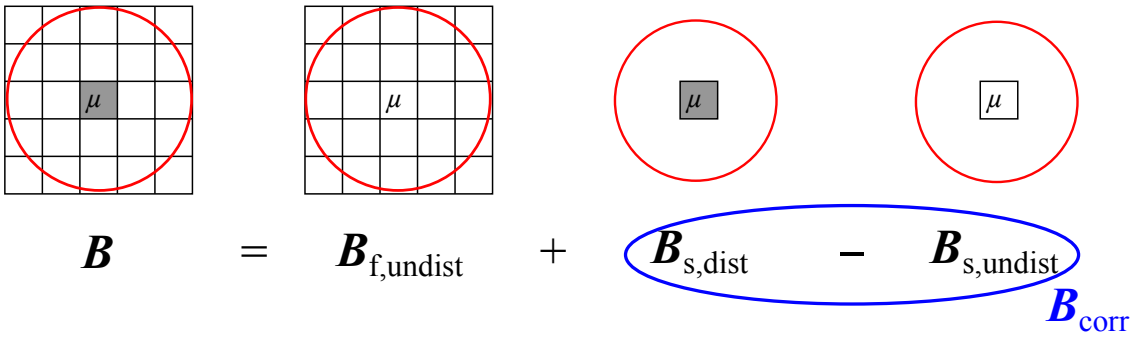

Figure 4.4: Schematic diagram indicating the unit cells included in the dipolar sums and the Lorentz spheres for each of the calculations used to obtain the dipolar field corrected for muon induced distortions. Shaded cells correspond to the relaxed geometry obtained from muon site calculations whereas empty cells are undistorted.

supercell containing the muon within a matrix of undistorted unit cells. Provided the supercell used for structural relaxation was sufficiently large, any distortions outside of the simulation cell should be small enough to neglect. Calculating the dipolar field at the muon site due a moment distribution constructed in this manner is achieved by splitting the dipolar field into three components:

$$\boldsymbol{B} = \boldsymbol{B}_{\mathrm{f,undist}} + \boldsymbol{B}_{\mathrm{s,dist}} - \boldsymbol{B}_{\mathrm{s,undist}}. \tag{4.2}$$

$\boldsymbol{B}_{\mathrm{f,undist}}$ is the full undistorted dipolar field calculated for a large number of unit cells (sufficiently large to ensure convergence) and is what is returned by carrying out a calculation assuming an undistorted structure. $\boldsymbol{B}_{\mathrm{s,dist}}$ and $\boldsymbol{B}_{\mathrm{s,undist}}$ represent the dipolar fields due to only the magnetic moments in the simulation cell for the distorted and undistorted cells respectively. Thus the difference between these two terms gives the correction to the total dipolar field, $\boldsymbol{B}_{\mathrm{corr}} = \boldsymbol{B}_{\mathrm{s,dist}} - \boldsymbol{B}_{\mathrm{s,undist}}$, due to the fact that the ions in the simulation cell are displaced by the presence of the muon. The Lorentz field depends only on the sum of the magnetic moments within the Lorentz sphere and not the positions of these moments. The Lorentz field is therefore identical for the distorted and undistorted cells and thus cancels when taking the difference between these in $\boldsymbol{B}_{\mathrm{corr}}$.

For $\boldsymbol{B}_{\mathrm{s,dist}}$ and $\boldsymbol{B}_{\mathrm{s,undist}}$ only the moments in a single cell are included and thus the system is no longer periodic. The cell is recentred on the muon, such that the distances between the muon and each of the ions correspond to the shortest

distances within the periodic structure (this is also done for an undistorted cell of the same size to allow comparison). A complication arises if the displacements of the ions are such that they cross the boundary of this recentred cell, which results in an anomalously large change in their positions when compared to the undistorted cell. To account for this possibility, each of the ions in the undistorted cell are translated by lattice vectors such that they are as close as possible to the corresponding ion in the distorted cell. The effect of muon-induced distortions on the dipolar tensor can be incorporated in an identical manner. This method is currently only implemented for commensurate magnetic structures, but can be extended to incommensurate structures in principle by considering $\boldsymbol{B}_{\text{corr}}$ corresponding all of the magnetic moment configurations in the unit cell generated by the propagation vector.

To validate my implementation of this approach, I reproduced the muon site calculations of CoF_2 by Möller *et al.* [36], who used a similar approach to account for the distortions of the nearby magnetic Co ions. The dipolar field at the lowest-energy muon site (for diamagnetic μ^+) in each case is reported in Table 4.1, with and without the effect of the distortion of the magnetic ions, along with the field measured from experiment [83]. When considering the undistorted structure, calculations by Möller *et al.* [36] and those carried out using MuFinder both obtain dipolar fields that are around 16% larger than the magnetic field measured experimentally. Including the distortions of the lattice results in a significant decrease to this field, with the field I obtained when incorporating these distortions nearly

Table 4.1: Dipolar field at the μ^+ stopping site calculated by Möller *et al.* [36] and from my calculations using the MuFinder program, along with the local magnetic field measured experimentally [83].

	B (T)	
Experiment [83]	0.228	
	undistorted	distorted
Möller *et al.* [36]	0.265	0.208
MuFinder	0.266	0.209

identical to the one reported by Möller *et al.* [36].

4.3 Example 1: GaV_4S_8 and GaV_4Se_8

Muon stopping site calculations were carried out to support the results of muon spectroscopy experiments on the skyrmion-hosting series $GaV_4S_{8-y}Se_y$ ($y = 0, 2, 4, 8$) carried out by myself and coworkers [116]. These calculations were motivated by an unusual temperature dependence of the local field at the muon site in GaV_4S_8, which was found to *increase* approximately linearly with temperature for temperatures below $T = 10$ K, whereas the magnetisation was found to decrease with increasing temperature [116]. This unusual behaviour was not seen in $GaV_4S_{8-y}Se_y$, whose local fields (as measured by the muon) and magnetisation both decreased as temperature increased. We therefore sought to investigate whether these differences in behaviour result from the nature of the muon stopping site in the two cases or whether it reflects distinct magnetic ground states in the two systems.

4.3.1 Background

Skyrmions are topological spin textures stabilised by the competition between the asymmetric Dzyaloshinskii-Moriya interaction (DMI) [117, 118] and the symmetric exchange interaction. The formation of Néel-type skyrmions in bulk crystals with polar C_{nv} symmetry was first predicted by Bogdanov and Yablonskii [119] and was recently observed in $VOSe_2O_5$ [120], GaV_4S_8 [121, 122] and GaV_4Se_8 [123].

The crystal structure of GaV_4S_8 and GaV_4Se_8 is composed of $(GaX_4)^{5-}$ tetrahedra and $(V_4X_4)^{5+}$ distorted heterocubane units (where X = S, Se), organised in a rock salt-type arrangement (space group $F\bar{4}3m$) [124]. Magnetic moments result from one unpaired electron per metallically-bonded V_4 tetrahedron, causing the V_4 units to carry an effective spin $S = 1/2$ [124, 123]. [Both compounds are insulators due to a large distance (≈ 4 Å) between V_4 clusters.] These materials have a non-centrosymmetric cubic crystal structure with T_d point symmetry at room temperature, but at around 40 K (in both materials) a Jahn-Teller transition changes this to a rhombohedral polar C_{3v} symmetry by stretching the lattice along one of

the four ⟨111⟩ cubic axes [121, 125, 123]. Below the magnetic ordering temperatures ($T_c \approx 13$ K for GaV_4S_8 [126, 121]; and $T_c \approx 17.5$ K for GaV_4Se_8 [127, 123]), applied magnetic fields drive successive transitions between cycloidal (C), skyrmion lattice (SkL), and field-polarised (FP) phases. In contrast to the Bloch-type SkL plane commonly observed to align perpendicular to the applied magnetic field direction, the propagation vectors of the Néel-type SkL are constrained to a plane perpendicular to the rhombohedral lattice distortion [121, 128]. For GaV_4S_8, a uniaxial magnetocrystalline anisotropy is found along this distortion, thought to favour ferromagnetic (FM) alignment below $T_{FM} \approx 5$ K [121, 122].

While GaV_4S_8 and GaV_4Se_8 are very similar in exhibiting a SkL phase, our μ^+SR measurements [116] showed that their magnetic behaviour is quite different. Our LF μ^+SR measurements [116] revealed that the skyrmion phases in GaV_4S_8 and GaV_4Se_8 give rise to emergent dynamics on the muon (microsecond) time scale, reflecting the slowing of magnetic fluctuations perpendicular to the applied field.

4.3.2 Muon stopping sites

Spin-polarised DFT calculation were carried out on GaV_4S_8 with the generalised gradient approximation (GGA) using the PBE functional [67]. I used a plane wave cutoff energy of 950 eV, resulting in total energies that converge to 0.1 eV per cell and a $4 \times 4 \times 2$ Monkhorst-Pack grid [69] for Brillouin zone sampling. I first optimised the ionic positions of the perfect crystal, allowing the ions to move until the energy reaches a convergence threshold; the lattice parameters are held fixed at their experimental values throughout this procedure. Muon stopping sites are determined by placing a muon in one of 68 initial positions and then allowing the structure plus implanted muon to relax.

Structural relaxations of a supercell of GaV_4S_8 using DFT reveal four distinct muon stopping sites (Figure 4.5). Three of these (labeled I – III) involve the muon sitting close to a single S atom, which makes sense on chemical grounds, given the electronegativity of S. A fourth site (site IV) has the muon closer to V atoms and is the highest energy site. In the lowest energy site (site I) the muon sits between two S atoms, in the plane defined by three S atoms within V_4S_4 units

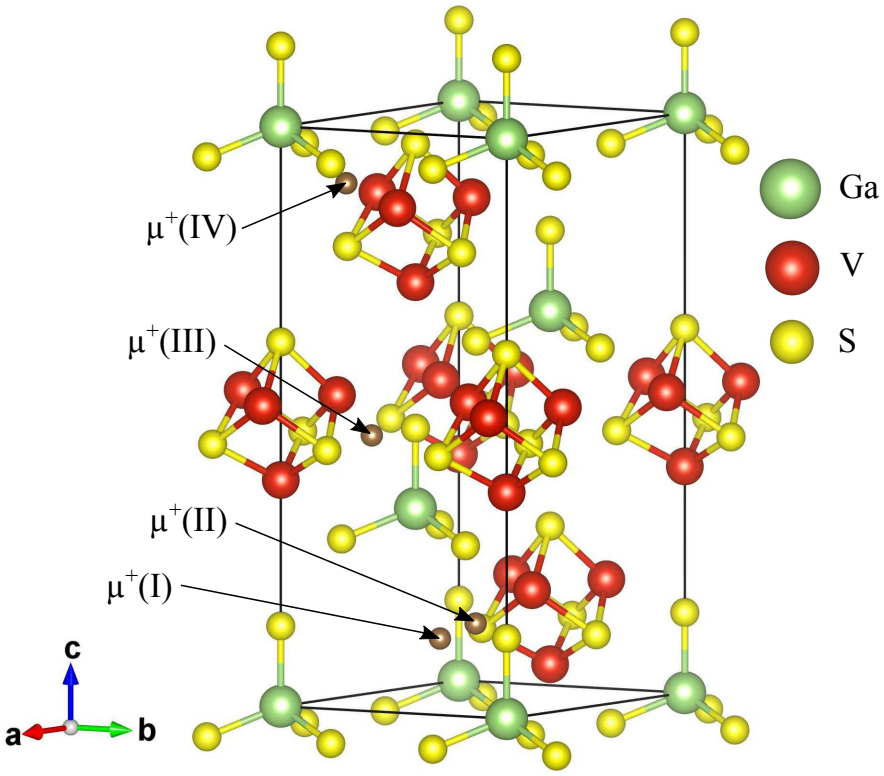

Figure 4.5: Four classes of muon stopping site determined for GaV_4S_8. The sites are numbered in order of increasing energy.

[Figure 4.6(I)]. The two μ^+−S distances are unequal (1.4 Å and 2.0 Å) with greater electron density found between the muon and the nearest S atom. (The S−μ^+−S angle is 160°.) This site is therefore best described in terms of the muon forming a μ^+−S bond (rather than an S−μ^+−S state by analogy to the commonly observed F−μ^+−F complex [32]), though the presence of a second nearby S atom does seem to stabilise this geometry. Two further sites involve the muon sitting close to a single S atom. In site II the muon sits along an edge of one of the V_4S_4 cubane-like units [Figure 4.6(II)]. This site is 0.137 eV higher in energy than site I. The muon sits 1.5 Å from a S atom, which is similar to the shortest μ^+−S distance for site I. In site III [Figure 4.6(III)], the muon again sits 1.4 Å from an S atom, but this time the S atom belongs to a GaS_4 tetrahedron. Despite the similar coordination of the muon by S, this site is 0.288 eV higher in energy than site I. Unlike sites I – III, site IV does not involve the formation of a μ^+−S bond. The muon sits above a face of one of the V_4S_4 cubane-like units, with the nearest S atom just over 2 Å away. The

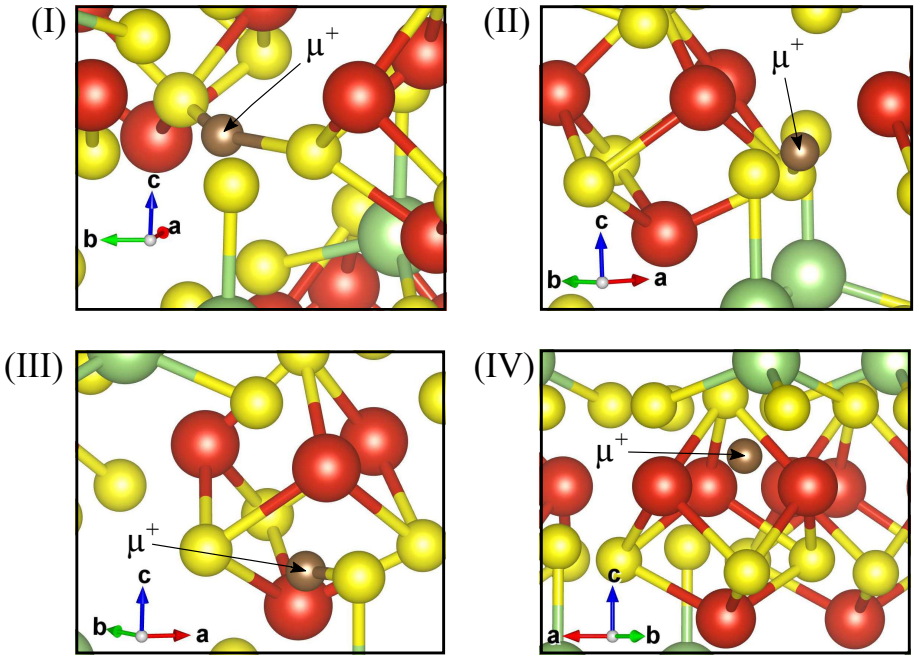

Figure 4.6: Local geometry around the muon for each of the four classes of muon stopping site in GaV_4S_8.

energy of this site is the highest, close to that of site 3: 0.293 eV higher in energy than site I.

I also carried out analogous calculations for GaV_4Se_8. GaV_4Se_8 is not as well-studied as GaV_4Se_8, and the lattice parameters for the rhombohedral phase were not known to us at the time of these calculations (experimental lattice parameters can be found in Ref. [129]). I therefore optimised these using DFT (starting from those of GaV_4S_8). I used a plane wave cutoff energy of 550 eV and $4 \times 4 \times 2$ Monkhorst-Pack grid for Brillouin zone sampling. Forty structures comprising the unit cell plus an implanted muon are relaxed to determine the muon stopping sites.

The results of calculations for GaV_4Se_8 are shown in Figure 4.7. The sites we find are similar to those calculated for GaV_4S_8, with three of the four sites involving the muon sitting close to a Se atom and a site in which the muon sits above a face of a V_4Se_4 unit. However, the ordering of sites is different in this case. In particular, the cube face site (site 1) [Figure 4.8(1)], which was found to be the highest energy stopping site for GaV_4S_8, is the lowest energy site for GaV_4Se_8. The sites in which the muon sits near an Se atom can also be compared to analogous sites for GaV_4S_8. Site 2 [Figure 4.8(2)], which is 0.145 eV higher in energy than the lowest energy

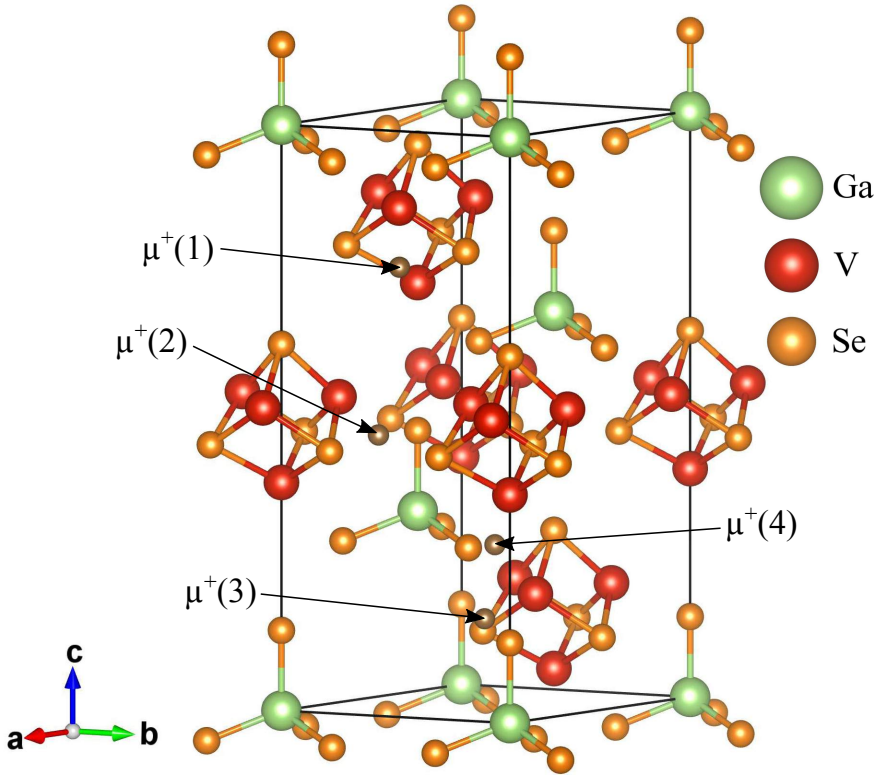

Figure 4.7: The four distinct muon stopping sites determined for GaV_4Se_8. Sites are numbered in order of increasing energy.

site, is similar to site III in GaV_4S_8, with the muon bonded to the Se atom at the top of a $GaSe_4$ tetrahedron. Site 3 [Figure 4.8(3)] is 0.190 eV higher in energy than the lowest energy site and is similar to site II in GaV_4S_8, but with a longer μ^+−Se distance (1.7 Å). Site 4 [Figure 4.8(4), 0.381 eV higher in energy than site 1] is similar to site I in GaV_4S_8.

For both the S and Se members of the series, the muon stopping sites (listed in table 4.2) do not correspond to the minima in the electrostatic potential, which themselves occupy interstitial positions around the GaS_4 tetrahedra. Disagreement between the muon stopping sites and the electrostatic minima has been found in other systems [36] where strong muon–lattice interactions (in our case the interaction between the muon and S/Se) leads to localisation away from the electrostatic minimum.

I conclude that, although the sites for the two systems are similar owing to their similar structures, the energetic ordering of sites in the two cases is rather

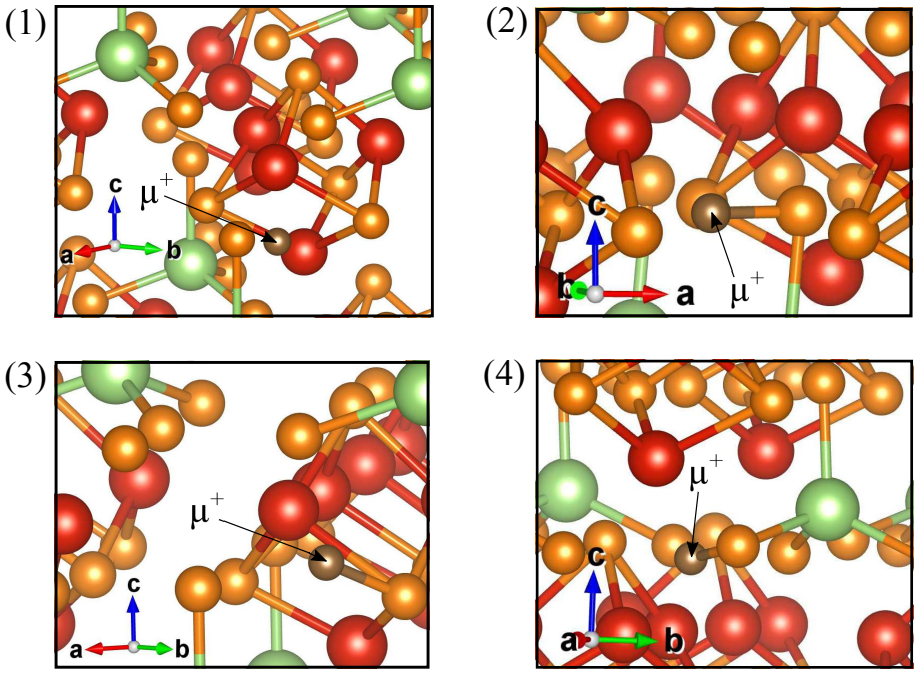

Figure 4.8: The local geometry around the muon for each of the four classes of muon stopping site.

different. In particular, the lowest energy site (which we might expect to contribute the greatest fraction of the asymmetry) is different for the two materials despite their structural resemblance. I note that it seems as though localisation near S seems to be a more important factor than localisation near Se. This could be explained by the higher electronegativity of S compared to Se.

Table 4.2: List of muon stopping sites with their relative energy ΔE and distance d to to closest S or Se atom, respectively.

GaV_4S_8			GaV_4Se_8		
Site	ΔE [eV]	d [Å]	Site	ΔE [eV]	d [Å]
I	0	1.4	4	0.381	1.6
II	0.137	1.5	3	0.190	1.7
III	0.288	1.4	2	0.145	1.7
IV	0.293	2.0	1	0	2.2

4.3.3 Discussion

These calculations were motivated by the unusual increase of the total local magnetic field B_1 with temperature in our ZF μ^+SR measurements on GaV_4S_8 [116]. We therefore suggested that the field at the muon stopping sites behaves in a different way to the bulk magnetisation. A temperature dependent hyperfine contribution at the muon site could be partly responsible for this. This is supported by the observation of a large Knight shift in the TF μ^+SR spectra for GaV_4S_8 [116], indicating a significant hyperfine coupling at the muon site. It is found that for the lowest energy sites in each of the compounds the muon attracts significant electronic density in its vicinity, forming a state that has close to zero charge. I refrain from calling this state muonium due to the fact that the spin density associated with the muon is very small in both cases (whereas muonium refers to the bound state of μ^+ and an $S = 1/2$ electron). These results leave open the possibility of a significant hyperfine contribution to the local magnetic field at the muon site, though the smallness of the spin density prevents us from concluding strongly in favour of its existence. I do not observe any significant structural distortions induced by the muon, which could affect the local magnetic properties (the displacements of the magnetic V ions are within 0.1 Å and 0.2 Å). I attempted to investigate the effect of the implanted muon on the spin configuration, but found that DFT calculations would fall into one of many vastly different magnetic states that are close in energy, which made it difficult to draw robust conclusions about the influence of the muon.

Zhang et al. [130] reported a failure of DFT in correctly predicting a band gap in GaV_4S_8. In our PBE calculations we find that the Fermi energy crosses bands for one of the spin channels, making the material a half-metal. This means that the muon sites detailed above have been calculated on a system with different electronic properties to those observed experimentally. To address this deficiency I have carried out DFT+U calculations, taking the calculated muon stopping sites as our starting point. Using the LDA exchange-correlation functional and applying a Hubbard U of 2.5 eV to the V d orbitals I allowed each of the sites to further relax. I find that the muon sites are unchanged by this procedure. Surprisingly, PBE+U calculations on GaV_4S_8 fail to produce a band gap even for U values up to 4.5 eV.

However, PBE+U calculations with $U = 3.5$ eV were found to result in the same sites determined using the alternative exchange-correlation functionals (PBE and LDA+U). I therefore conclude that the muon stopping sites in this system are not sensitive to the precise form of the exchange-correlation functional used and that calculations at the previous level of complexity (GGA) are sufficient for accurately determining muon stopping sites, despite their failure to properly reproduce all of the material properties.

To help assign each of the calculated muon sites to the sites observed in our μ^+SR measurements I have carried out dipolar field calculations. I take a magnetic moment of 1.73 μ_B per formula unit, corresponding to one unpaired electron V_4 cluster, which has been found to be consistent with values obtained from susceptibility measurements [124]. I take the moment to be localised on the apical V atom and aligned along [111], the magnetic easy axis in this material [121]. Calculating the dipolar field associated with each of the muon stopping sites gives $B = 49, 85, 52, 39$ mT respectively. Because the spin structure is ferromagnetic we need to also consider the effect of the Lorentz and demagnetising fields. These contributions are proportional to the net magnetisation of the sample and are therefore independent of the muon stopping site. These terms act to reduce the magnetic field experienced by the muon at each of the stopping sites. Assuming that the two precession frequencies observed in the ZF data corresond to the two lowest energy sites here I assign B_1 to site II and B_2 to site I. If we assume that $B_L + B_{dem} = -37$ mT, then the total field at each site (neglecting any hyperfine contribution) $B_{1,calc} = 48$ mT and $B_{2,calc} = 12$ mT have magnitudes in the ratio 4:1. These values are slightly higher than those obtained in the experimental data [116], but seem quite plausible. There is also the possibility of significant different hyperfine contributions at the two muon stopping sites, as suggested by the TF μ^+SR data. Furthermore, there is recent evidence that the ground state is more complicated than previously thought, with the suggestion that the system adopts a soliton lattice with periodically arranged FM domain walls as $T \to 0$ [122]. This would result in differences in the field measured at each muon site when compared to those obtained under the assumption of a single FM domain. We must also consider that the approximation of

the moments being located at a single point is a crude one, particularly given that the fields at each of the muon sites is likely to be highly sensitive to the distribution of spin around the nearest V_4S_4 unit. Taking the above considerations into account, these calculations show that the calculated muon sites may be plausibly mapped to those observed experimentally, based on the magnitudes of the fields experienced by the muon at each of these sites.

4.3.4 Summary

Muon stopping sites in the isostructural skyrmion-hosting materials GaV_4S_8 and GaV_4Se_8 are found to be similar, but the energetic ordering of analogous sites is found to be different in the two cases. This may affect which muon sites are occupied in each case. It is argued that these energetic differences are due to the different electronegativities of S and Se, which affects how favourable it is for the muon to localise near these atoms.

It is also shown that, despite failing to reproduce the insulating ground state of GaV_4S_8, the PBE functional is sufficient to accurately determine the muon stopping site. The muon sites obtained are the same as those found using the LDA+U functional with $U = 2.5$ eV, which successfully captures the insulating ground state. This illustrates that it may not be necessary to successfully reproduce all material properties in order to get an accurate estimate of the muon stopping site. Finally, I show that by evaluating the dipolar fields at the muon sites for a candidate magnetic structure, the fields experience by the muons at these sites can be compared with those corresponding to the observed muon precession frequencies.

4.4 Example 2: URu_2Si_2 and $CeRu_2Si_2$

The heavy fermion system URu_2Si_2 has been the subject of several μ^+SR studies [131, 132, 133, 134], with the most recent of these measurements carried out by my colleague Murray Wilson. However, the muon stopping site in URu_2Si_2 was not previously known, which has prevented quantitative estimates of the sizes of magnetic moments being made from these measurements. With calculation of the

muon stopping site using DFT, reported in this section, this is no longer the case.

The isostructural compound $CeRu_2Si_2$ has also been the subject of many μ^+SR studies [135, 84, 136, 137]. The most relevant of these is the experimental determination of the μ^+ site in transverse-field measurements by measuring the angular and temperature dependence of μ^+ Knight shifts [84]. This provides experimental values for the components of the dipolar tensor which can be compared with those calculated for a candidate muon site. The muon stopping site in $CeRu_2Si_2$ was calculated in order to determine whether DFT obtains a stopping site that is consistent with these measurements. Comparison can also be made between the sites calculated for URu_2Si_2 and $CeRu_2Si_2$, which might be expected to be similar on account of their structural similarity.

4.4.1 Background

The heavy fermion metal URu_2Si_2 has been the subject of considerable research interest over the past three decades [138]. The low-temperature specific heat of URu_2Si_2 exhibits two phases transitions [139]. The transition at $T = 1.1$ K is known to result in a superconducting state at lower T. On the other hand, the nature of the second order phase transition at 17.5 K [140, 141] to an enigmatic "hidden order" phase is less well understood, with the name given to this phase reflecting the fact that its order parameter is unknown. A first-order transition into a large moment antiferromagnetic state (LMAF) with a moment of 0.4 μ_B [142] at a critical pressure of 0.5–0.8 GPa was observed used neutron scattering [143] and μ^+SR [131]. Furthermore, μ^+SR [132, 133] and NMR measurements [144] show that the weak antiferromagnetic moment seen at ambient pressure can be explained by a small volume fraction of the high-pressure LMAF state coexistencing with the hidden order phase.

Another method to perturb the hidden order state of URu_2Si_2 is chemical doping. It has been found that doping of the silicon site has only a weak effect on the electronic state which may be explained by a chemical pressure effect [145, 146], whereas doping of the uranium [147, 148] and ruthenium [149, 150, 151, 152] sites cause much more dramatic changes in behaviour. A recent μ^+SR study [134] found

that when doping the ruthenium site with Fe or Os, the antiferromagnetic state exists down to low doping levels for both dopants and that the internal field seen by the muon increases with doping. Knowledge of the muon stopping site could be used to determine how the magnetic moment changes between these samples and to explore the possibility of whether the muon stopping site is likely to change with doping.

The isostructural compound $CeRu_2Si_2$ appears to be close to a local-moment-magnetism transition, as can be seen from its extreme sensitivity to internal pressure (applied by chemical substitution of Si for Ge, for example). It was originally classified as one of the few heavy-fermion systems exhibiting a Fermi-liquid paramagnetic ground state, but this picture was changed by μ^+SR measurements on single crystals [135].

μ^+SR measurements were first dedicated to determining the μ^+SR stopping site by analysing the angular and temperature dependence of the muon Knight shift [136, 84]. These measurements are discussed in more detail in Section 4.4.3, where the stopping site obtained from density functional theory calculations is compared to the one determined experimentally. Zero-field studies at very low temperature were undertaken to probe for the occurrence of static magnetism [136]. These measurements suggest a field distribution with zero average values and a spread of 0.02 mT at the muon site which was proposed to be due to static Ce moments of order $\mu_s \approx 10^{-3}\ \mu_B$ ordering in a complicated (possibly incommensurate) structure. The dynamics of the f electrons at high temperatures was investigated using transverse-field μ^+SR measurements [137]. These obtain an estimate of $\approx 0.6\ \mu_B$ for the fluctuation Ce moments, much higher than the static moments measured below 2 K using ZF μ^+SR. Longitudinal field measurements at low temperature exhibit a small relaxation rate that suggests the presence of small f-spin fluctuations below 2 K [135]. Hence the μ^+SR data seem to indicate the coexistence of static ultrasmall-moment magnetism and dynamical f-spin fluctations involving much larger moments at low temperatures.

4.4.2 Muon stopping sites

I have carried out density functional theory (DFT) calculations in order to determine the muon stopping sites in both of these compounds. For URu_2Si_2, structural relaxations were carried out on a supercell comprising $2 \times 2 \times 1$ body-centred tetragonal cells of URu_2Si_2. I worked within local spin density approximation (LSDA), which has previously been shown [153] to produce results consistent with the known experimental properties of URu_2Si_2. I use a plane-wave cutoff energy of 2700 eV and a $3 \times 3 \times 3$ Monkhorst-Pack grid [69] for Brillouin zone integration, resulting in total energies that converge to 0.01 eV/atom.

Candidate structures comprising a muon and the URu_2Si_2 supercell were generated by requiring the muon to be at least 0.5 Å away from each of the muons in the previously generated structures (including their symmetry equivalent positions) and at least 1.0 Å away from any of the atoms in the cell. This resulted in 19 structures which were subsequently allowed to relax.

I identified two distinct muon stopping sites in this material (see Figure 4.9). In site 1 (Figure 4.9, black spheres) the muon sits 0.68 Å above the centre of the bottom edges of the unit cell [fractional coordinates (0.009,0.499,0.071)]. I note that this position is slightly displaced from the minimum in the electrostatic potential which lies at the centre of the line joining nearest neighbour uranium atoms in the basal plane. The local geometry of the muon for both sites is shown in Figure 4.10. The distortions to nearby atoms are all small for site 1, with the nearby U atoms being displaced by around 0.1 Å away from the muon. In site 2 [Figure 4.9, white spheres, fractional coordinates (0.189,0.193,0.164)] the muon is coordinated by a U and a Si atom [see Figure 4.10(b)]. The displacement of the nearest U atom is significantly larger for site 2 (≈ 0.2 Å) than for site 1. Site 2 is around 0.45 eV higher in energy than site 1.

The local magnetic field at the site is the sum of the dipolar, hyperfine, Lorentz and demagnetising fields. In the large-moment antiferromagnetic state (LMAF) with a moment of 0.4 μ_B [142], the Lorentz and demagnetising fields are zero. The hyperfine field at the muon site cannot be neglected *a priori*. In fact, Knight shift measurements on heavy fermion systems [84] suggest that this contribution is com-

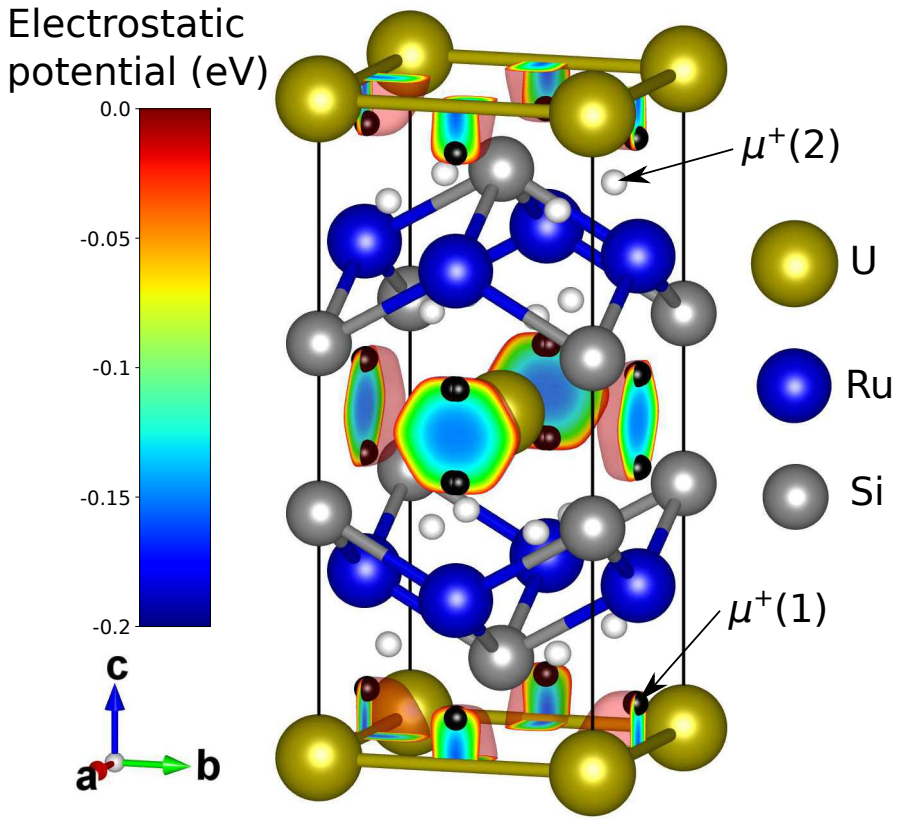

Figure 4.9: The two crystallographically distinct muon stopping sites in URu_2Si_2 and their symmetry equivalent positions. The lower energy site (site 1) is represented by black spheres and the higher energy site (site 2) by white spheres. I also show the electrostatic potential of the host crystal, visualised using VESTA [154].

parable to the dipolar contribution in these systems and I will return to the hyperfine field shortly. I have calculated the dipolar field at both candidate stopping sites using MUESR [112] and present the results in Table 4.3. The local distortions induced by the muon are seen the reduce the dipolar field at both candidate stopping sites, with the reduction being small for site 1 and much larger for site 2 on account of the relative sizes of the displacements of the nearby magnetic U ions.

The dipolar field at site 1 is along the c axis, consistent with experiment [134]. On the other hand, the field at site 2 has a significant component in the ab plane. I therefore propose that site 1 is the muon stopping site that is realised in this material. Inclusion of the hyperfine field would not be expected to change the direction of the field at the muon site, as the transferred hyperfine field due to the RKKY interaction is either parallel or antiparallel to the direction of the localised moments [8], which

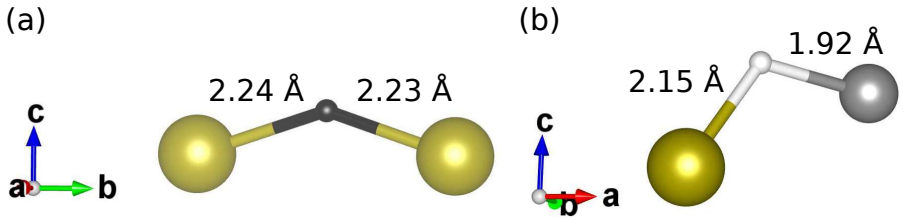

Figure 4.10: The local geometry of the muon site for (a) site 1 and (b) site 2.

Table 4.3: Relative energies and dipolar fields at each of the candidate muon stopping sites. B_{undist} denotes the dipolar field at the position of the muon in the unrelaxed structure. B_{dist} takes into account the changes to the dipolar field resulting from the muon-induced displacements of the nearby magnetic ions.

Site no.	Energy (eV)	B_{undist} (mT)	B_{dist} (mT)
1	0	88.1	83.5
2	0.45	66.6	42.1

also lie along the c axis.

For calculations on $CeRu_2Si_2$, I again used a $2 \times 2 \times 1$ supercell and generated initial positions by requiring the muon to be at least 0.35 Å away from each of the muons in the previously generated structures (including their symmetry equivalent positions) and at least 1.0 Å away from any of the atoms in the cell (which resulted in 32 initial positions). I used a plane-wave cutoff energy of 490 eV, which results in atomic energies that converge at the level of around 0.1 eV/atom and used a $2 \times 2 \times 2$ Monkhorst-Pack grid [69] for Brillouin zone sampling. The PBE functional [67] was used, with the system treated as non-spin-polarised. The lower cutoff energy and k-point sampling compared to those used for URu_2Si_2 reflects the fact that the stopping sites in URu_2Si_2 were observed not to change significantly when comparing the results of structural relaxations using the parameters reported earlier and those using values similar to those listed here and hence this lower level of accuracy is also likely to be sufficient to accurately determine the muon stopping sites in the isostructural $CeRu_2Si_2$ (at a reduced computational cost).

Structural relaxations result in a muon stopping site that is very similar to site 1 in URu_2Si_2 [the lowest energy site has fractional coordinates (0.497, 0.005, 0.072)].

One initial position relaxed to a site similar to site 2 in URu_2Si_2, with this site having an energy 0.36 eV higher in energy than site 1. However, given the lower energy of site 1 and the fact that nearly all of the initial positions relaxed into this structure (implying it has a larger basin of attraction) I conclude that there is a single crystallographically distinct stopping site in $CeRu_2Si_2$. This site is shown in Figure 4.11 where I also show the electrostatic potential of the unperturbed crystal. The minima of the electrostatic potential has a very similar shape to that of URu_2Si_2 (Figure 4.9) which likely explains why the muon sites obtained are the same for both compounds.

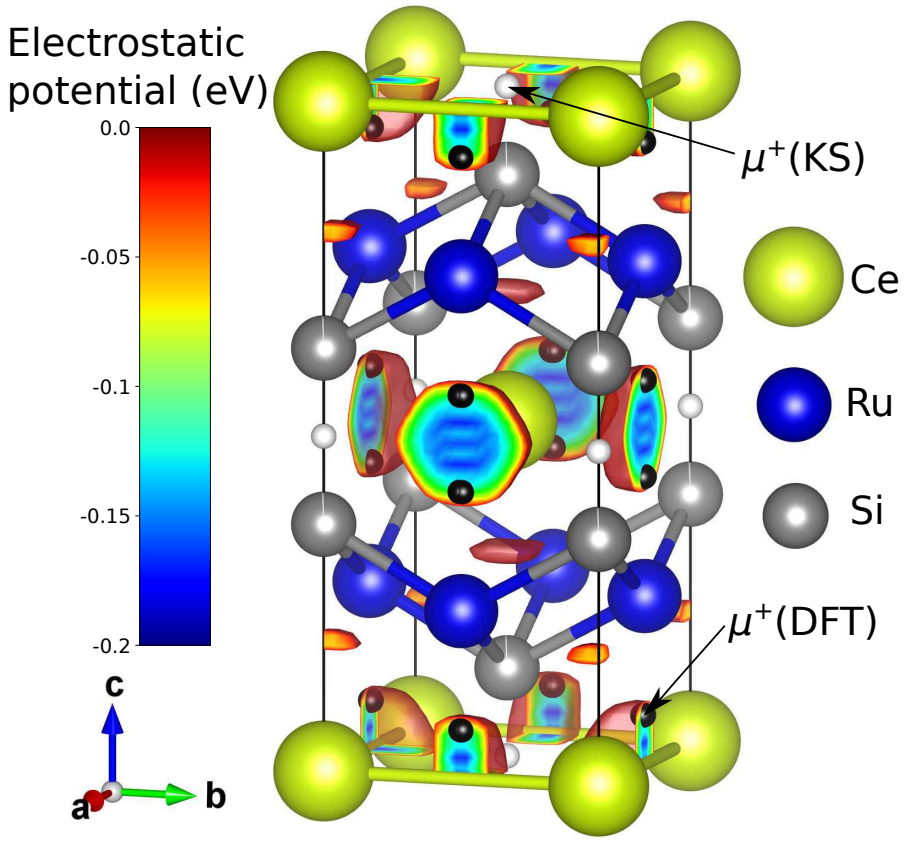

Figure 4.11: Candidate muon stopping sites in $CeRu_2Si_2$ and their symmetry equivalent positions. The site obtained from DFT is represented by black spheres and is distinct from the site previously proposed on the basis of Knight shift measurements [84] (white spheres). I also show the electrostatic potential of the host crystal, visualised using VESTA [154].

4.4.3 Discussion

The μ^+ stopping site in $Ce_2Ru_2Si_2$ has previously been determined experimentally from measurements of the μ^+ Knight shift [84]. The Knight shift [155] measures the shift in the nuclear magnetic resonance frequency of a paramagnetic substance away from the applied field. Applied to muons, the Knight shift measures the shift between the the local magnetic field at the muon site $\boldsymbol{B}_\mu$ and the external field $\boldsymbol{B}_{\text{ext}}$ and is defined as

$$K_{\text{exp}} = \frac{\boldsymbol{B}_{\text{ext}} \cdot (\boldsymbol{B}_\mu - \boldsymbol{B}_{\text{ext}})}{B_{\text{ext}}^2}. \tag{4.3}$$

As the Lorentz and demagnetising fields at the muon site do not provide microscopic information, it is more common to refer to the so-called muon Knight shift,

$$K_\mu = \frac{\boldsymbol{B}_{\text{ext}} \cdot (\boldsymbol{B}_\mu - \boldsymbol{B}_{\text{L}} - \boldsymbol{B}_{\text{dem}} - \boldsymbol{B}_{\text{ext}})}{B_{\text{ext}}^2}, \tag{4.4}$$

in which the contributions from the Lorentz field $\boldsymbol{B}_{\text{L}}$ and the demagnetising field $\boldsymbol{B}_{\text{dem}}$ have been subtracted. For rare-earth or actinide compounds, the muon Knight shift can be written as $K_\mu = K_0 + K_f$, where K_0 and K_f correspond to the contributions of of the internal fields arising from the polarisation of conduction electrons and localised f-moments induced by the external field $\boldsymbol{B}_{\text{ext}}$ respectively. K_0 is proportional to the Pauli susceptibility which is usually temperature independent and isotropic. Thus the angular and temperature dependence and angular dependence of K_μ will arise solely from K_f.

K_f is usually much larger than K_0 and comprises two contributions from the localised f-moments: (i) the dipolar interaction between the f-moments and μ^+ and (ii) an increased hyperfine contact field due the additional spin polarisation of conduction electrons at the μ^+ site through the Ruderman-Kittel-Kasuya-Yosida interaction. Both contributions are proportional to the component of susceptibility associated with the f-moments $\boldsymbol{\chi}_f$ and the muon Knight shift can be written as [84]

$$\begin{aligned} K_\mu &= \frac{1}{B_{\text{ext}}^2} (\boldsymbol{B}_{\text{ext}} \cdot \mathbf{A}_f \cdot \boldsymbol{\chi}_f \cdot \boldsymbol{B}_{\text{ext}}) \\ &= \frac{1}{B_{\text{ext}}^2} (\boldsymbol{B}_{\text{ext}} \cdot \mathbf{A}_{\text{dip}} \cdot \boldsymbol{\chi}_f \cdot \boldsymbol{B}_{\text{ext}}) \frac{1}{B_{\text{ext}}^2} (\boldsymbol{B}_{\text{ext}} \cdot \mathbf{A}_{\text{c}} \cdot \boldsymbol{\chi}_f \cdot \boldsymbol{B}_{\text{ext}}), \end{aligned} \tag{4.5}$$

where $\mathbf{A}_{\text{dip}}$ is the dipolar coupling tensor and $\mathbf{A}_{\text{c}}$ is the hyperfine contact coupling tensor. The dipolar coupling tensor depends on the vectors $\boldsymbol{r}$ joining the f-moments

and the μ^+ site, with its components given by

$$A_{\mathrm{dip}}^{ij} = \sum \frac{1}{r^3}\left(\frac{3r_i r_j}{r^2} - \delta_{ij}\right), \tag{4.6}$$

where the sum is over all of the f-moments in the Lorentz sphere. On the other hand $\mathbf{A}_{\mathrm{c}}$ is normally isotropic. Therefore the determination of K_μ along the principal crystallographic directions allows one to extract $\mathbf{A}_{\mathrm{dip}}$ and $\mathbf{A}_{\mathrm{c}}$, with knowledge of the former yielding information about the μ^+ stopping site.

The muon stopping site with fractional coordinates $(\frac{1}{2}\frac{1}{2}0)$ obtained on the basis of Knight shift measurements [84] is different to the one obtained here using DFT, with both of these sites shown in Figure 4.11. However, I argue that my calculated site may also be consistent with the observed scaling of the muon Knight shift. In the analysis of the muon Knight shift it was assumed that the muon stopping site has an axial symmetry, which results in a simplification of Equation (4.5) for fields applied parallel to and perpendicular to the crystallographic c axis. The assumption of axial symmetry constrains the components of the dipolar tensor to satisfy $A_{\mathrm{dip}}^{xx} = A_{\mathrm{dip}}^{yy}$ (which also means $A_{\mathrm{dip}}^{xx} = -\frac{1}{2}A_{\mathrm{dip}}^{zz}$ as the dipolar tensor is traceless). While the calculated muon site has $A_{\mathrm{dip}}^{zz} = -0.128$ T/μ_{B}, in reasonable agreement with the experimental value $A_{\mathrm{dip}}^{zz} = -0.124$ T/μ_{B} [84], it lacks the symmetry assumed in the analysis that allowed this component of the dipolar tensor to be extracted from measurement of the muon Knight shift. This analysis also suggests that there is a significant hyperfine contribution to the field at the muon site, obtaining $A_{\mathrm{c}} = -0.086$ T/μ_{B}. As can be seen in Figure 4.11, applying the symmetry operations of the crystal to the muon stopping site obtained from DFT generates sites that lie approximately along the a axis and b axis respectively. For $\boldsymbol{B}_{\mathrm{ext}}$ parallel to [110] the previous analysis remains valid as, while $A_{\mathrm{dip}}^{xx} \neq A_{\mathrm{dip}}^{yy}$, their sum is still equal to $-A_{\mathrm{dip}}^{zz}$. However, for applied fields in the basal plane, but not along [110], this set of sites will split into two subsets of magnetically inequivalent sites (whereas the previously proposed site would not). Thus, while a full angular scan of the μ^+ precession frequency in the ab plane would be able to distinguish between these two sites, the site calculated here cannot be ruled out on the basis of these Knight shift measurements.

The fact that the site calculated for $CeRu_2Si_2$ is not incompatible with the ex-

perimentally proposed site is reassuring for validity of the muon sites calculated for URu_2Si_2, given that the sites were found to be almost identical for these isostructural compounds. However, I note that assuming a muon site $(\frac{1}{2}\frac{1}{2}0)$ in URu_2Si_2 would result in a nearly-identical estimate for the magnetic field at the muon site as obtained for the calculated site. This is due to the fact that, in the ordered state, the U moments are found to lie along the c axis [156, 157, 158] and therefore the only component of the dipolar tensor we are sensitive to is A^{zz}_{dip}, which is nearly identical for the two candidate sites (the off-diagonal elements vanish due to symmetry in both cases).

4.4.4 Summary

Muon stopping sites were calculated for the heavy fermion systems URu_2Si_2 and $CeRu_2Si_2$. In URu_2Si_2, structural relaxations obtain two crystallographical distinct stopping sites, with the lower energy site sitting close to the minimum of the electrostatic potential of the unperturbed system. However, dipolar field calculations demonstrate that only the lower energy site produces a field that lies along the c axis, which was found to be the case experimentally [134]. Therefore it is proposed that only the lower energy site is realised in practice.

The muon stopping site obtained for the isostructural compound $CeRu_2Si_2$ is found to be the same as the one in URu_2Si_2, but is distinct from the site previously proposed on the basis of Knight shift measurements [84]. However, without further knowledge of the angular dependence of the Knight shift it is not possibile to conclusively distinguish between these sites, highlighting one of the potential limitations associated with determining muon stopping sites experimentally.

4.5 Conclusion

There has been significant progress in the determination of muon stopping sites using density functional theory (DFT) over the past several years. There is a growing list of examples where knowledge of the muon stopping site (calculated using DFT) has formed a vital part of the interpretation of μ^+SR data. There has also been

significant progress in the development on new methods, with much of this work focussed on providing tools to facilitate these types of calculations. My contribution towards this goal is the MuFinder program, which aims to automate the workflow required to calculate muon stopping sites using DFT, thereby making it easier for non-experts to carry out these calculations to support their μ^+SR measurements.

In this chapter I have presented two case studies of muon stopping site calculations that I have carried out. A finding of both of these studies is the similarity of the muon stopping sites for isostructural compounds. (This was also found for the isostructural pair $CoTi_2O_5$ [100] and $FeTi_2O_5$ [101].) This suggests that as the number of applications of DFT+μ grows, it should be possible to estimate muon stopping sites based on those reported for similar systems. These studies also illustrate that it is not necessary to accurately reproduce all of the materials properties within DFT in order to obtain reliable estimates of the muon stopping site. This is a very important result, as μ^+SR is often used to study highly correlated systems whose physics is difficult to capture using DFT.

Although the list of systems for which it is possible to determine the muon site experimentally is relatively small, comparison of these sites with those obtained from DFT+μ is an important step in assessing the reliability of these calculations. The insulating fluorides [36, 37] are a good example of this as is the case of MnSi [98], where the muon stopping sites were independently obtained from measurements of the muon Knight shift and DFT calculations, with both methods yielding the same sites. $Ce_2Ru_2Si_2$ is just one member of a series of heavy fermion compounds in which the muon site has been determined using Knight shift measurements [84] and the other systems in this series would also provide good tests for the accuracy of stopping sites obtained using DFT, especially given the complicated physics in these systems.

Chapter 5

Local magnetism, magnetic order and spin freezing in the 'nonmetallic metal' FeCrAs

This chapter reports the results of muon-spin relaxation (μ^+SR) measurements on the iron-pnictide compound FeCrAs. These measurements indicate a magnetically ordered phase throughout the bulk of the material below T_N=105(5) K. There are signs of fluctuating magnetism in a narrow range of temperatures above T_N involving low-energy excitations, while at temperatures well below T_N behaviour characteristic of freezing of dynamics is observed, likely reflecting the effect of disorder in our polycrystalline sample. Using density functional theory (DFT) and dipolar field calculations a distinct muon stopping site in this compound is proposed. The structural distortions induced by the implanted muon at this site are shown to be minimal, suggesting that the muon remains a faithful probe of the magnetic properties of the system.

This chapter is based on work published in Ref. [159], where polarised non-resonant x-ray scattering data on a single crystal and susceptibility measurements on our polycrystalline sample are also reported. The μ^+SR data in this chapter were collected by collaborators, but all of the analysis of the data and discussion of the muon site is my own.

5.1 Introduction

Landau's Fermi liquid theory is perhaps the closest condensed matter physics has to a "standard model". However, metallic states not described by the Fermi liquid model are known to exist in many strongly correlated electron systems such as doped cuprates, quantum critical metals and disordered Kondo lattices [160]. Iron-pnictide superconductors also show non-Fermi-liquid behaviour, most notably incoherent charge transport above a magnetic spin-density-wave transition, typically found at $T_{\mathrm{SDW}} \approx 150$ K [161, 162, 163]. Recent examples of materials which behave neither as a metal nor an insulator include high temperature superconducting cuprates [164], heavy fermion systems [165, 166], iron-based chalcogenides [167, 168, 169], and oxyselenides [170, 171, 172]. Common to both cuprates [173] and iron-based superconductors [174] is the emergence of high-temperature superconductivity from the suppression of the static antiferromagnetic order in their parent compounds. The interplay between magnetism and unusual electronic transport is also evident in systems exhibiting a quantum critical point (QCP) arising from magnetic frustration [175] and in heavy-fermion superconductors, whose low temperature non-Fermi-liquid normal state most often derives from a nearby antiferromagnetic QCP [176].

The 'nonmetallic metal' [177] FeCrAs is a strongly correlated electron system, with local physics dominated by complex antiferromagnetism, magnetic frustration and charge fluctuations. Thermodynamic measurements show Fermi liquid-like specific heat; but resistivity has a non-metallic character [178]. FeCrAs crystallises in the hexagonal $P\bar{6}2m$ space group [179, 180, 181] with Cr and Fe forming alternating two-dimensional lattices along the c axis (see Figure 5.1). Cr forms layers with the structure of a distorted kagome lattice where the Cr–Cr distances are approximately constant. The Fe layers form a triangular lattice of three atom trimer units. The As is interspersed throughout both the Fe and Cr layers, as well as in between.

Despite strong geometric frustration of the Cr sublattice, these moments are observed to order at $T_{\mathrm{N}} \approx 125$ K with an antiferromagnetic propagation vector of $\boldsymbol{k} = (1/3, 1/3, 0)$. Neutron diffraction [182] suggests that the ordered state has small moments between 0.6 and 2.2 μ_{B} on the Cr atoms and, surprisingly, no detectable

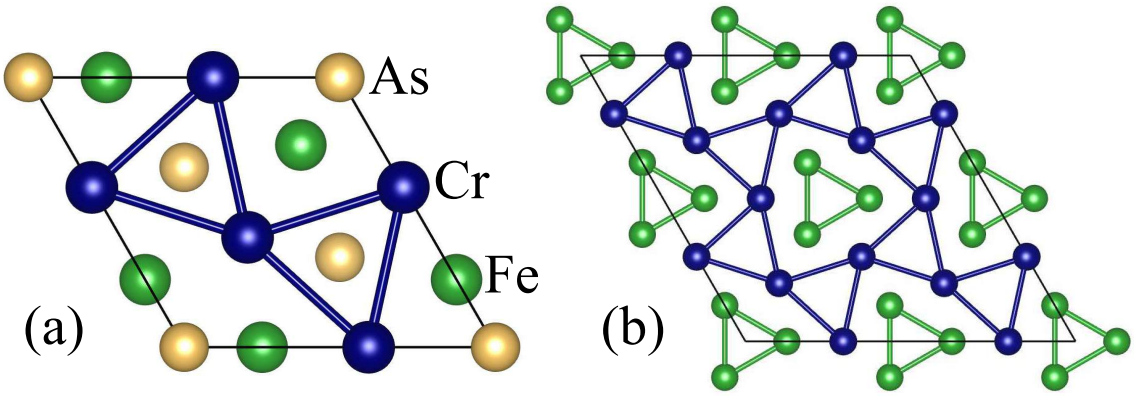

Figure 5.1: Structure of FeCrAs, showing (a) unit cell viewed along the c axis and (b) Fe trimers and Cr kagome planes.

moment on the Fe sublattice. Mössbauer spectra [183] show no magnetic splitting on the iron sites until far below T_N, and even at the lowest temperatures a splitting of only $(0.10 \pm 0.03)\mu_B$ per Fe is observed. (Based on our findings, it seems likely that this tiny moment results from disorder in the polycrystalline samples used.) Fe moments are also absent in x-ray emission spectroscopy, which found a suppressed Fe K β' line [184]. These studies show that, in contrast to iron-based pnictides, any static or dynamic Fe moment in FeCrAs is negligibly small at any temperature.

Theoretical studies have sought to explain the unusual metallic properties of FeCrAs. A model in which Heisenberg spins on the Cr kagome lattice couple either ferromagnetically or antiferromagnetically to Heisenberg spins at the average positions of a trimer results in a phase diagram consistent with the observed magnetic order [185]. A further theoretical study [186] of the system addressed the lack of static moments on the Fe atoms, by assuming that there are well-defined local moments on the Fe sites and showed not only that the Fe sublattice would play a role in stabilising the magnetic order on the Cr sublattice, but that the electronic state on the Fe sublattice could be a $U(1)$ spin liquid phase that survives in the presence of the magnetic Cr sublattice. An alternative "Hund's metal" scenario [187, 188, 189] has been proposed involving localised moments coupling to itinerant electrons. Most recently [189] neutron scattering revealed that, despite the occurrence of magnetic ordering of the Cr sublattice with a mean field critical exponent at low temperatures, the dynamic response resembles that of an itinerant magnetic system at very

high characteristic energies. The high energy scale of these excitations leaves open the possibility that the nonmetallic resistivity of FeCrAs at high temperature arises from scattering from spin and orbital fluctuations which are enhanced by magnetic frustration. Even below T_N, despite the probable absence of magnetic moments on the Fe sites, the fact that the ordered Cr moments are not fully polarised, but rather vary in size between 0.6 and 2.2 μ_B, allows for a scenario involving scattering of the conduction electrons from longitudinal fluctuations of the magnetic moment on the Cr sublattice, giving a possible mechanism for the continuation of the nonmetallic resistivity to the lowest temperatures.

In this chapter, muon-spin spectroscopy (μ^+SR) is used to probe the low-temperature order and dynamics in the magnetic state of FeCrAs. The sample is magnetically ordered throughout the bulk below $T_N = 105$ K, showing no evidence of phase separation. However, there is evidence of low-energy spin excitations entering the time window of μ^+SR below around 130 K, providing evidence of slow spin dynamics in FeCrAs that likely reflect fluctuations of the Cr moments. Below $T = 20$ K a freezing of dynamics is observed, and this likely results from low-level disorder in the polycrystalline samples of this frustrated system. The muon stopping site in this material is calculated using density functional theory (DFT) and it is found that the muon does not introduce any significant structural distortions in this system.

5.2 Experimental

A polycrystalline sample of FeCrAs was prepared by Wenlong Wu and Stephen Julian at the University of Toronto, following the recipe given in Ref. [190]. The sample was obtained by crushing high quality single crystals, and then removing any ferromagnetic grains with a magnet. Such ferromagnetic grains are thought to contain iron inclusions. In subsequent magnetisation measurements on these powder samples no magnetic hysteresis loops, that would be indicative of ferromagnetic domains, were resolved.

Muon-spin relaxation (μ^+SR) measurements were made on a polycrystalline sample using the GPS instrument at the Swiss Muon Source (SμS), Paul Scherrer Insti-

tut, Villigen, Switzerland and at the ISIS facility, Rutherford Appleton Laboratory, UK, using the EMU instrument. Measurements were made at SμS in a He cryostat where the sample was wrapped in Ag foil (thickness 25 μm) and mounted on a fork to minimise any background contribution. Measurements at ISIS were made using a closed-cycle refrigerator where the sample was mounted on a Ag plate to ensure good thermal contact.

5.3 Muon-spin spectroscopy

Example zero-field (ZF) μ^+SR measurements made at SμS on a polycrystalline sample of FeCrAs are shown in Figure 5.2. Below $T = 105$ K, rapid oscillations are present in the early times of the asymmetry spectra, characteristic of quasistatic long range magnetic order (LRO) at the muon stopping site. These oscillations comprise a single frequency, which suggests a single magnetically distinct muon stopping site in the material or, more likely for this system, a single crystallographically distinct site experiencing a range of fields centred on the field corresponding to muon precession frequency. The variance of local fields experienced at this site will then contribute to the observed rapid relaxation of the oscillations. To parametrise the oscillations, the first 0.05 μs of the spectra were fitted to a function

$$A(t) = A_1 e^{-\lambda_f t} \cos(2\pi\nu t + \phi) + A_2, \tag{5.1}$$

where A_1 is the asymmetry due to muons precessing, whereas A_2 reflects muon-spin components aligned parallel to the internal magnetic field along with any implanting the sample holder.

The amplitudes A_1 and A_2 were allowed to vary, but it was consistently found that $A_1 \approx 2A_2$ for all $T < 105$ K. This is expected in a (quasistatic) magnetically ordered polycrystalline sample, where 2/3 of the initial muon polarisation is expected to initially lie perpendicular to the local magnetic field and contribute to the precession signal, while 1/3 is expected to lie along the local field direction and contribute a constant. This suggests that the sample is magnetically ordered throughout its bulk with all muon sites subject to the same magnetic field distribution. Additionally in this measurement, where the sample is mounted on a fork, there is very little

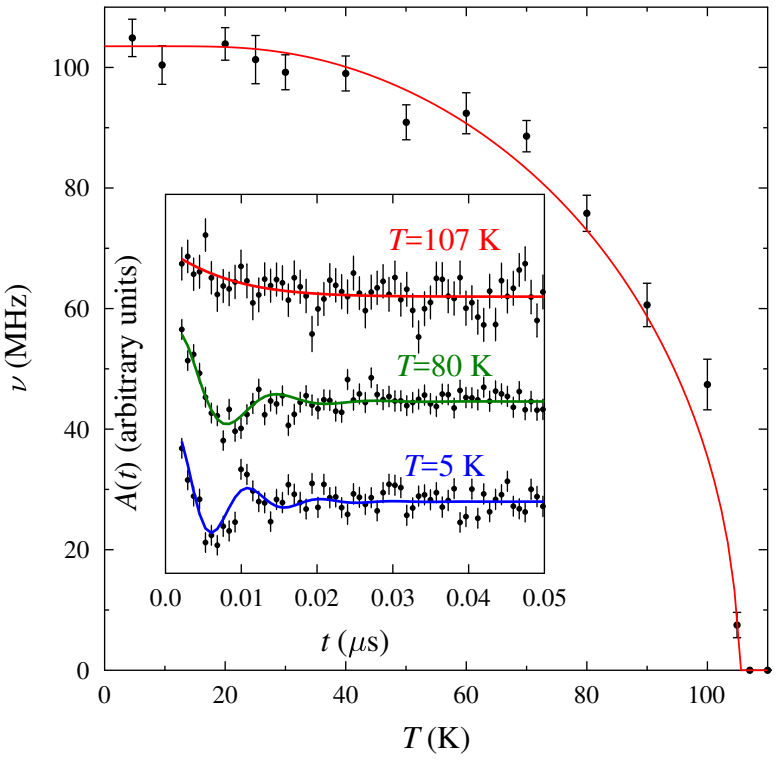

Figure 5.2: Temperature dependence of the precession frequency ν observed in zero-field μ^+SR measurements made at SμS with an $S = 3/2$ mean-field fit. Inset: Data and fits to the first 0.05 μs of the asymmetry spectra measured at several temperatures.

background contribution from the sample holder. A fixed phase offset of $\phi = -62°$, determined from a low-temperature fit, was required to ensure good fits. Non-zero phases, such as those observed here, have been observed in other μ^+SR experiments [191, 135] and often result from an asymmetric magnetic field distribution or, likely in this case, from difficulty in resolving features at early times in the spectra. The relaxation rate λ_f was found to be relatively large and approximately independent of temperature and so was fixed at its average value $\lambda_f = 173\ \mu s^{-1}$.

In light of recent neutron diffraction measurements, where mean-field-like behaviour was reported [189], the extracted muon precession frequency was fit according to mean-field theory. An $S = 3/2$ fit, appropriate for Cr^{3+}, yielded $T_N = 105(5)$ K and $\nu_{sat} = 104(1)$ MHz for the saturation magnetisation. This value of T_N is somewhat lower than the transition temperature of 125 K obtained from measurements of magnetic susceptibility and heat capacity on single crystals [192], but is in good agreement with magnetic susceptibility measurements made on our

polycrystalline sample [159].

Above T_N the spectra comprise a fast-relaxing component ($\lambda \approx 300$ MHz for $T = 110$ K) and a component that relaxes very slowly (i.e. it is approximately constant on the time scale of the oscillations). On cooling from ≈ 130 K to ≈ 80 K there is a significant increase in the amplitude of the fast-relaxing component, accompanied by a drop of the other. This behaviour is attributed to slow fluctuations entering the muon time window in this regime below.

To investigate the possibility of multiple magnetic phases or other contributions to the muon depolarisation, measurements were made at ISIS in an applied weak transverse field (wTF) of magnitude $B_0 = 2$ mT. This field is small compared to the internal magnetic field below 100 K and so only those muons not in sites subject to the large internal field will be seen to precess at a frequency $\nu_0 = \gamma_\mu B_0/2\pi = 0.28$ MHz. As seen in Figure 5.2, the asymmetry from muons with spin components perpendicular to the internal magnetic field decays within 0.05 μs, so is not resolvable with the time resolution available at ISIS. In the absence of dynamic fluctuations, the 2/3 of the muon spin components perpendicular to the internal fields is therefore expected to be quickly dephased from the spectrum, with the remaining 1/3 fixed along the large, static internal field direction and contributing a constant offset. This gives rise to the so-called 1/3-tail, which can only be relaxed by dynamics in the local magnetic field distribution. The spectra were therefore fitted to a function of the form

$$A(t) = A_{\mathrm{rel}} e^{-\lambda_{\mathrm{osc}} t} \cos(2\pi\nu_0 t + \phi_0) + A_{\mathrm{b}}, \tag{5.2}$$

where the phase ϕ_0 was varied to ensure good fits. The resulting temperature dependence of the relaxing asymmetry A_{rel}, the relaxation λ_{osc} and the baseline asymmetry A_{b} is shown in Figure 5.3.

On crossing T_N from above, the oscillating component of the asymmetry A_{rel} [Figure 5.3(a)] drops slowly by $\approx 15\%$, decreasing from from 22% at 130 K to 7% at 80 K, and does not vary significantly at lower temperatures. (This behaviour of A_{rel} is consistent with the asymmetry measured at SμS in this region described above.) The width in temperature of the change in A_{rel} is much broader than that typically observed in magnetic ordering transitions [23, 193, 194, 195]. However, there is an

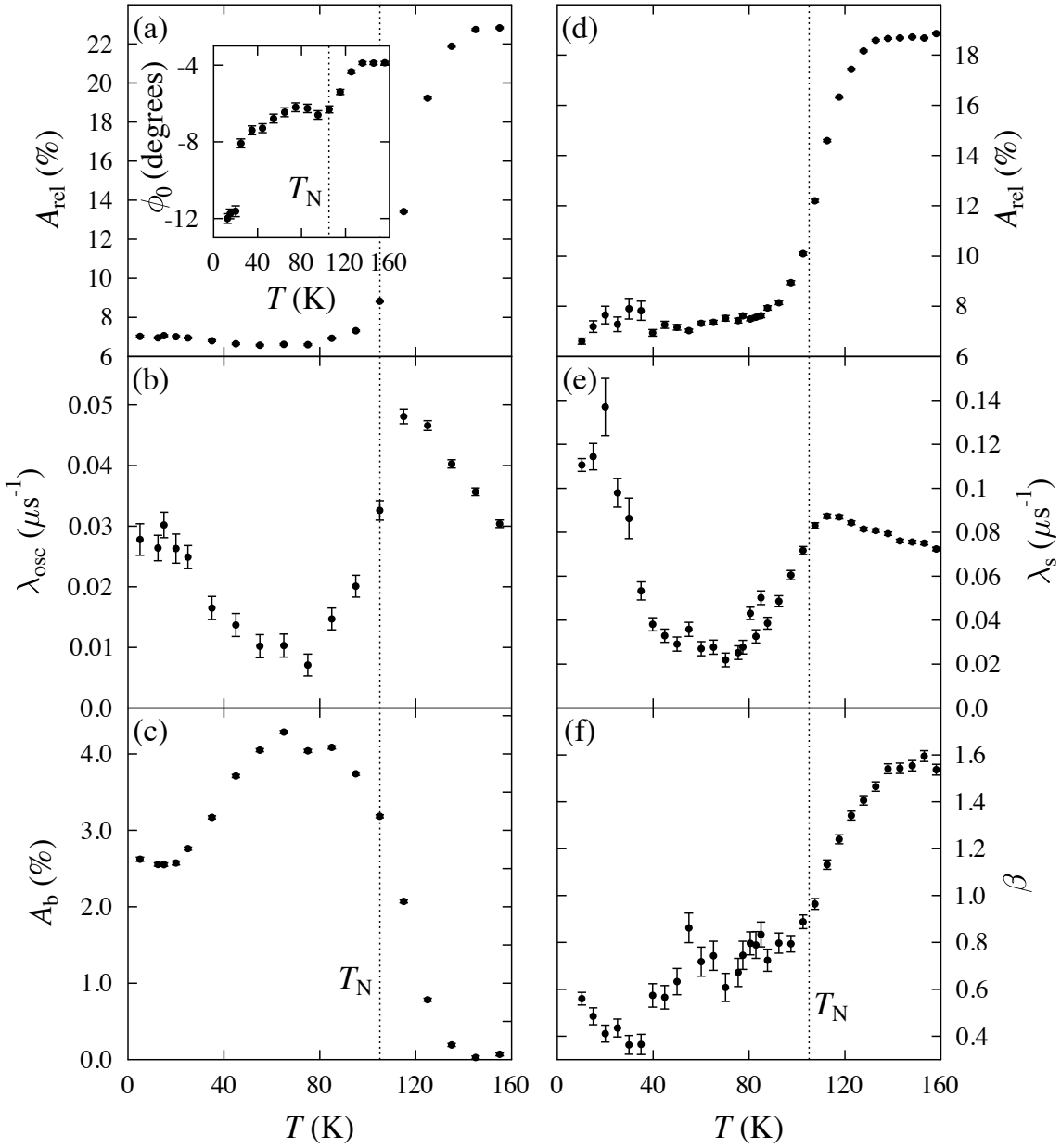

Figure 5.3: Results of fitting Equation (5.2) to the wTF results, showing the temperature evolution of (a) relaxing asymmetry A_{rel}, (b) relaxation parameter $\lambda_{\mathbf{osc}}$ and (c) baseline asymmetry A_{b}. The temperature dependence of the phase ϕ_0 is shown inset in (a). Temperature dependence from ZF measurements of (d) relaxing asymmetry A_{rel}, (e) relaxation parameter λ_{s} and (f) lineshape parameter β.

abrupt change in shape of the spectra measured at SμS at $T = 105$ K, so it is unlikely that the system enters a magnetic state through a broad ordering transition starting at $T \approx 130$ K. Instead the loss of $A_{\rm rel}$ on cooling and the rapid relaxation seen in the SμS data can be attributed to dynamic fluctuations that have spectral density in the muon time window at temperatures $80 \lesssim T \lesssim 130$ K. In the SμS data, the relaxation rate of the fast-relaxing component at $T = 110$ K is $\lambda \approx 300$ MHz, which is sufficiently rapid to dephase this component of the asymmetry at the ISIS time resolution. Approximating the variance of the field distribution by the field measured in the ordered state $\Delta \approx 2\pi\nu(T = 0) \approx 2\pi \times 100$ MHz, this relaxation rate corresponds to fluctuations with correlation times $\tau \approx 10^{-9}$ s. These fluctuations correspond to energies $\Delta E = \hbar/\tau \approx 1$ μeV, much lower in energy than the lowest energy magnetic mode (≈ 3 meV) found using inelastic neutron scattering [189]. The wide temperature range over which the change in $A_{\rm rel}$ occurs implies that the muons experience a range of relaxation rates that result in differing fractions of the asymmetry being dephased from the spectra as a function of temperature. Above $T_{\rm N}$, muons could be subject to magnetic fields with different magnitudes and/or correlation times depending their positions relative to the correlated spins. Additionally, the morphology of our polycrystalline sample, that likely contributes to the low temperature behaviour discussed below, may also result in muons that occupying sites in differently shaped crystallites experiencing slightly different relaxation rates.

The drop in $A_{\rm rel}$ between 130 K and 80 K indicates that 15% of the asymmetry is due to muons in sites where there are large internal magnetic fields well below $T_{\rm N}$. Below $T_{\rm N}$ the only muons that contribute to $A_{\rm rel} = 7\%$ are those where there is no large magnetic field. These could reasonably be attributed to muons stopping in the sample holder, but might include muons that stop in regions of the sample where there is no strong magnetic field. The relaxation rate $\lambda_{\rm osc}$ is very small and is consistent with being due to fluctuations in small fields experienced by those muons not subject to the large internal magnetic field. The rate $\lambda_{\rm osc}$ shows a maximum slightly above the ordering temperature and a minimum around 80 K.

The baseline asymmetry offset $A_{\rm b}$ [Figure 5.3(c)] is very small above $T \approx 140$ K.

It initially increases as temperature decreases down to $T \approx 80$ K, where it reaches a plateau around 4.5%, accounting, approximately, for those 1/3 of muon spins in magnetic sites aligned along the internal field direction. An unusual subsequent drop is seen in A_b on cooling below 50 K. Given that the precession frequency seen in the SμS measurements does not show any anomaly in this region, the drop is suggestive of additional dynamics in the field distribution entering the muon time window and relaxing some fraction of the muon spins. These fluctuations are distinct from those entering the muon time window above T_N as they affect only a fraction of the muons and freeze out on further cooling.

The temperature dependence of the phase ϕ_0 [Figure 5.3(a), inset] likely reflects the fact that the precessing muons experience small fields whose complicated distribution changes when the system orders. In addition to the drop in ϕ_0 close to T_N, there is a large discontinuous change in ϕ_0 at around 20 K, coincident with the slowing of dynamics and freezing discussed in more detail below.

Further ZF measurements were made at ISIS to investigate the low temperature dynamics. Below T_N in these measurements we detect the relaxation of those muons with their spin aligned in the direction of the internal magnetic field (expected to be 1/3 of the total muons for a quasistatically ordered system), that can only be relaxed by dynamic fluctuations. These relaxing spectra change their shape significantly over the temperature regime and so to parametrise them I fit the asymmetry $A(t)$ to a stretched exponential function,

$$A(t) = A_\mathrm{rel} e^{-(\lambda_\mathrm{s} t)^\beta} + A_\mathrm{bg}. \tag{5.3}$$

The background asymmetry A_bg due to muons stopping in nonmagnetic sites is approximately constant and was therefore fixed to the value 3.5%, estimated from a high-statistics fit. (This value differs from the value of 7% in the wTF measurements owing to the sample being remounted for the ZF measurements and covering a different fraction of the muon beam profile.) The temperature dependence of the relaxing amplitude A_rel, the relaxation rate λ_s and the lineshape parameter β is shown in figure 5.3.

As seen in the wTF measurements, there is a change in the relaxing asymmetry A_rel [Figure 5.3(d)] between $T \approx 120$ K and $T \approx 80$ K. Approximately two-thirds

of the relaxing asymmetry is lost on crossing T_N from above, as expected from the arguments above and consistent with the material being magnetically ordered throughout its bulk. The lineshape parameter β decreases with decreasing temperature across the ordering transition. Below T_N the muon experiences approximately exponential relaxation due to electronic moments. Above T_N the electronic moments fluctuate very rapidly and are motionally narrowed from the spectra, leaving the muon sensitive to quasistatic nuclear moments which result in approximately Gaussian relaxation.

The relaxation rate λ_s reaches a local maximum just above T_N due to a sudden increase in the magnitude of the local field from the ordering of electronic moments and the critical slowing of fluctuations, both of which contribute to a large relaxation rate. It then decreases with decreasing temperature before rising sharply below 40 K, peaking at $\approx$ 20 K and remaining roughly constant at lower temperatures. This is suggestive of fluctuations slowing to be within the muon response time, followed by a subsequent freezing below 20 K.

5.4 Muon stopping site

In order to understand the origin of the contributions to the μ^+SR signal, density functional theory (DFT) calculations were carried out to locate the most probable muon stopping sites and assess the degree of perturbation the muon-probe causes in the system. Calculations were carried out using the plane wave basis-set electronic structure code CASTEP [68] within the generalised gradient approximation (GGA), using the PBE functional [67].

A supercell comprising $2\times2\times2$ unit cells was used in order to minimise the effects of muon self-interaction resulting from the periodic boundary conditions. A cutoff energy of 800 eV was used, resulting in total energies that converge at the order of a few meV per supercell and a $2\times2\times4$ Monkhorst-Pack grid [69] was used for k-point sampling. The system was treated as non-spin-polarised; spin-polarised calculations are likely to better capture the magnetic state of the system, but computation times were found to be prohibitive. The structure of the pristine crystal was allowed to

Table 5.1: Lattice parameters and ion positions, taken from experiment [179, 180, 181] and from a DFT calculation (using the PBE functional).

	Experimental	DFT Calculation
a (Å)	6.096	5.905
c (Å)	3.651	3.695
Fe($x0\frac{1}{2}$)	0.2505	0.2502
Cr($x00$)	0.5925	0.5838

Table 5.2: Positions of the muon sites in FeCrAs and their energies E relative to the most stable site. Also listed are calculated average dipolar magnetic fields ν and field distribution widths Δ.

Site	muon position	E (eV)	ν (MHz)	Δ (MHz)
1	Cr layer, inside hexagon	-	88	44
2	Fe layer	0.12	29	9
3	Cr layer, inside triangle	0.40	50	18

relax and the lattice parameters allowed to vary. The experimental and optimised lattice parameters and ionic positions are reported in Table 5.1.

Muons were placed in range of low-symmetry positions and the structure was allowed to relax (keeping the unit cell fixed). The relaxed geometries suggest three distinct candidate low-energy stopping sites (see Figure 5.4) with different energies. These are listed, in order of increasing energy, in Table 5.2.

In the lowest energy site [Figure 5.4(a)], a muon sits within one of the distorted hexagons in the Cr layer. In the second most stable site [Figure 5.4(b)] the muon sits in the Fe layer. This site is 0.12 eV higher in energy than the lowest energy site. The third most stable site [Figure 5.4(c)] is also in the Cr layer, but here the muon sits in the centre of one of the triangles making up the kagome lattice. This site is significantly higher in energy than the other two sites, being 0.4 eV higher in energy than the lowest energy site. For both sites in the Cr layer (sites 1 and 3) the nearest As ion is displaced by ≈ 0.2 Å. Displacements of the Cr and Fe atoms are $<$ 0.11 Å for site 1. The ionic displacements in sites 2 and 3 are generally

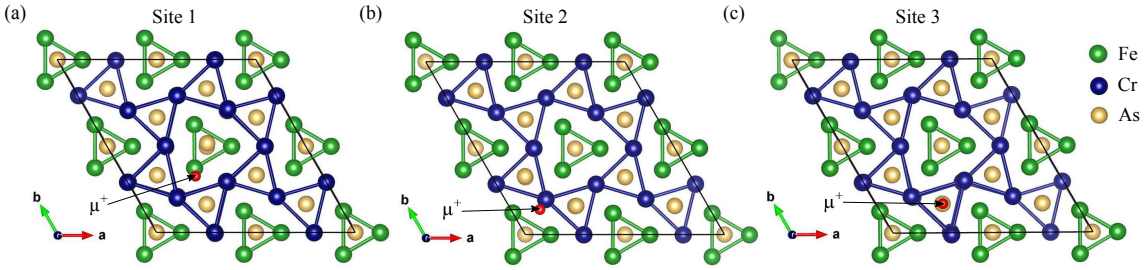

Figure 5.4: Muon positions within the relaxed structure for each of the stable muon sites within a $2 \times 2 \times 2$ supercell of FeCrAs. Sites shown in (a) and (c) involve a muon sitting in the Cr layer. For site 2 shown in (b) the muon sits in the Fe layer.

smaller and are < 0.06 Å for Cr and Fe atoms. The muon-induced displacements of the magnetic ions in this system are slightly smaller than those I have previously calculated for the polar magnetic semiconductor GaV_4S_8 [116] (see Section 4.3), with the displacements of the V ions in this system being between ≈ 0.1 Å and ≈ 0.2 Å and much smaller than those calculated in the molecular spin ladder compound $(Hpip)_2CuBr_4$, where the nearest Cu^{2+} ion is displaced by up to 0.77 Å [196] (see Chapter 6).

In the absence of strong muon–lattice interactions and screening of the μ^+ charge, the minimum of the electrostatic potential provides a good candidate for the muon stopping site [2]. The electrostatic potential for FeCrAs is presented in Figure 5.5. In the Cr layer [Figure 5.5(a)], site 1 is slightly displaced from the local minimum, which may be due to the effect of shielding of the muon or from changes to the potential energy landscape due to ionic displacements induced by the muon (though as discussed above, these displacements are very small). The minimum corresponding to site 1 is seen to be a deeper minimum than the local minimum at site 3, explaining the relative stability of these two sites. In the Fe layers [Figure 5.5(b)] the muon stopping site is also close to the minimum of the electrostatic potential. From the symmetry of this layer it is clear that all of the minima in the Fe layer are equivalent and there is only one distinct minimum.

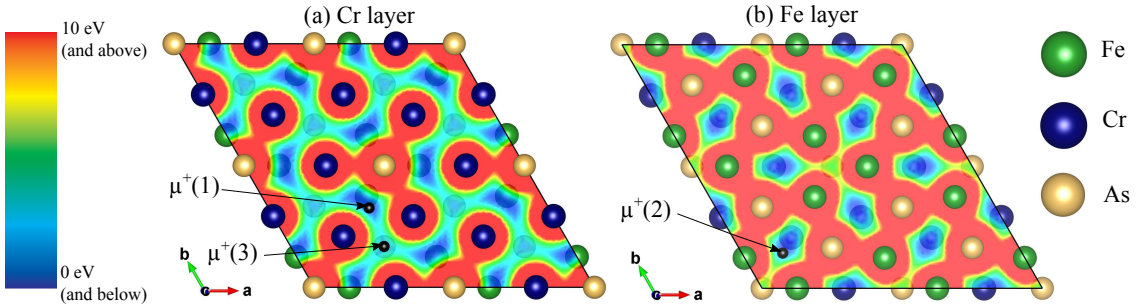

Figure 5.5: The electrostatic potential within (a) the Cr layer and (b) the Fe layer for FeCrAs. Blue colouring indicates regions that are attractive to a positive charge, red indicates regions that repel a positive charge. Also indicated are the positions of each of the stable muon sites. Data are visualised using the VESTA software [154].

5.5 Dipolar field calculations

The magnetic structure of FeCrAs has been determined using neutron scattering [182] and is shown in Figure 5.6. A supercell comprising $3 \times 3 \times 1$ unit cells is required to describe the non-collinear AFM magnetic structure. The magnetic unit cell (MUC) thus differs from the crystallographic unit cell and therefore sites that are crystallographically equivalent are not necessarily magnetically equivalent.

The total magnetic field at the muon site is the sum of dipolar, demagnetising, Lorentz fields and hyperfine interactions. However, as FeCrAs orders antiferromagnetically, the demagnetising and Lorentz field are zero. The dipolar coupling is therefore expected to be the dominant contribution to the field at the muon site. By considering the moments on the Cr sublattice only, the magnitude of the dipolar field (and therefore the expected muon precession frequency) was calculated at each of the muon stopping sites. The non-collinear antiferromagnetic magnetic structure means that each crystallographically distinct site corresponds to a set of magnetically distinct sites, each experiencing a different local magnetic field. For each distinct muon stopping site all of the crystallographically equivalent positions within the MUC were generated. Computing the dipolar field associated with each of these positions allows the average field and field distribution width, $\Delta = \gamma_\mu \sqrt{\langle B - \langle B \rangle \rangle^2}$, associated with each of the classes of muon site to be calculated and these are reported in Table 5.2. Note that these fields have been calculated for the undistorted

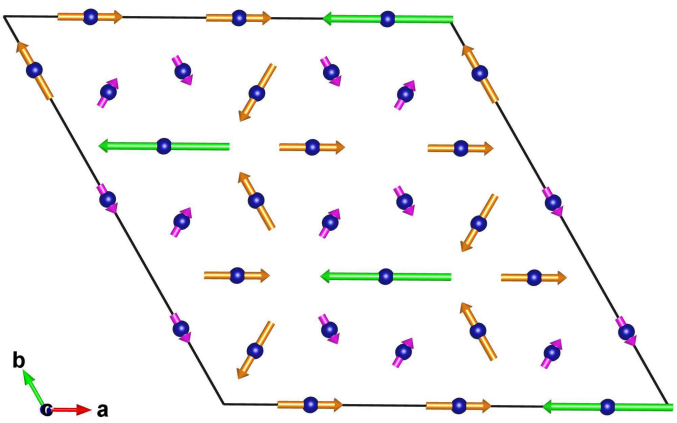

Figure 5.6: The magnetic structure of the Cr layer in a $3 \times 3 \times 1$ magnetic unit cell. Moments of magnitude 0.635 μ_B, 2× 0.635 μ_B and 4× 0.635 μ_B are coloured violet, orange and green respectively. No measurable moments were detected on the Fe sublattice [182].

structure, though as noted earlier, the displacements of the Cr ions due to implanted muon are very small.

The observation of a single muon precession frequency in the μ^+SR measurements suggests a single site being realised, which might be expected to be the lowest energy one. The average dipolar field at the lowest energy site is consistent with the observed precession frequency and so this stopping site is likely to be the one realised in the material. Displacements of the Cr and Fe atoms due to the presence of a muon at this site are small (<0.11 Å and <0.6 Å respectively), with the largest perturbation to the structure being a radial displacement of the nearest As atom of 0.2 Å. The lack of any significant structural distortions suggests that the implanted muon should not affect the magnetism measured in this system.

5.6 Discussion

The μ^+SR results indicate that upon cooling below $T \approx 130$ K magnetic fluctations enter the muon time window that persist down to $T \approx 80$ K. These fluctuations correspond to an energy scale $E \approx 1$ μeV, much lower in energy than the magnetic dynamics measured previously [189]. Measurements made at SμS suggest a picture of this material adopting a magnetically ordered state with a magnetic correlation length long enough for coherent muon-spin precession to be resolved

below 105 K. The observation of a single oscillatory period in the asymmetry provides an approximate lower bound on this magnetic correlation length of around $10a$ (where a is the nearest-neighbor spin separation) [23]. Below T_N the material is quasi-statically magnetically ordered throughout the whole of its bulk, with no sizeable missing fraction of asymmetry (that could suggest phase separation, for example) Moreover, polarised non-resonant x-ray diffraction measurements carried out by coworkers at Durham University [159] confirmed the existence of ordered antiferromagnetism adopted by Cr moments and no detectable moment on the Fe atoms.

Evidence for a spin freezing transition at around 20 K is seen in magnetic susceptibility measurements on polycrystalline samples [159], but in high-quality single crystals a much weaker freezing transition is observed at much lower temperatures (below 10 K). The behaviour of A_b in the wTF measurements [Figure 5.3(c)] and λ_s in the ZF measurements [Figure 5.3(e)] is consistent with this spin freezing transition. This transition must open additional relaxation channels because it provides a means to relax the 1/3-tail rapidly on the ISIS timescale (thus decreasing A_b), with the peak in λ_s suggesting a freezing of these dynamics. Our wTF measurements suggest that the low temperature dynamics do not affect all of the muons. The freezing likely results from disorder in the polycrystalline materials that relieves the frustration and which might be expected to result from strain or surface/edge states in the crystallites. We might speculate that the resulting edge states involve either the fluctuating component of the Cr moments, or fluctuating Fe spins whose moments are not reduced to zero by the unusual collective electronic state adopted by the material. Only those muons close to these spins would then experience the glassy freezing of these spin fluctuations.

5.7 Conclusion

In conclusion, an unusual electronic state is adopted by FeCrAs along with a magnetic structure comprising near-zero magnetic moments on the Fe sites. In the magnetically ordered phase, the material is ordered throughout the whole of its bulk.

Low-energy spin fluctuations enter the μ^+SR time window below around 130 K, providing evidence of slow spin dynamics. Polycrystalline samples undergo an additional freezing of dynamics at low temperatures, likely representative of disorder relieving the frustration in the system.

The spin fluctuations observed in this study correspond to an energy scale $E \approx 1$ μeV and are much lower in energy than the magnetic dynamics measured previously using neutrons [189], demonstrating the importance of a multi-technique approach to study fluctuations at different timescales. This work also demonstrates the complementary nature of μ^+SR measurements made at continuous and pulsed sources, with the large internal fields in the ordered state necessitating the time resolution afforded by a continuous source, whereas the longer time window provided by a pulsed source was required to study the slow dynamics in this system.

The conclusions of this study rely on the notion that the implanted muon faithfully probes the magnetic behaviour of the system in FeCrAs. DFT calculations of the muon stopping sites demonstrate that this is the case, with the muon causing minimal structural distortions to its host (see Chapter 6 for an example of where this is not the case). Furthermore, the dipolar field at the lowest energy muon site calculated using the known magnetic structure [182] is consistent with the measured muon precession frequency, providing evidence that this is indeed the muon stopping site realised in this material.

The DFT calculations also demonstrate that the electrostatic potential of the host crystal provides a good first approximation to the muon stopping sites in this system. Moreover, the symmetry of the unit cell and hence its corresponding potential energy landscape informs the number of crystallographically distinct stopping sites associated with each layer. Consideration of the unit cell symmetries in this manner can significantly reduce the number of initial positions (and hence the computational cost) required to successfully identify all of the crystallographically distinct muon stopping sites and has been subsequently incorporated in the algorithms used within the MuFinder program (see Section 4.2).

Chapter 6

Magnetic phases in the molecular spin ladder $(Hpip)_2CuBr_4$ probed with implanted muons

This chapter reports the results of muon-spin spectroscopy (μ^+SR) measurements on the molecular spin ladder compound $(Hpip)_2CuBr_4$, [Hpip=$(C_5H_{12}N)$]. Using transverse-field (TF) μ^+SR we are able to identify characteristic behaviour in each of the regions of the phase diagram of the strong-rung spin ladder system $(Hpip)_2CuBr_4$.

Probable muon sites are calculated using density functional theory and are crucial to the interpretation of the experimental results. Calculation of the dipolar field at each of the distinct muon stopping sites allows these sites to be mapped to features in the TF μ^+SR Fourier spectra. My analysis suggests that the muon plus its local distortion can lead to a local probe unit with good sensitivity to the magnetic state.

The work presented in this chapter forms part of a collaborative study of molecular spin ladder compounds using μ^+SR, published in Ref. [196]. The μ^+SR data in this chapter were measured and analysed by others working as part of this collaboration, with my contribution being the calculation of the muon stopping sites and the subsequent analysis of the muon states and magnetic field distributions for the interpretation of these data.

6.1 Introduction

Spin ladders represent a class of low-dimensional quantum magnets that occupy a regime of subtle behaviour which lies between the stark extremes of the one-dimensional chain or two-dimensional plane [45]. These materials are characterised by two antiferromagnetic exchange parameters: J_{rung} along the ladder rungs and J_{leg} along the ladder legs. For ladders with an even number of legs the ground states are magnetically disordered and show a gap in their excitation spectrum. [They are often described as quantum disordered (QD)]. An applied magnetic field B_0 acts to close the gap and, at a critical field $B_0 = B_{\mathrm{c}}$, there exists a $T = 0$ quantum critical point (QCP) above which the excitation spectrum is gapless. In a one-dimensional spin system such as an isolated ladder, divergent phase fluctuations prevent the possibility of the high-field, gapless state showing long range magnetic order (LRO) and, instead, a spin Luttinger liquid (LL) state is realised. This gapless LL state is characterised by algebraically decaying spin correlations and, since it involves no symmetry breaking, is reached via a crossover rather than a phase transition for $T > 0$. Despite this, the change in spin correlations has been shown to be observable in thermodynamic measurements [197, 198]. The QCP and related physics in two-leg ladders has been extensively studied theoretically, but there has been comparatively little matching experimental work due to the scarcity of model systems with accessible energy scales. Figure 6.1(a) shows a schematic applied magnetic field-temperature phase diagram for a spin ladder.

Arguably the best studied and clearest example of LL physics has been found in a two-leg spin ladder system: the strong-rung coordination compound piperidinium copper halide $(\mathrm{Hpip})_2\mathrm{Cu}X_4$ [where (Hpip) = $(\mathrm{C_5H_{12}N})$ and X = Br, Cl], whose phase diagrams are shown in Figure 6.1(b). The X = Br compound $(\mathrm{Hpip})_2\mathrm{CuBr}_4$ has [197, 198, 199] $J_{\mathrm{leg}}/J_{\mathrm{rung}} = 0.25$ and a phase diagram that reveals LL, quantum critical (QC) and QD regimes at low temperature, with a critical field, derived from magnetisation measurements, of $B_{\mathrm{c}} = 6.7$ T at $T = 0$. Owing to the existence of a small three-dimensional coupling J' there is also a region of 3D LRO within the LL dome below $T \approx 0.1$ K, where the inter-ladder exchange coupling leads to 3D magnetic ordering reminiscent of that shown by coupled spin dimers in an applied

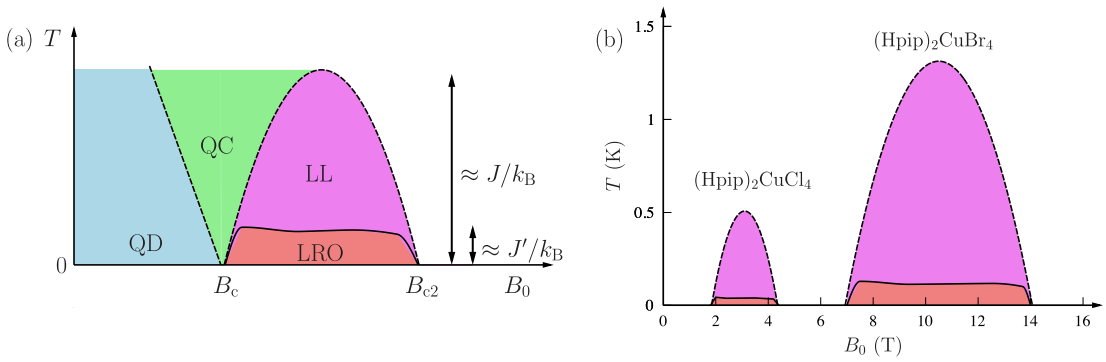

Figure 6.1: (a) Schematic temperature-magnetic field phase diagram for strong-rung spin ladder compounds. The coherence scale of the order of the exchange parameter J along the legs of the ladder is shown. Weak interladder coupling J' leads to LRO. (b) Schematic LL domes for $(Hpip)_2CuX_4$, X = Br and Cl, with the dome height determined via thermodynamic measurements.

magnetic field [200]. Above a saturation field $B_{c2} = 13.8$ T the system becomes gapped, once again.

In this chapter I present local probe measurements of the magnetism in strong-rung spin ladder $(Hpip)_2CuBr_4$. Implanted muons [8, 1] are employed in the transverse field (TF) geometry, intended to probe the static magnetic field distribution in this system. Muon-spin relaxation (μ^+SR) has previously been shown to be a sensitive local probe of static and dynamic effects in one- and two-dimensional coordination polymer molecular magnets [53, 201, 92], in both TF and longitudinal-field (LF) configurations. The technique has also been shown to usefully probe the phase diagram and excitations in systems based on coupled antiferromagnetic dimers [200] and in spin liquid systems [202], whose low energy physics can also be viewed as being related to that of antiferromagnetically coupled, strongly interacting dimers. However, detailed investigations of spin ladders using μ^+SR have not been possible until the recent commissioning of new spectrometers with high magnetic field and low temperature capabilities [22, 203].

There is also a direct and useful correspondence between a spin Hamiltonian in an applied magnetic field and a lattice boson Hamiltonian in the grand canonical ensemble [204], where the applied magnetic field acts as an effective chemical po-

tential for the boson excitations. For the 3D interacting dimer case, this gives us a picture of the magnetically ordered regime as being an analogue of a Bose Einstein condensate (BEC) for magnons. For the 1D spin ladder case, this picture shows that the applied field provides us with a control over the population of excitations within the LL state. The measurements on spin ladders presented here may therefore be viewed as providing a bridge between local probe results on the relatively well understood 3D dimer physics seen in systems such as Cu(pyz)(gly)(ClO_4) [200] and the BEC of magnons candidate $NiCl_2{\cdot}4SC(NH_2)_2$ [205], as well as the more exotic case of spin liquid physics examined, for example, in Ref. [202]. Since spin ladder systems lie between these extremes, an understanding of the muon's interaction with spin ladders is useful in interpreting the results of the more speculative work in the more complex spin liquid systems. Moreover, in cases such as the spin liquids, where μ^+SR has provided unique insights, it is especially important to assess the extent to which the implanted muon has the potential to perturb the intrinsic magnetic state.

I show here the ways in which implanted muons are sensitive to the different phases in spin ladder materials. Notably, my first principles calculations of the nature of the muon stopping site suggest that the muon's sensitivity to the physics in these systems derives from a local distortion it makes to the crystal structure in its vicinity, which leads to a significant perturbation to the local magnetism (though in a quite different manner to that found in pyrochlore oxides [91]). Despite this, the muon continues to prove a useful probe of the global magnetic properties of the materials, allowing us in the case of $(Hpip)_2CuBr_4$, for example, to identify phase boundaries in agreement with those suggested by other techniques.

6.2 Experimental

TF μ^+SR measurements on $(Hpip)_2CuBr_4$ were carried out on single crystal samples at the Swiss Muon Source, Paul Scherrer Institute (Switzerland) using the HAL-9500 high field spectrometer. The crystals had approximate dimensions $5 \times 5 \times 1$ mm^3. These cover the muon beam area for the HAL-9500 spectrometer, leading us to expect very little background signal from muons stopping in the sample holder. The

single crystal samples were wrapped in Ag foil (thickness 12 μm) and glued to a silver sample holder with GE varnish. The holder was mounted on the cold finger of a dilution refrigerator, with the field directed along the b axis (i.e. perpendicular to the ladders, which extend along the a-direction). This is the same orientation used in previous studies, e.g. in Ref. [198]. Data analysis was carried out using the WiMDA analysis program [39], with TF spectra generated using WiMDA's apodised, phase-corrected cosine Fourier transforms.

6.3 Muon spectroscopy measurements

TF μ^+SR measurements were used investigate the phase diagram of the spin ladder system $(\text{Hpip})_2\text{CuBr}_4$. In the high magnetic field limit, the muon spin relaxation rate (and hence the width of the features seen in the Fourier transforms of the spectra) are determined by the magnetic field correlations along the direction of the applied magnetic field. Example Fourier transform TF μ^+SR spectra are shown in Figure 6.2 at two temperatures. At each applied field there is significant Fourier amplitude $A(B)$ [proportional to the field distribution $p(B)$] close to the applied field B_0, but also significant spectral weight displaced from B_0. With increasing applied field the average spectral weight shifts to lower fields. The evolution of the spectral features may also be tracked in the colour map plot of Fourier amplitude shown in Figure 6.3.

In order to extract more quantitative detail from the field distributions, the spectral functions $A(B)$ were fitted to the sum of several peaks. It is found that for $5.5 \leq B_0 \leq 8$ T the data can be best described by a sum of four distinct Gaussian components: two modelling the shape of the large feature whose centre is near B_0, one for the high field side feature seen in the QD region and one for the feature seen on the low-field side of the peak that persists into the LL regime. The spectra were therefore fitted to the function

$$A(B) = \sum_{i=1}^{4} A_i \exp\left[-\frac{(B - B_i)^2}{2\sigma_i^2}\right]. \tag{6.1}$$

The amplitudes A_i were found to be roughly constant with varying applied field, allowing us to track the behaviour of each of the components. Amplitudes were

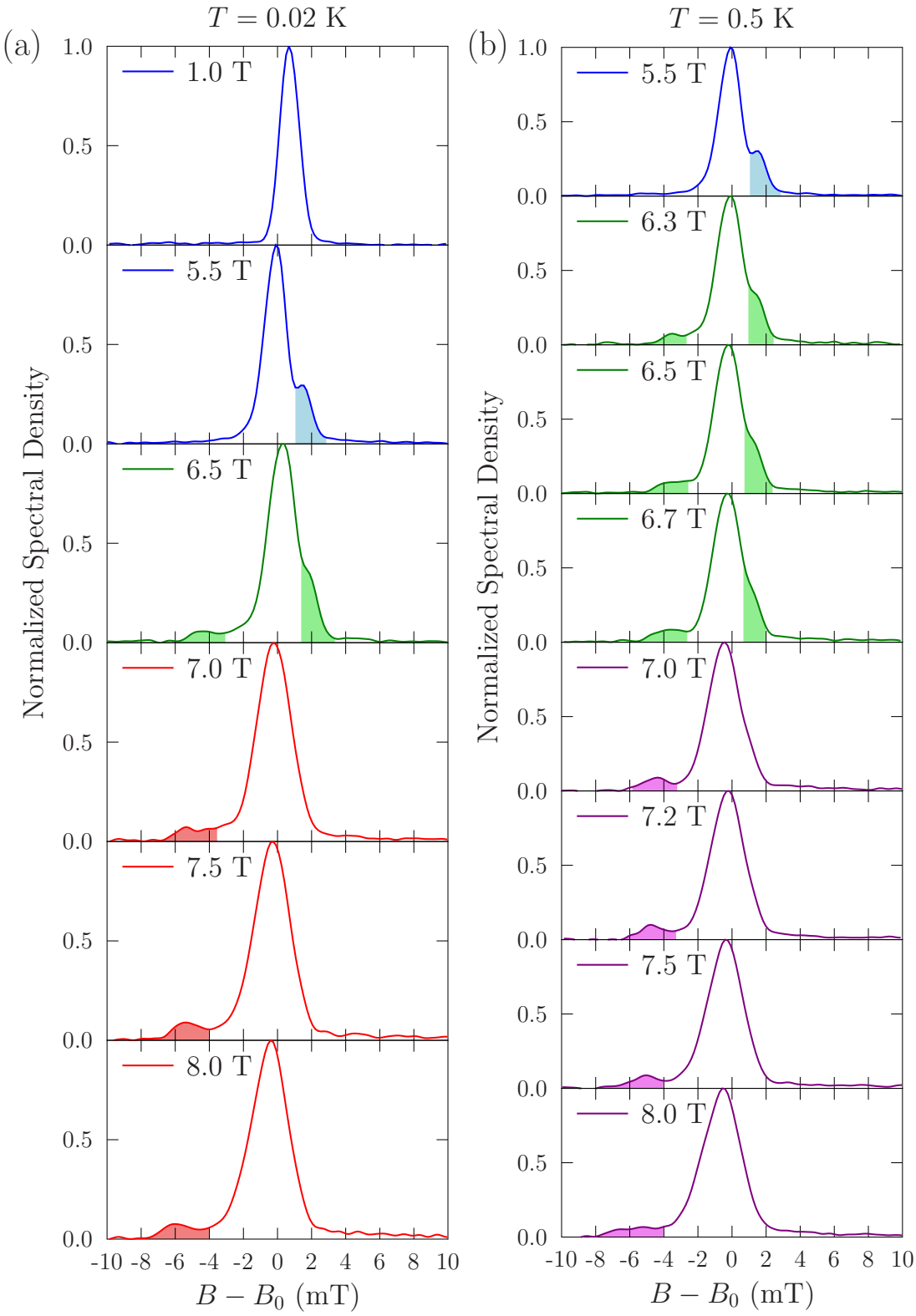

Figure 6.2: Fourier transform TF μ^+SR spectra measured for $(Hpip)_2CuBr_4$ at fixed temperatures of (a) $T = 0.02$ K and (b) $T = 0.5$ K. Colours refer to Figure 6.1(a) and shading highlights the satellite peaks.

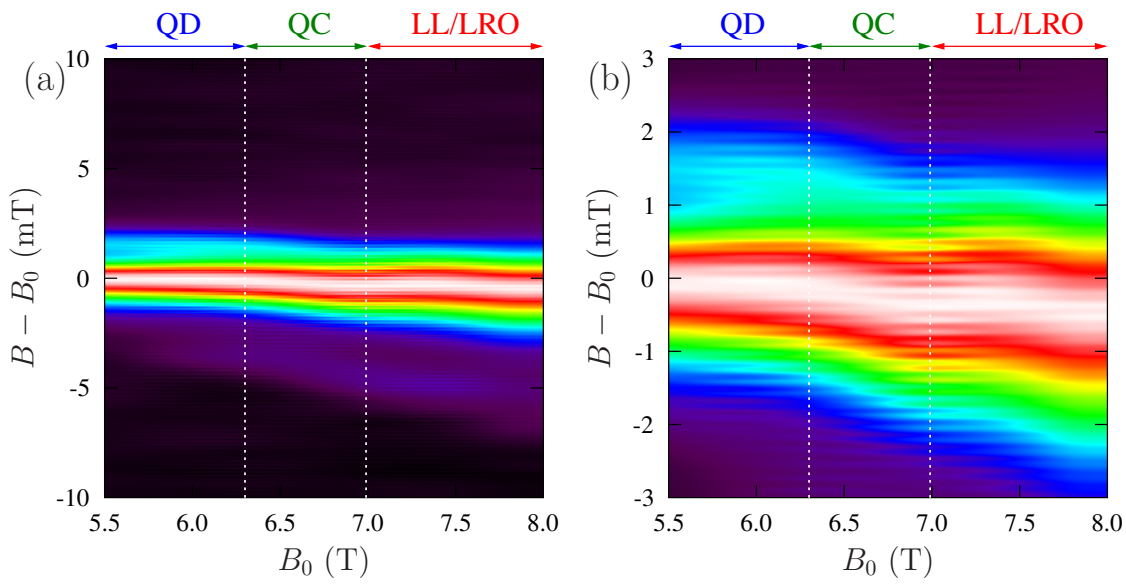

Figure 6.3: A colour map of Fourier amplitude as a function of applied field B_0 for TF measurements on $(Hpip)_2CuBr_4$. Data are shown at $T = 0.5$ K, with (a) a broad vertical scale and (b) an expanded vertical scale. Dotted white lines are guides to the eye showing probable transitions (see text).

allowed to vary slightly in the fitting procedure. There is a drop in the amplitude of the broad central feature when its width increases (rising again when the width decreases) consistent with a constant area of this feature in the frequency domain, and therefore for a constant contribution from muon sites. When the low field feature is no longer resolvable, it is not completely clear whether the spectral weight is lost from the total signal, owing to the relatively small size of this feature compared to the larger contributions to the central peak. However, the broadening out of this feature (and the loss of its spectral weight) would be consistent with the results of the fitting. [It was found that the two central components have similar spectra weight (given by the product $A_i\sigma_i$), with the peaks above and below each having $\approx$15% of that spectral weight.] The position B_i and width σ_i of the peak components are extracted and plotted against applied field B_0 in Figure 6.4 for data measured at $T = 0.5$ K.

Several trends are apparent in the data and the corresponding fits. As the quantum critical (QC) region is approached from the quantum disordered (QD)

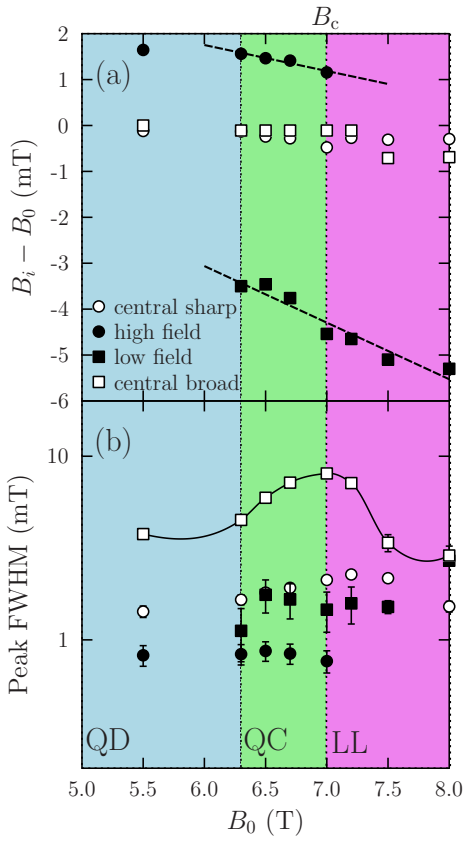

Figure 6.4: Results of fitting Gaussian peaks in Equation (6.1) to the data at $T = 0.5$ K. (a) Peak position B_i relative to the applied field B_0. (Lines are guides to the eye.) (b) Full width half maximum (FWHM) peak widths.

regime on increasing B_0 a high field shoulder is seen in addition to the large central peak. As the field is increased, this feature shifts towards the central line, before merging into the broad central peak above the crossover field $B_c \approx 7$ T. At $B_0 = 6.3$ T and above, we see an additional peak on the low field side, which persists and shifts to still lower fields as the applied field is increased. The broader of the two central features shows a maximum in its width centred on B_c. It is notable that these features correlate with the independently determined phase diagram of the material. The high field feature is visible in the QD and QC regimes and disappears as we pass into the LL/LRO regions. As we leave the QD region and cross into the QC regime, a low-field feature appears which persists into the LL/LRO region. Taking the $T = 0$ QCP to be at the centre of the QC region leads to an estimate

$B_c = 6.7$ T, in broad agreement with the magnetisation result. We are therefore able to broadly distinguish the regimes showing quantum disorder (with the high-field feature resolvable) and LL physics (where this feature is not resolved).

The spectra are generally quite similar for $T = 0.02$ K and $T = 0.5$ K where they reflect the same phases. The most significant differences are seen in the data measured around 6.5 T and 8 T. The former field is close to the QD–QC crossover [Figures 6.1(a) and (b)]. At this applied field, raising the temperature causes a shift in spectral weight to lower fields. This is consistent with the negative slope of the boundary between QD and QC regions [Figure 6.1(a)], which causes the low temperature point to be closer to the QD region and the higher temperature point to be closer to the QC regime. The shift in spectral weight to low fields is then seen to follow the same trend as we find in the constant temperature scans from the QD to QC region, which also involve a shift in spectral weight to lower fields as the applied field is increased. At 8 T the 0.5 K data reflects the LL phase, with a rather broad low field satellite, whereas at 0.02 K the satellite found to be much sharper, reflecting the LRO phase. The overall difference between the LL and LRO phases is however found to be quite subtle.

6.4 The state of the stopped muon

6.4.1 Dynamical Regime

In order to understand the origin of the TF μ^+SR signals reported in Section 6.3 I examine the nature of the stopping state of the muon. Consider first the case of ZF and LF μ^+SR. In most magnets, we are well within the fast fluctuation limit at temperatures above T_N. In zero field measurements we often observe that the electronic fluctuations are partially narrowed from the spectrum (allowing nuclear moments to make a sizeable contribution to the relaxation in zero field). A rough estimate can be made of the muon relaxation rate based on the fluctuating amplitude of a magnetic field component at the muon site and the fluctuation time τ. In a fast fluctuation regime with dense magnetic moments and relaxation dominated by exponential correlations [8] we expect the muon polarisation $P(t)$ to relax following

an exponential function $P(t) = \exp(-\lambda_{\mathrm{LF}} t)$ with the LF relaxation rate given by

$$\lambda_{\mathrm{LF}} = \frac{2\gamma^2 \Delta B^2 \tau}{\omega_0^2 \tau^2 + 1}, \tag{6.2}$$

where $\omega_0 = \gamma B_0$, B_0 being the applied field and γ the muon gyromagnetic ratio. If there are several distinct muon sites in a material, then we would expect a relaxation rate λ_i for a particular site i, to reflect the fluctuating magnetic field ΔB_i at that site, along with the correlation time for the site τ_i. The relaxation of the muon site would then follow $P(t) = \sum_i a_i \exp(-\lambda_i t)$, where a_i reflects the occupancy of each site.

Within the same approximation, the TF relaxation is given by the Abragam function [8], which in the fast fluctuation limit also predicts exponential relaxation with a transverse relaxation rate

$$\lambda_{\mathrm{TF}} = \gamma^2 \Delta B^2 \tau \tag{6.3}$$

and a corresponding Lorentzian lineshape in the frequency domain. Assuming that, for a particular site, transverse and longitudinal field-field correlations are of the same order of magnitude, we may compare a transverse relaxation rate of $\approx 10\ \mu\mathrm{s}^{-1}$ with a typical longitudinal one of $\approx 0.1\ \mu\mathrm{s}^{-1}$ [196], from which we obtain an estimate of the characteristic parameters $\Delta B \approx 50$ mT and $\tau \approx 5$ ns (corresponding to $\gamma \Delta B \tau \approx 0.2$, confirming the original assumption of being in the fast fluctuation limit). This would imply that there is at least one muon site experiencing significant dynamic fluctuations of this amplitude. Dipole field calculations based on the muon site analysis below (see Section 6.4.4) are fully consistent with this estimate.

Besides this evidence for a fast fluctuating dynamical response in at least part of the spectrum, the TF measurements are also sensitive to any time averaged field component along the applied field direction. Evidence for such quasistatic fields is provided by the shifted satellite features found in the spectra.

6.4.2 Muon sites

To identify the specific classes of muon stopping state I carried out spin-polarised density functional theory (DFT) calculations within the generalised gradient approximation (GGA) using the PBE functional [67]), using the plane wave basis-set

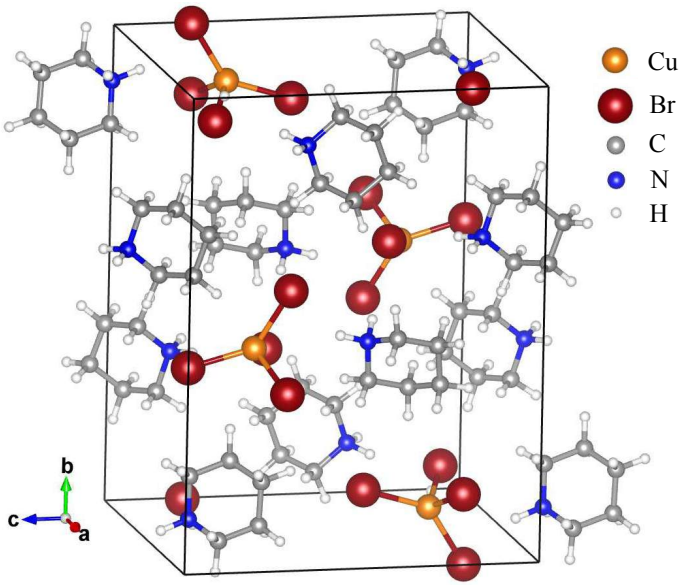

Figure 6.5: The unit cell of $(Hpip)_2CuBr_4$, comprising $(CuBr_4)^{2-}$ tetrahedra and $(C_5H_{12}N)^+$ counterions.

electronic structure code CASTEP [68]. A plane wave cutoff energy of 1000 eV was used, resulting in energies that converge to a precision of $\sim$ 10 meV per cell and Brillouin zone integration was performed at the Γ point.

$(Hpip)_2CuBr_4$ crystallises in the monoclinic space group $P2_1/c$ space group [206], with $a = 8.487(2)$ Å, $b = 17.225(3)$ Å $c = 12.380(2)$ Å and $\beta = 99.29(2)°$. The unit cell comprises flattened $(CuBr^{2-})_4$ tetrahedra and $(C_5H_{12}N)^+$ counterions and is shown in Figure 6.5. Structural relaxations were performed using a $2\times1\times1$ supercell. Doubling the simulation cell along the shortest dimension reduces the spurious self-interaction of the muon which results from the use of periodic boundary conditions. Furthermore, this results in a simulation cell that is equivalent to the magnetic unit cell of this system, thereby allowing us to better assess the effect of the implanted muon on the magnetic structure.

The muon was placed in 52 different initial positions (for both charged and neutral cells) forming an equally spaced three-dimensional grid spanning distinct positions within the conventional unit cell. Positions where the muon would be < 1 Å away from another atom were discarded as starting points. The structure plus implanted muon was then allowed to relax until the forces on the atoms were all $< 5\times10^{-2}$ eV/Å and the total energy and atomic positions converged to 2×10^{-5}

eV and 1×10^{-3} Å, respectively. The structure without the muon was relaxed in the same manner, such that any atomic displacements result from the presence of the muon, rather than differences between the experimental structures and the one obtained from DFT.

I first consider the case of diamagnetic μ^+. Relaxation of the supercell plus the implanted muon yields, as might be expected for a molecular material, many candidate muon sites that are close in energy. I find three characteristic stopping sites based on the local geometry around the muon position and show each of these in Figure 6.6. (I) In the lowest energy sites the muon sits between two Br atoms forming a rung of the spin ladder [Figure 6.6(a)] (called the *rung sites* below). The resulting Br$-\mu^+-$Br-like structure is similar to the F$-\mu^+-$F complex [32] commonly formed in other complex systems [35] (and predicted using DFT [36]), although I note in the present case that the two μ^+-Br bonds lengths are unequal. (II) A second class of site has the muon sitting between two Br atoms forming a ladder leg [Figure 6.6(b)] (the *leg sites* hereafter). (III) In the third class of site [Figure 6.6(c)] the muon sits within a $CuBr_4$ tetrahedron (the *tetrahedron sites*, hereafter). Rung sites [Figure 6.7(a)] have the lowest energies lying within a narrow 30 meV range. Leg sites [Figure 6.7(b)] were found to be on average 76 meV higher in energy than the rung sites. Many tetrahedral sites [Figure 6.7(b)] were identified, having energies 43–204 meV higher than the rung sites.

These three stopping sites: rung, ladder and tetrahedron, have many features in common. Most notably, in all cases the muon sits between two Br atoms. This is true even for the case in which the muon lies inside the $CuBr_4$, where the muon sits along an edge of the tetrahedron. I conclude that the Br$-\mu^+-$Br-like state is highly probable for a muon stopping in this material, with the muon consistently found to sit slightly closer to one of the Br atoms than the other.

All of these sites result in significant distortions to the nearby Cu and Br atoms, with the most significant atomic displacements shown Figure 6.6. The lighter spheres indicate the initial positions of the atoms whereas the darker spheres represent the relaxed positions of the atoms. The displacements of all other atoms (not shown) are less than 0.2 Å. In all cases we observe a significant displacement of the nearest

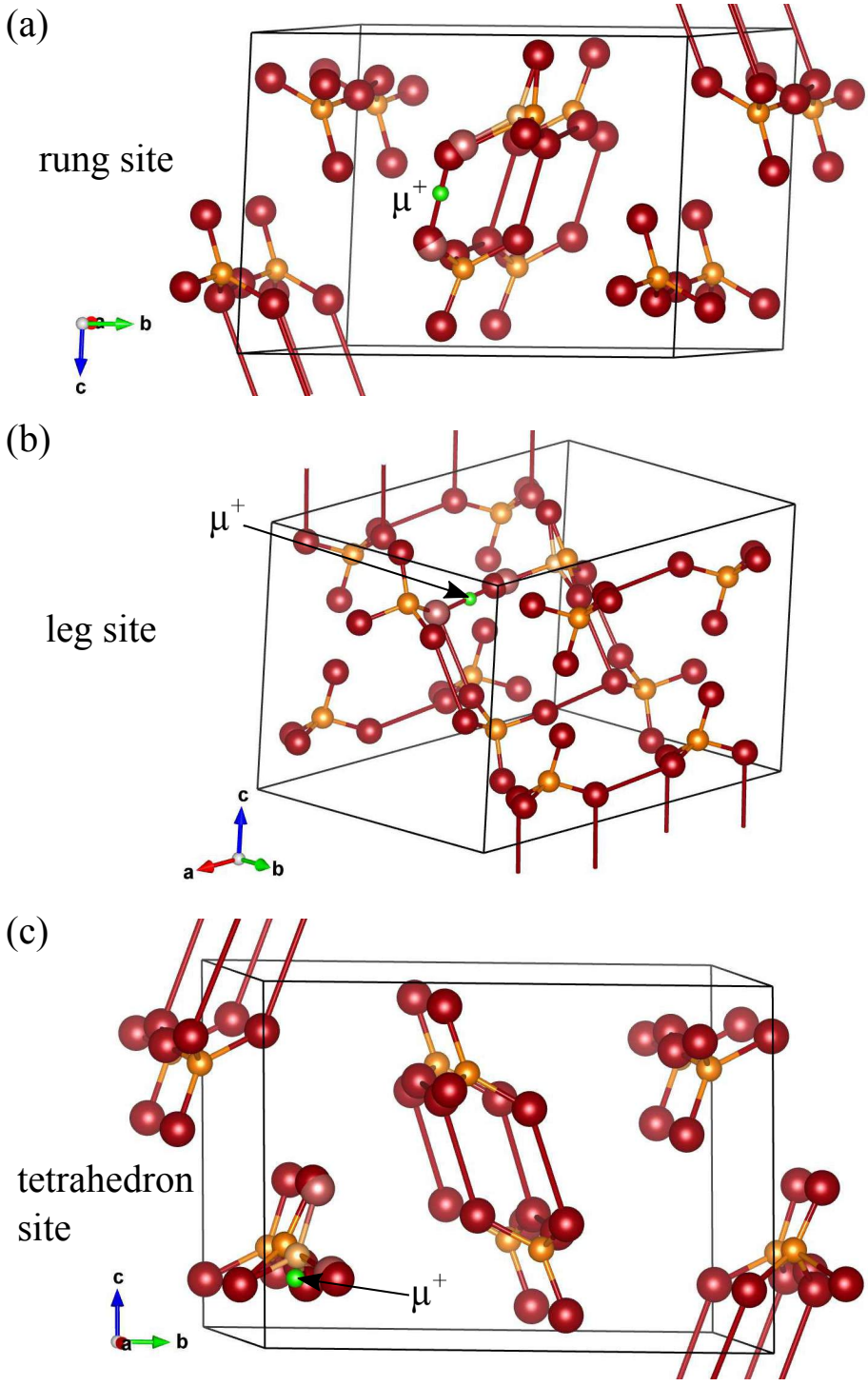

Figure 6.6: Muon stopping sites within the spin ladder structure. Muons were found to stop (a) along ladder rungs (b) along ladder legs and (c) inside the $CuBr_4$ tetrahedra. For clarity, only Cu atoms (orange spheres) and Br atoms (red spheres) are shown.

Cu atom (which can be as large as 0.77 Å), which is accompanied by a stretching of the nearest Cu–Br bond. In the leg and rung sites it is the Cu atom within the tetrahedron containing the Br atom that the muon sits closest to that experiences a significant displacement.

The sites found in the case of muonium (investigated by employing a neutral simulation cell) are very similar to those described above. After relaxation of the structure, there is little electron density found around the muon, with the additional electron density instead moving to the piperidinium ion (close to the N) and the $CuBr_4$ unit closest to the muon. The additional electron density around this Cu ion results in a slight reduction of the Cu moment compared with each of the corresponding cases for diamagnetic μ^+. The spin density around the muon is found to be small for both charged and neutral cells. We therefore expect the contact hyperfine contribution to the local magnetic field experienced by the muon to be small, with dipolar coupling providing the dominant contribution.

Since changes in spin density induced by the implanted muon are likely to have a significant impact on the magnetic properties measured in a μ^+SR experiment, I have compared the calculated spin density of the structure with and without the muon. It is found experimentally that the magnetic exchange coupling is antiferromagnetic along both the legs and rungs and we therefore expect the sign of the spin density to alternate between adjacent Cu ions, as found by neutron diffraction [198]. I note, however, that this is not the magnetic ground state found in my calculations, even for the unperturbed structure, where we find a complicated magnetic ground state involving spins of equal magnitude on each Cu site, with mixed ferromagnetic and antiferromagnetic alignment within the ladders. The failure of DFT to correctly capture the ordered magnetic ground state of this system is perhaps unsurprising, given that the system is found to order only upon the application of a relatively large external magnetic field. Though this fact limits quantitive analysis, the impact of the implanted muon on the spin density can still give us an insight into the magnitude of effects it could have on the magnetic properties of the system.

In Figure 6.7, the displayed isosurfaces represent increases and decreases in spin density. The perturbation caused by the muon probe is quite dramatic: it results

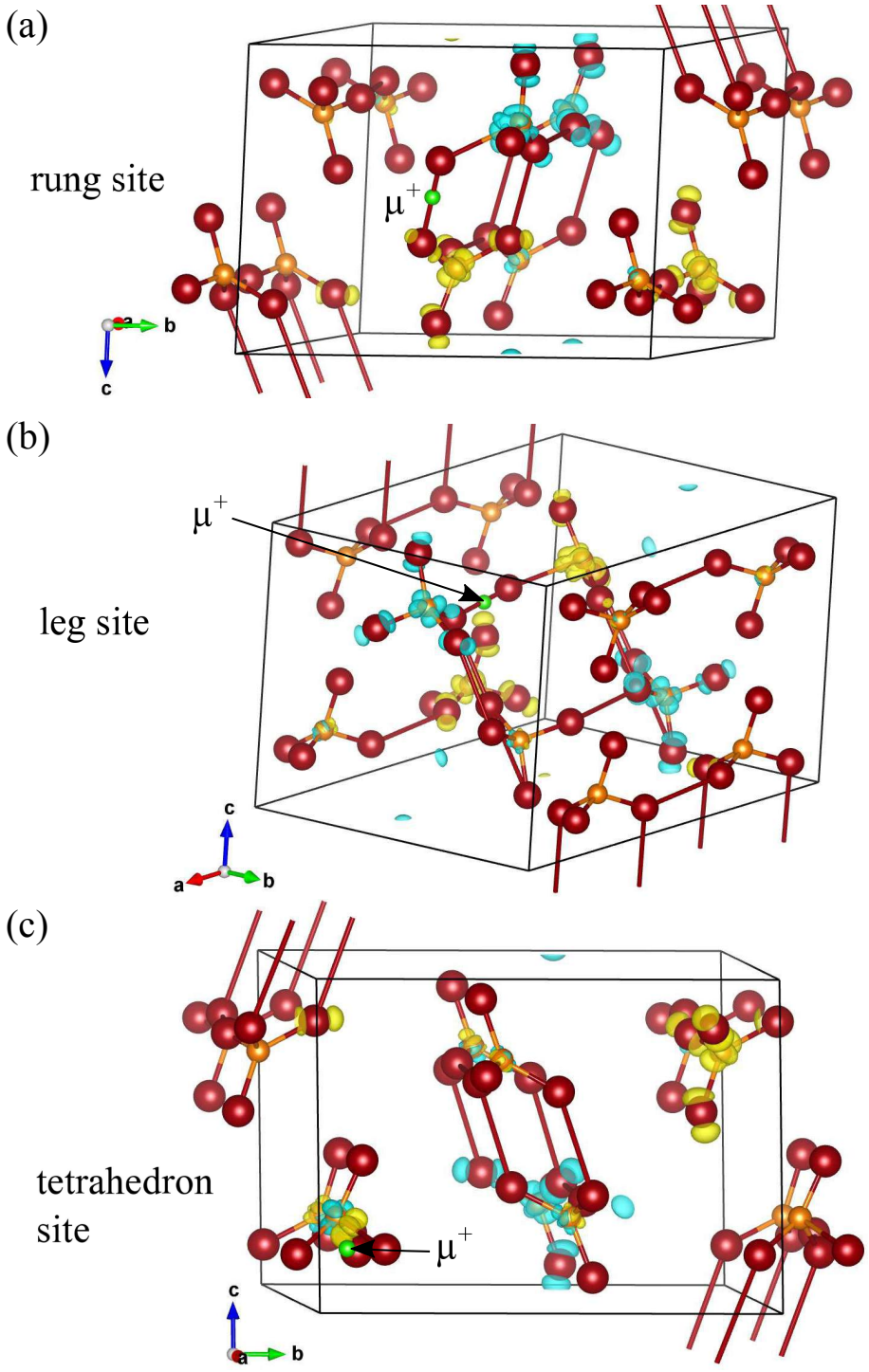

Figure 6.7: Muon stopping sites within the spin ladder structure. Muons were found to stop (a) along ladder rungs (b) along ladder legs and (c) inside the $CuBr_4$ tetrahedra. Yellow and cyan isosurfaces indicate postive and negative changes in spin density respectively.

in the flipping of multiple spins. In each case the spin on four Cu ions close to the muon sites are flipped (note the use of periodic boundary conditions). These spin flips occur for Cu ions up to around 9 Å away from the muon site, indicating a range over which muon-induced distortions to the electronic structure can occur. While most of these changes in spin density are spin flips, the Cu atoms nearest the muon sites that dominate the local field at the muon site show a decrease in the magnitude of their spin. For the rung sites, Mulliken population analysis indicates a 15% reduction of the spin on the nearest Cu ion from $0.34\hbar/2$ to $0.29\hbar/2$. A similar reduction of the Cu spin is seen for the leg sites. The tetrahedron sites see a 25% reduction of the nearest Cu moment, from around $0.33\hbar/2$ to $0.25\hbar/2$. This is likely to reflect the muon's closer proximity to a Cu ion for these latter sites.

To summarise, we identify three distinct muon stopping sites: one where the muon sits along a ladder rung, one where the muon sites along a ladder leg and one where the muon sits inside a $CuBr_4$ tetrahedron. Most importantly for our discussion, each of these sites causes significant structural, electronic and magnetic distortion to the local environment. The perturbation on the local magnetism caused by the muon is also significant, involving a reduction in the local Cu moments and changes in their local spin polarisation over sizeable distances.

6.4.3 Mapping the features in the spectra

We can consider the three muon sites identified above in reconciling the features seen in the TF spectra, where we have four types of muon state: two experiencing local ranges of magnetic fields close to the magnitude of the applied magnetic field (i.e. they see a small average internal magnetic field contribution from the sample) and one either side of these (which experience a larger internal field contribution). Below I discuss how each of these muon states predicted by DFT might contribute to the observed features in the spectra. I argue that the features observed on either side of the central peak are likely to be due to a sizeable perturbation to the system caused by the muon-induced distortion to the system with associated local staggered moments, and identify the rung and leg sites as those most likely to be responsible for these features, owing to the disruption to exchange couplings that they are predicted

to cause in their vicinity. (Note that the structure of the material suggests that there are two exchange pathways along the rung and one along the leg, with the two rung paths related by an inversion center. If the muon is close to one Br, we then expect to find two muon sites coupled to the rungs and two sites coupled to the legs.)

The observed central peaks are of rather different character to the peaks we observe on either side: one central contribution is relatively narrow and one rather broad. The narrow central peak varies relatively little over much of the field range and would appear to result from muon sites not well coupled to the material itself. Sites contributing to this latter peak might include muons stopping outside the sample in the sample holder, or from muons in sites in the sample where they do not experience a significant static internal local magnetic field. I do not discuss these sites further as they provide little information about the system. The broader peak is better coupled to the magnetic behaviour, showing a maximum in its width on passing through B_c which suggests a dynamical origin. Sites in which a muon sits close to the $(C_5H_{12}N)^+$ ions might reasonably produce these central peaks as a result of the muon sitting further away from the Cu ions and thereby experiencing a relatively small internal local field. However, such sites were not found in my calculations, even with the muon being initialised close to the piperidinium rings, with the exception of one site which was found to be around 2 eV higher in energy than the low energy muon sites. I therefore conclude that such a site is unlikely to be realised. This is to be contrasted with calculations performed on the strong-leg spin ladder system $(C_5H_9NH_3)CuBr_4$ [207] which demonstrate sites where the muon was able to form a C$-\mu^+$ bond, breaking the ring. Calculations performed on an isolated piperidinium ion showed a similar ring-breaking and bond formation. This implies that the formation of the μ^+-Br bond is so energetically favourable in the current case that muon sites not involving this coordination are unlikely to occur. In the absence of sites near the carbon atoms, I tentatively attribute the broad central peak to muons stopping in tetrahedron Br$-\mu^+-$Br sites. Whereas the perturbation of the rung and leg sites is identified as being necessary for the associated spectral features we observe, muons in the tetrahedron sites do not sit directly along the magnetic exchange pathways and thus might be expected to perturb the system

much less strongly than the rung and leg sites.

The two features appearing on either side of the central lines result from muon sites that couple to the physics of the spin ladders, as the features correlate strongly with the known phases of the material. In the QD region we observe a feature shifted to the high-field side of the central peak, while in the LL/LRO regions we see a feature on the low field side. Note that the discontinuity in the field shift on passing through B_c, the difference in slope of their field dependence [Figure 6.4(a)] along with the appearance of both features simultaneously in the QC region would strongly suggest that they do not arise from a single feature in the spectra that moves continuously as a function of applied field, indicating that they each require separate explanations. If we consider a muon site in the crystal and the region of the material around it, the total local magnetic field experienced by the muon will be the vector sum of the externally applied field B_0, internal field from the surrounding pocket of material B_{int}, the Lorentz field B_L from more distant moments and the demagnetising field B_{dem}. Approximating the sample as a flat plate, we would expect that $B_{\text{dem}} = -\mu_0 M$, where M is the magnetisation, and that the Lorentz field will be given by $B_L = \mu_0 M/3$. The field at the muon site is then $B = B_0 - 2\mu_0 M/3 + B_{\text{int}}$.

The unperturbed QD region, formed from interacting antiferromagnetic dimers, should give no internal magnetic field at the muon site arising from the Cu^{2+} spins and should have magnetisation $M = 0$ and so we would therefore expect $B = B_0$. The unique signal we observe on the high-field side of the central peak in this phase must therefore result from a small additional contribution to the magnetisation or internal field. One possible source of a small magnetisation identified in the BEC compound DTN [205] was that a small misalignment of the crystal with respect to the applied magnetic field can lead to a small non-zero magnetisation M, however no such effect has been reported for our material. In order to observe a peak at positive $B - B_0$, we require a positive contribution to B_{int} in a region of the phase diagram where there should be no electronic spins in the unperturbed state. The main candidate for producing such an effect is a muon stopping site such as the rung or ladder state that distorts its local environment to the extent that a hyperfine or dipolar contribution from the local Cu^{2+} moments becomes resolvable. This might,

for example, involve the rung site disrupting the local exchange pathway between the two Cu^{2+} ions in a dimer, or a more general distortion leading to a hyperfine field at the muon site. One rather extreme example of a muon induced distortion, still consistent with the DFT result, would be the breaking of a local dimer by the muon which would result in an unpaired spin near the muon site aligned preferentially along the applied field B_0. Such a distortion was also suggested to be the case in μ^+SR measurements on the double chain compound $KCuCl_3$ [208]. There a TF signal comprising seven frequencies was observed at low temperature with a temperature dependence suggestive of unpaired Cu^{2+} spins. However no comparable spectral structure or temperature dependence is observed here.

6.4.4 Spectra in the LL and LRO phases

I now turn to the features on the low field side of the central peak that are most evident in the LL and LRO phases. In the LRO phase in the spin ladders [198] at 8.6 T, the spins are aligned perpendicular to the a axis and antiparallel within the ladder, but parallel on ladders of the same type [propagation vector $\boldsymbol{k} = (0.5, 0, 0)$]. The ordered moment is 0.41 μ_B per copper ion. Increasing the applied field in the region $B_0 > B_c$ cants the AF order parallel to B_0. Thus the magnetisation rises rapidly and via the negative contribution from the sum of the Lorentz and demagnetisation fields, should be expected to result in the appearance of a new peak at low field which moves to still lower frequency as the field is further increased, as we observe. Thus, the low-field peak which is seen at fields exceeding B_c has a separation from the central peak which increases proportionally not to B_0 but to $B_0 - B_c$ and thus tracks the chemical potential of the bosonic excitations.

However, just as in the QD region, it is unlikely that the muon probe coupling passively to the field of the local magnetic moments provides the entire explanation here. This is because the low field feature is seen not just in LRO phase but also in the LL phase, where there should not be magnetic order. In the LL phase there will be some magnetisation owing to correlations that locally resemble the spin configuration in the ordered phase, leading to a larger contribution $-2\mu_0 M/3$ from the Lorentz and demagnetising fields. However in this phase the local magnetic field

will be rapidly fluctuating on the muon time scale. Moreover, the distortions close to the muon described above will still be active and might be expected to produce a distortion in the local magnetism of the LL electronic state, as has been previously suggested theoretically [209, 210]. In fact, there is experimental evidence for such states in the low temperature behaviour of the 1DQHAF dichlorobis (pyridine) copper (II) ($CuCl_2 \cdot 2NC_5H_5$ or CPC) [211]. In this case, shifts in the TF μ^+SR spectra were attributed to muon-induced perturbations to the spin chain. The physics here involves the muon moment causing a significant perturbation to the local exchange links, leading to a local susceptibility which differs markedly from that of the rest of the chain [209, 210]. In the case of CPC, where a powder sample was measured, peaks were resolved on both sides of a central peak, attributed to site dependence of the sign of the hyperfine field, with the fact that the sample was a powder causing a dipolar broadening only, and no shift in the peak position.

The occurrence of both satellite features in the QC region provides evidence that the low field feature does not simply track the macroscopic magnetisation, since the appearance of the low-field feature below B_c suggests that the muons are sensitive to LL correlations and that these start to form on the muon response scale in the $6 \leq B \leq 7$ T region.

Assignment of the features in the TF spectra was facilitated by calculations of the local magnetic field at each of the three sites. Since the muon has a large zero-point energy due to its small mass, we expect quantum delocalisation across the closely spaced members of each group of sites, thus the properties of the effective quantum delocalised muon site defined by the group of structures can be estimated by taking an average over the group. By exploring the effect of three characteristic modes of magnetic order on the dipolar field at the muon sites we can determine the relative sensitivity of the muon sites to different types of static order and fluctuations. First we explore the effect of a uniform FM order parameter along the b axis, then a staggered AF order parameter in the ac plane directed along c. Finally we take the known canted AF structure for the ordered state of the system, which allows an estimate the size of the local dipole field at the candidate muon sites in the LRO region.

Table 6.1: Summary of the three muon sites and the average sensitivity of their local fields to different modes of correlated ordering of the Cu moments, expressed in units of mT/($\mu_{\mathrm{Cu}}/\mu_{\mathrm{B}}$). Field directions $B_\perp$ and $B_\parallel$ are relative to the b axis, which is the orientation of the applied field in the experiments. Large $B_\perp$ values are associated with strong relaxation in the LF configuration and large $B_\parallel$ values are associated with strong relaxation and significant spectral shifts in the TF configuration.

Site	Energy	Number of	FM[a]			AF[b]			Canted AF[c]			
	(meV)	structures	$\lvert B_\perp\rvert$	$B_\parallel$	$\lvert B\rvert$	$\lvert B_\perp\rvert$	$B_\parallel$	$\lvert B\rvert$	$\lvert B_\perp\rvert$	$B_\parallel$	$\lvert B\rvert$	$0.41B_\parallel$
Rung	0	6	6	2.0	6.6	18	$\pm$5.6	19	8.9, 15	$-$2.1, 5.2	9.1, 16	0.9, 2.1
Leg	76	6	1.4	$-$22	22	20	$\pm$2.7	20	13, 14	$-$19, $-$15	21, 23	$-$7.7, $-$6.3
Tetrahedron	140	21	85	$-$64	140	130	$\pm$34	150	99, 130	$-$71, $-$27	130, 150	$-$33, $-$11

[a]FM moments along the b axis.

[b]AF moments along the c axis.

[c]Canted AF mode (Thielemann *et al.* [198]), the final column lists the predicted field shifts in mT for the TF spectrum with the LRO moment of 0.41 μ_B.

My dipolar field calculations are summarised in Table 6.1. The large transverse field fluctuation amplitude $B_\perp$ found for the tetrahedron site is expected to dominate the LF relaxation, with the greatest sensitivity being seen for AF or canted AF spin fluctuations. When considering the TF spectra this site also has the largest $B_\parallel$ coupling, giving a large negative shift for uniform moments polarised along the b axis. The final column in Table 6.1 gives the TF spectral shift for the known LRO structure, which allows the satellite spectral features of Figures 6.3 to be clearly assigned. We see that the observed +2 mT feature corresponds to the rung site and the −6 mT feature corresponds to the leg site.

The results of the dipolar field calculations indicate that a straightforward assignment of the satellite features can be made, the high field feature being from rung sites in an environment with quasistatic local canted AF order and the low field satellite from leg sites within the same quasistatic local canted AF environment. The presence or absence of each of these features in the different phases reflects an interplay between the muon-induced perturbation at each site and the underlying state of the system.

As noted above, impurity-induced local AF order is a known property of chain systems, thus its presence in response to the more strongly perturbing muon sites across a large part of the phase diagram is not entirely surprising. A key question is why such an effect disappears for the rung site in the LL/LRO phase as well as for the leg site in the QD phase. One possibility is that the presence of the muon in the rung sites site leads to a distortion that reduces the size of the local spin gap. This would explain the appearance of the low field feature at fields below B_c and also to the occurrence of a feature in the QD region. Another possible explanation for the disappearance of the static features is that dynamical interaction between the muon-induced moments and the QD and LL/LRO phases leads to fast spin fluctuation and removes the static component of the field at the respective muon sites in these phases. The precise mechanism for this behaviour is unclear at present and it is clearly an area that would benefit from further theoretical investigation.

In conclusion, it is difficult to reconcile the features we see in the spectra without invoking a significant distortion to the local electronic structure caused by the

implanted muon. The two stopping sites lying along the exchange pathways, both found via DFT calculations, provide such distortions. However even in the presence of this local distortion, we obtain here the striking and important result that the nature of the resulting stopping state allows the muon to probe the global, underlying physics of the spin ladder via its response to the perturbing muon.

6.5 Conclusion

The transverse field μ^+SR technique has been shown to be sensitive to the crossover between quantum disordered and Luttinger Liquid regimes in the molecular spin ladder compound $(Hpip)_2CuBr_4$. The muon probes the magnetism of this systems by realising a local magnetic perturbation that results from the distortion to the local structure caused by its electrostatic charge. Despite this modified local character, the muon continues to be a useful probe of the global properties of the system, enabling the phase diagram to be mapped out across a wide range of field and temperature.

These results demonstrate the use of muons as a local probe in higher magnetic fields than are typically employed in standard μ^+SR studies and provide us with an insight into the evolution of behaviour between systems based on interacting spin dimers such as the putative spin liquid states. It is possible that the muon causes significant perturbations to the global magnetic state via the local magnetism in such spin liquid systems (and many others). However, the present results show that these are not necessarily detrimental to the use of the muon as a probe of the broader intrinsic properties, but instead provide a means of probing them via the local magnetism. This is especially important in quantum disordered phases, where in the absence of such a local perturbative probe effect we would expect no magnetic response at all. It is hoped that in future the detailed analysis of muon stopping states in an increasingly diverse range of materials will provide further insight into the ways in which the muon probes its host material, thus allowing a richer level of detail on the properties of the material to be revealed.

Chapter 7

Multiple quantum spin liquid phases in 1T-TaS_2 investigated with muon-spin spectroscopy

1T-TaS_2 has been previously suggested to exhibit a quantum spin liquid (QSL) phase, but the exact nature of this phase remained unclear. In this chapter I report the results of muon-spin relaxation (μ^+SR) measurements on 1T-TaS_2. We identify three distinct phases versus temperature, whose critical exponents are compared with those predicted by QSL models. The intermediate phase between 25 K and 110 K conforms to a Z_2-linear spin liquid model, whereas the behaviours at lower and higher temperatures are consistent with Z_2-gapless spin liquids. The coupling of the muon to the spinons is determined from the muon stopping sites and their associated hyperfine interactions, determined using density functional theory (DFT). The zero-point energy (ZPE) of the muon at each of the stopping sites and the energy barriers between sites are also calculated. These calculations suggest the formation of a quantum delocalised state for the muon between the TaS_2 layers that provides sensitivity to the unpaired spins in two adjacent layers.

This chapter is structured as follows: in Section 7.1 I provide a brief introduction to quantum spin liquid states and the review the evidence for a QSL state in 1T-TaS_2; in Section 7.2 I describe the methods used, while the results of our μSR measurements are reported in Section 7.3. In Section 7.4 I present the results of my

calculations of the muon sites and their associated analysis. I discuss the findings of our μ^+SR measurements and how these can be interpreted in terms of the calculated muon sites in Section 7.5 and finally present my conclusions in Section 7.6.

This chapter is based on joint research. The μ^+SR measurements were made jointly by myself and collaborators and I also carried out the DFT calculations of the muon stopping sites. The results of the μ^+SR measurements were analysed within an interpretive framework devised by Francis Pratt.

7.1 Introduction

7.1.1 Quantum spin liquid states

The presence of strong quantum fluctuations can destablise the ordering of interacting localised magnetic moments even down to $T = 0$ K. The resulting state of matter is known as a quantum spin liquid (QSL) [212] and was first proposed by Anderson in 1973 [213]. Systems with frustrated interactions are particularly susceptible to these effects and much work on highly frustrated systems and their QSL phases has followed [214]. In parallel with the continually expanding body of theoretical work [215] on QSLs, experiments have made good progress recently as various new candidate QSL materials have emerged. For the triangular lattice class these include a number of molecular compounds [216, 202, 217, 218, 219] and also inorganic compounds [220, 221, 222, 223].

A system in which competing interactions cannot be simulataneously satisfied is said to be frustrated. In magnetic systems, geometric frustration occurs when antiferromagnetically (AF) coupled spins sit on lattices comprising triangular motifs. For three spins at the corners of a triangle with AF interactions it is not possible for all of the spins to be antiparallel (see Figure 7.1). The resulting ground-state degeneracy enhances the quantum fluctuations and suppresses magnetic ordering.

Non-magnetic states can be constructed using valence bonds, spin-singlet states of two $S = 1/2$ spins at site i and j given by

$$(i,j) = \frac{1}{\sqrt{2}}\left(|\uparrow_i\downarrow_j\rangle - |\downarrow_i\uparrow_j\rangle\right), \tag{7.1}$$

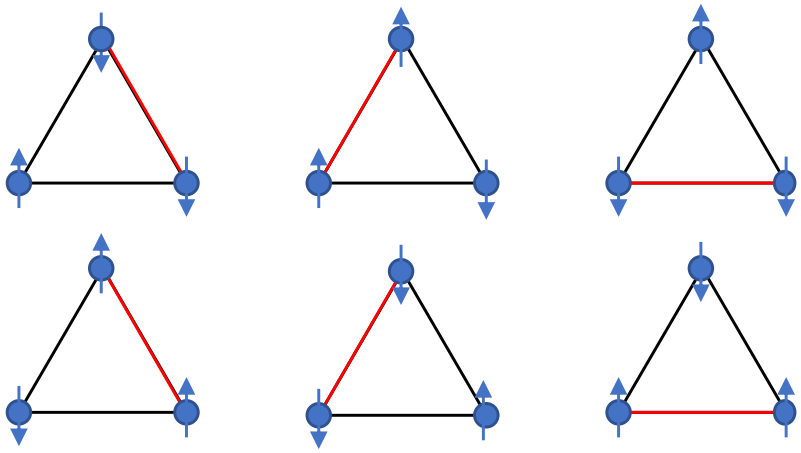

Figure 7.1: In a triangle of antiferromagnetically interacting Ising spins it is not possible for all three spins to be antiparallel. Thus, instead of the two ground states required by Ising symmetry (up or down), we obtain six degenerate ground states as shown in the figure.

which form due to the AF interaction between spins. Each valence bond has zero spin and hence if all of the spins in the system are part of a valence bond the full ground state will have spin 0 and will therefore be non-magnetic. The ground state of the system can then be written as a tensor product of valence bond states,

$$|\Psi_{\mathrm{RVB}}\rangle = \sum_{i_1 j_1 \ldots i_n j_n} a_{(i_1 j_1 \ldots i_n j_n)} \, |(i_1, j_1)\ldots(i_n, j_n)\rangle \,, \tag{7.2}$$

where $(i_1, j_1)\ldots(i_n, j_n)$ are dimer configurations covering the whole lattice. The coefficients $a_{(i_1 j_1 \ldots i_n j_n)}$ are variational parameters determined by minimising the ground-state energy of a model Hamiltonian. If the ground state of the system is dominated by a single dimer configuration it is called a valence-bond solid (VBS). Such a state generally breaks translational or rotational lattice symmetry and is thus not a quantum spin liquid state, which is usually invariant under all symmetry operations allowed by the lattice. If quantum mechanical fluctuations are present, the ground state of the system is a superposition of a large number of different valence bond partitionings and can be regarded as a valence bond "liquid" rather than a solid. This type of wavefunction is known as a resonating valence bond (RVB) state.

Excitations of the RVB ground state involve the breaking of a spin-singlet pair to form a spin-triplet state with an unpaired spin. For a long-range magnetically

ordered state the elementary excitations will be a localised spin-triplet excitation i.e. a magnon. On the other hand, for a QSL, with only short-range spin correlations, the unpaired spins may interact only weakly with each other and behave as independent spin-1/2 excitations called spinons. The existence of these $S = 1/2$ spinons is crucial to the experimental verification of QSLs, with the splitting of a spin-1 magnons into two independent spin-1/2 spinons an example of *fractionalisation*. A systematic way of determining whether a spin model permits such fractionalisation was first proposed by Wen [224, 225], based on the concept of confinement or deconfinement in lattice gauge theory.

Spin liquids are classified according to their gauge symmetries, which can be $SU(2)$, $U(1)$ or Z_2. To illustrate how these symmetries arise I briefly outline how low-energy effective field theories for QSLs are constructed. The discussion here closely follows the approach in Ref. [214]. The RVB wave function in (7.2) has too many variational degrees of freedom to be practically useful and must be simplified. A solution was found [226] by noting that the Bardeen-Cooper-Schrieffer (BCS) states for superconductors are direct product states of spin-singlet Cooper pairs. This suggests that good RVB wavefunctions can be obtained from BCS wavefunctions via Gutzwiller projection [227, 228] P_{G}, $|\Psi_{\mathrm{RVB}}\rangle = P_{\mathrm{G}}\,|\Psi_{\mathrm{BCS}}\rangle$. The Gutzwiller projection removes all doubly occupied components of the BCS wavefunction and freezes the charge degrees of freedom. This type of construction is in fact more general and it is possible to construct fermion or boson representations of spins, with spin wavefunctions obtained from the ground state wavefunction of a trial mean-field Hamiltonian via Gutzwiller projection, $|\Psi_{\mathrm{spin}}\rangle = P_{\mathrm{G}}\,|\Psi_{\mathrm{MF}}\rangle$.

The approach introduced above is complicated by the fact that there exists, in general, many mean-field states $|\Psi_{\mathrm{MF}}\rangle$ corresponding to the same RVB spin wave function after Gutzwiller projection. This gauge redundancy arises due to the enlarged Hilbert space of fermion or boson operators compared to the Hilbert space occupied by the spin operators. For example, the fermion representation of $S = 1/2$ spin operators is given by [229, 226, 230]

$$\boldsymbol{S}_i = \sum_{\alpha\beta} f^{\dagger}_{i\alpha}\boldsymbol{\sigma}_{\alpha\beta}f_{i\alpha}, \tag{7.3}$$

where $\alpha, \beta = \uparrow, \downarrow$ denote the spin indices, $f_{i\alpha}^\dagger$ ($f_{i\alpha}$) are fermion creation (annihilation) operators and $\boldsymbol{\sigma}$ is a vector of Pauli spin matrices. Though the components of $\mathbf{S}_i$ constructed this way satisfy the $SU(2)$ lie algebra $\left[S_i^\lambda, S_j^\mu\right] = i\epsilon_{\lambda\mu\nu}S_i^\nu\delta_{ij}$, where $\lambda, \mu, \nu = 1, 2, 3$ and $\epsilon_{\lambda\mu\nu}$ is the antisymmetric tensor, the local Hilbert space for two fermions comprises four Fock states: $|0\rangle$, $f_\uparrow^\dagger|0\rangle = |\uparrow\rangle$, $f_\downarrow^\dagger|0\rangle = |\downarrow\rangle$, $f_\uparrow^\dagger f_\downarrow^\dagger|0\rangle = |\uparrow\downarrow\rangle$. The single-occupancy constraint

$$\sum_\alpha f_{i\alpha}^\dagger f_{i\alpha} = 1, \tag{7.4}$$

achieved via Gutzwiller projection, removes the unphysical states to obtain a proper spin representation.

The choice of $\{f_{i\alpha}\}$ used to represent the spin operators is not unique, even after choosing the particles statistics and imposing the single-occupancy constraint. For example, the $U(1)$ gauge transformation

$$f_{i\alpha} \to f'_{i\alpha} = e^{i\theta(i)} f_{i\alpha} \tag{7.5}$$

yields a new set of fermion operators $\{f'_{i\alpha}\}$ that form another representation of the spin operators. This gauge redundancy also holds for boson representations of the spin operators. The two gauge-equivalent states correspond to the same state in the spin Hilbert space, they just appear different when represented by particles in an enlarged Hilbert space, with no way of distinguishing between them physically [231]. For fermion representations of $S = 1/2$ spins there also exists an $SU(2)$ gauge structure due to particle-hole symmetry [232]. This gauge redundancy is absent in boson representations.

Consider the isotropic AFM Heisenberg model

$$H = J\sum_{\langle ij\rangle} \boldsymbol{S}_i \cdot \boldsymbol{S}_j, \tag{7.6}$$

where $J > 0$ and $\langle ij\rangle$ indicates that the sum is over nearest neighbour pairs. Using the fermion (spinon) representation of the spin operators in Equation (7.3) the spin exchange operator can be written as [214]

$$\boldsymbol{S}_i \cdot \boldsymbol{S}_j = \frac{1}{4}\sum_{\alpha\beta}\left(2f_{i\alpha}^\dagger f_{i\beta} f_{j\beta}^\dagger f_{j\alpha} - f_{i\alpha}^\dagger f_{i\alpha} f_{j\beta}^\dagger f_{j\beta}\right). \tag{7.7}$$

The Hamiltonian is thus highly interacting in terms of spinons and thus approximate methods are generally required. In the mean-field theory approach it is assumed that the path integral derived from the Hamiltonian in (7.6) is dominated by saddle points characterised by the equal-time expectation values [214]

$$\chi_{ij} = \sum_{\alpha} \langle f^{\dagger}_{i\alpha} f_{j\alpha} \rangle, \quad \Delta_{ij} = \sum_{\alpha\beta} \epsilon_{\alpha\beta} \langle f_{i\alpha} f_{j\beta} \rangle, \quad a^{l}_{0} = \langle a^{l}_{0}(i) \rangle, \tag{7.8}$$

where $\epsilon_{\alpha\beta}$ is the totally antisymmetric tensor ($\epsilon_{\uparrow\downarrow} = 1$). The real auxiliary fields $a^{l}_{0}(i)$ on all sites $i, l = 1, 2, 3$ enforce the single occupancy constraint (7.4). Any time-dependent fluctuations in χ_{ij}, Δ_{ij} and a^{l}_{0} are neglected in mean-field theory.

A more detailed derivation of the mean-field Hamiltonian can be found in Ref. [214], but the final result, written in compact form, is

$$H_{\mathrm{MF}} = \sum_{\langle ij \rangle} \frac{3}{8} J \left[\frac{1}{2} \mathrm{Tr}(u_{\mathrm{ij}} u^{\dagger}_{\mathrm{ij}}) - (\psi^{\dagger}_{i} u_{ij} \psi_{j} + \mathrm{H.c.}) \right] + \sum_{i,j} a^{l}_{0} \psi^{\dagger}_{i} \sigma^{l} \psi_{i}, \tag{7.9}$$

where σ^{l} ($l = 1, 2, 3$) are the Pauli spin matrices and we have introduced a doublet field $\psi = (f_{\uparrow}, f^{\dagger}_{\downarrow})^{\mathrm{T}}$ and a 2×2 matrix

$$u_{ij} = \begin{pmatrix} \chi_{ij} & \Delta^{*}_{ji} \\ \Delta_{ij} & -\chi_{ji} \end{pmatrix}. \tag{7.10}$$

Written in this manner it is clear that the mean-field Hamiltonian is invariant under the local $SU(2)$ transformation

$$\psi_{i} \rightarrow W_{i} \psi_{i} \quad u_{ij} \rightarrow W_{i} u_{ij} W^{\dagger}_{j}, \tag{7.11}$$

which is the same gauge redundancy as the one resulting from the particle-hole symmetry of the fermion representation of $S = 1/2$ spins. Thus, two ansätze of the mean-field Hamiltonian related by an $SU(2)$ gauge transformation, $(u_{ij}, a^{l}\sigma^{l})$ and $(u'_{ij}, a'^{l}_{0}\sigma^{l}) = (W_{i} u_{ij} W^{\dagger}_{j}, W_{i} a^{l} \sigma^{l} W^{\dagger}_{i})$, will yield the same physical spin wavefunction after Gutzwiller projection.

Excitations above the mean-field ground state can be considered by returning to the imaginary time path integral corresponding to the Hamiltonian in (7.3). The mean-field ansatz corresponds a zeroth-order saddle point approximation to the full path integral. In the first-order approximation the fields $(u_{ij}, a^{l}\sigma^{l})$ become dynamical

quantities with their fluctuations describing spin-singlet excitations, usually called gauge fluctuations. The existence of gauge redundancy in these fields suggests that the low-energy fluctuations in spin systems also possess such redundancy. However, unlike the redundancies discussed so far, these will be physically measurable as the gauge fluctuations represent emergent gauge bosons that mediate effective interactions between spinons that are otherwise non-interacting in the zeroth-order mean-field theory [233].

For a given mean-field state there are two kinds of gauge transformation: those that change the ansatz $(u_{ij}, a^l\sigma^l)$ and those that do not. The latter form a subgroup of the original $SU(2)$ symmetry, denoted as an invariant gauge group (IGG) [231]

$$\text{IGG} \equiv \{W_i u_{ij} W_j^\dagger = u_{ij}, W_i \in SU(2)\}. \tag{7.12}$$

For a stable QSL state, physical gapless excitations exist only for fluctuations belonging to the IGG of the mean-field ansatz. Within $SU(2)$ there are only three plausible types of IGG: $SU(2)$, $U(1)$ and Z_2. The corresponding spin liquids are labelled $SU(2)$, $U(1)$ and Z_2 spin liquids. $SU(2)$ spin liquids are expected to be unstable due to the existence of a large number of gapless $SU(2)$ gauge field excitations. $U(1)$ spin liquids are expected to be more stable, but still support gapless excitations. Z_2 spin liquids are expected to the the most stable, with the gauge fluctuations gapped by the Anderson-Higgs mechanism [215].

The spinons themselves can have either a gapped or a gapless dispersion, independent of whether the gauge fluctuations are gapped or gapless. A Z_2-gapped spin liquid is characterised by gapped spinons (which can be either fermions [234, 226] or bosons [235]) together with gapped visons [236], the latter of which are the "vortices" of the Z_2 gauge field. Two further classes of Z_2 spin liquids, both of which are gapless, are classified according to the energy dependence of the spinon density of states (DOS) and are shown in Figure 7.2. A Z_2-gapless spin liquid has a constant density of states arising from either a quadratic spinon dispersion or a large spinon Fermi surface [see Figure 7.2(a)]. In the latter case, the dispersion is weakly linear around the Fermi energy, typically with one branch that increases in area and one branch that decreases in area as E increases, such that the overall DOS remains constant. In a Z_2-linear spin liquid the spinons are gapless at $k = 0$ and follow a

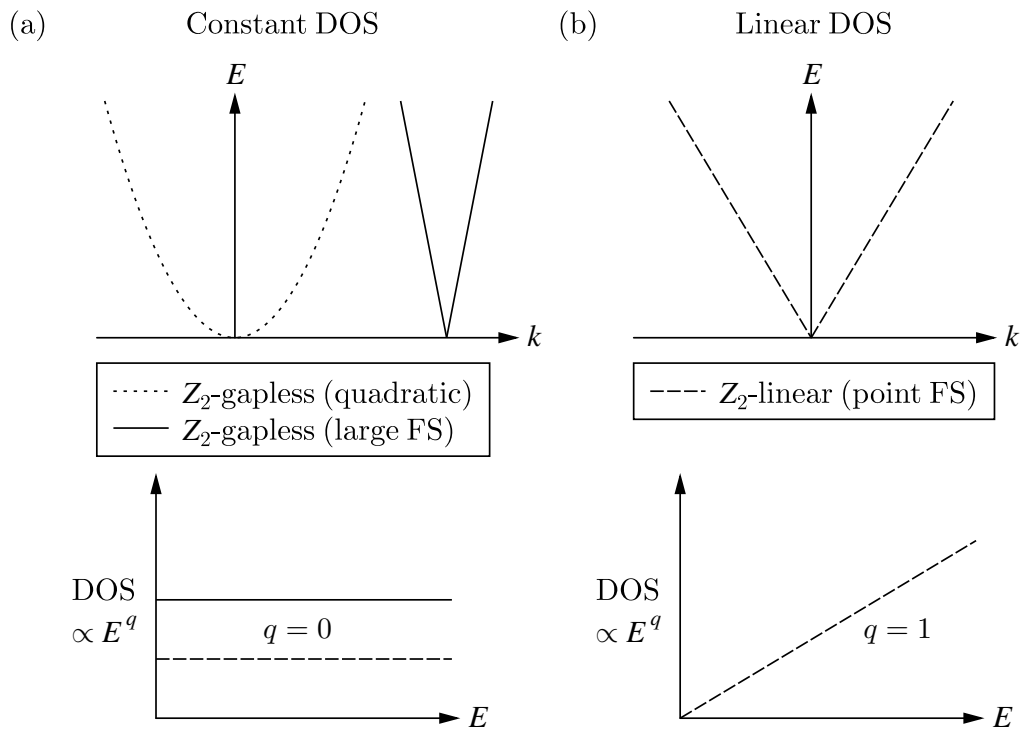

Figure 7.2: Spinon dispersion and density of states (DOS) for two different classes of Z_2 QSL. When $q = 1$ an additional T dependence appears in many properties compared to the case of $q = 0$.

linear spectrum around this point, resulting in a DOS that is directly proportional to energy [see Figure 7.2(b)]. These gapless Z_2 spin liquid models will be relevant to our analysis of 1T-TaS_2.

7.1.2 1T-TaS_2 as a quantum spin liquid

The transition metal dichalcogenide 1T-TaS_2 is a layered compound, with each layer comprising a triangular lattice of Ta atoms which is sandwiched by S atoms in an octahedral TaS_6 coordination, with weak van der Waals interactions between layers. For $T > 540$ K, 1T-TaS_2 crystallises in an unmodulated trigonal structure with space group $P\text{-}3m1$ [237]. Below this temperature, it undergoes a series of structural modulations [238]. First, an incommensurate charge-density-wave (CDW) sets in at $T \approx 540$ K. Upon further cooling a transition to a nearly-commensurate CDW occurs at $T_{\text{nCDW}} \approx 350$ K [239]. The series of CDW phases ends with a fully commensurate C-CDW phase that is stabilised below 200 K. In this phase, the distortion pattern

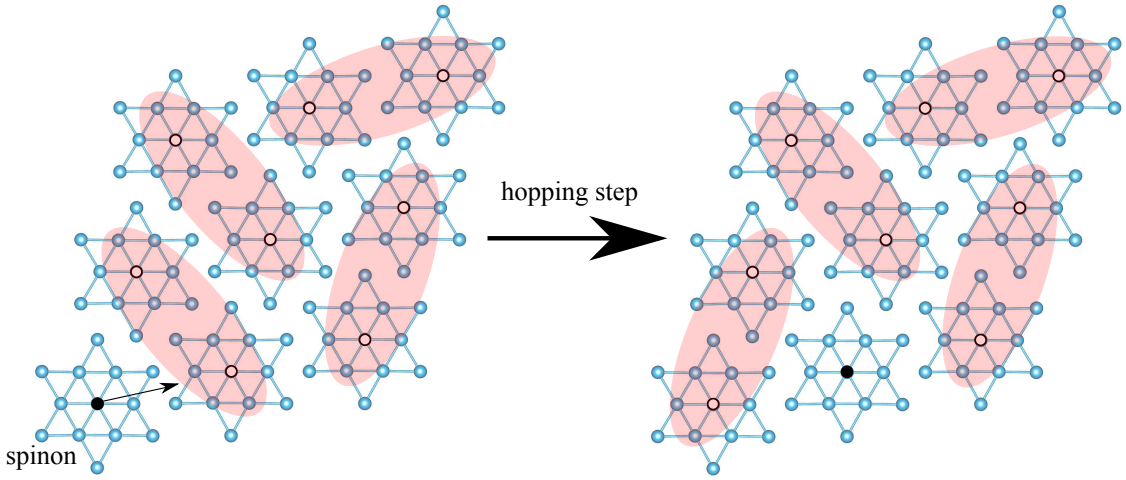

Figure 7.3: In the C-CDW phase, 1T-TaS_2 comprises a triangular lattice of Star-of-David (SD) clusters containiig 13 Ta atoms. Also illustrated is the basic hopping step for 2D spinon diffusion, which involves rearrangement of the valence bonds (VB) adjacent to the mobile spinon.

forms a triangular-lattice of Star-of-David (SD) clusters containing 13 Ta atoms. Each Ta^{4+} of 1T-TaS_2 provides one $5d$ electron, and thus there are 13 $5d$ electrons per cluster [240]. Twelve of these electrons form 6 Ta–S covalent bonds, leaving one unpaired spin-1/2 localised on each cluster (see Figure 7.3).

Experimentally, 1T-TaS_2 is found to be insulating in the C-CDW phase [241]. Studies on 1T-TaS_2 using density functional theory (DFT) have shown that a two-dimensional spin-1/2 Mott phase exists for a monolayer in the CDW state, but that this phase is destroyed by the packing of the distorted layers, leading to a one-dimensional metal for the bulk [242, 243, 244]. This one-dimensional metallic band dispersion has subsequently been shown to exist using angle-resolved photoemission spectroscopy [245]. More recently, DFT calculations have shown that the electronic phase of 1T-TaS_2 and its phase transition are dictated not by the 2D order itself, but by the vertical ordering of the 2D CDWs [246]. These calculations uncovered two competing CDW stacking configurations (one insulating and the other metallic) that are very close in energy, and suggest that the competition between these may be responsible for the metal-insulator transition in 1T-TaS_2.

The expected ordering of the local moments in a Mott insulator into an anti-

ferromagnetic ground state due to exchange coupling is not seen for 1T-TaS_2 [247] and it was one of the materials that originally inspired the RVB theory [213]. Several recent studies have explored further the evidence that it is a quantum spin liquid, both from an experimental and a theoretical perspective [247, 248, 199, 249]. Measurements using zero-field (ZF) μ^+SR have confirmed the absence of magnetic ordering down to 20 mK [248, 199]. Furthermore, the NMR relaxation rate in the C-CDW phase was found to exhibit a power-law temperature dependence $1/T_1 \propto T^2$ for temperatures above 55 K, which suggests a QSL model whose spinon excitations have nodes in k-space [250]. Below 55 K, 1T-TaS_2 exhibits a broad range of ^{181}Ta relaxation rates, suggesting a growing randomness in the spin system as the temperature decreases [250]. However, despite these studies, the exact nature of the QSL phase in 1T-TaS_2 remains unclear.

The existence of a QSL state in 1T-TaS_2 is complicated by the issue of interlayer coupling [247]. Below 200 K, the Star-of-David motifs are stacked directly on top of each other to form bilayers, with these bilayers stacked either randomly or in an incommensurate fashion [248, 251]. If the spins in the bilayer form a singlet then this state no longer fits the description of a spin liquid. This scenario is supported by the results of DFT calculations [242], which suggest that interlaying hopping dominates over intralayer hopping and the system becomes a one-dimensional metal. However, the formation of a dominant interlayer singlet is not supported by the NMR relaxation rate $1/T_1$ measured in Ref. [250], which would show an exponential decay if this were the case (they instead found $1/T_1 \propto T^2$ as noted above). On the other hand, if the spin liquid on each layer is fully gapped a sufficiently weak interlayer hopping will not be able to destroy the topological protection of the QSL state and it will therefore survive.

In this chapter, I report the results of muon spin relaxation (μ^+SR) measurements on high quality samples of 1T-TaS_2. In additional to checking a candidate QSL for magnetic ordering, μ^+SR can also measure critical parameters [202] that can be compared against QSL models. A QSL can be described theoretically in terms of fractionalised spinon excitations and various experimental properties are expected to depend on the characteristics of these spinons. Here we use μ^+SR in

longitudinal magnetic fields (LF μ^+SR) to provide information on the dynamics of spinons diffusing through the triangular lattice (Figure 7.3). The coupling of the muon to the spinons is determined by the stopping sites and their associated hyperfine interactions, which I have computed using density functional theory (DFT). The predictions of the QSL models are also compared with the results of specific heat measurements made by collaborators. Both spinon diffusion and the spinon contribution to specific heat are expected to depend on the nature of the spinon density of states (DOS) (Figure 7.2).

7.2 Methods

7.2.1 μ^+SR measurements

Muon spectroscopy (μ^+SR) measurements were carried out on the HiFi instrument at the ISIS Neutron and Muon Source. A mosaic sample, made from several large crystals of 1T-TaS_2 (0.7272 grams in total) all oriented with the with the ab plane parallel to the surface, was mounted on a silver sample plate, covered with a thin silver foil and then placed in a closed cycle refrigerator. The high-quality 1T-TaS_2 bulk crystals used in this study were synthesised by collaborators at the Instituto de Ciencia Molecular, Universidad de Valencia (ICMol) by chemical vapour transport and characterised using elemental analysis, ICP mass spectrometry and XRD. Data analysis was carried out using the WiMDA program [39].

The muon probe is fully spin polarised on implantation and the forward/backward asymmetry of the detected muon decay positrons $a(t)$, reflects the time dependent polarisation of the muon spin. In the ZF measurements the relaxing component of $a(t)$ was fitted to the product of a Gaussian and a Lorentzian term. The Gaussian term reflects nuclear dipolar relaxation contributions and was estimated at high T and then kept fixed as T varied. The relaxation rate of the Lorentzian term λ reflects the electronic contribution to the muon spin relaxation that varies significantly with T. The electronic contribution is in a fast fluctuation regime where λ is proportional to the electronic spin fluctuation time τ. In the LF measurements the magnetic field was applied perpendicular to the ab plane of the crystals.

Detailed measurements of the field and temperature dependence of the muon spin relaxation were made in this study, counting 5×10^7 muon decay events in each μ^+SR spectrum to get sufficient accuracy in the fitted parameters to estimate critical exponents that can be compared with those of QSL models.

7.2.2 Density functional theory calculations

In order to identify the muon sites and their hyperfine coupling to the unpaired spin, calculations were made using density functional theory (DFT). Spin-polarised calculations were carried out using the plane wave basis-set code CASTEP [68] within the generalised gradient approximation (GGA) using the PBE functional [67]. A $\sqrt{13} \times \sqrt{13} \times 2$ supercell comprising two C-CDW unit cells stacked along the c axis was used for these calculations (the doubling of the c axis is necessary to ensure sufficient isolation of the implanted muon from its periodic images). The C-CDW wave state was obtained by starting from the corresponding structure in Ref. [252] and allowing the ionic positions to relax. I used a plane wave basis-set cutoff energy of 500 eV and a $5\times5\times5$ Monkhorst-Pack [69] grid for k-point sampling, resulting in total energies that converge to an accuracy of 0.01 eV per cell. Muons were initialised in 59 random positions within this supercell, generated by requiring initial positions being at least 0.25 Å away each other and from any of the atoms in the cell. Each structure was then allowed to relax until the change in energy per ion was less than 2×10^{-5} eV and the maximum force was below 5×10^{-2} eV/Å. A neutral cell was used to provide an unpaired spin within the structure and the hyperfine coupling was evaluated for each relaxed site configuration [calculations using a charged (+1) cell were found to give negligible hyperfine coupling].

The zero-point energy (ZPE) of the muon at the stopping site was estimated using the results of phonon calculations carried out using the finite-displacement method. The lowest energy stopping site within each group was further relaxed with a stricter force tolerance of 1×10^{-2} eV/Å to refine the equilibrium geometry used for the phonon calculations. Phonons were calculated at the Γ point only. As the muon is much lighter than the atoms in this system, the highest energy phonon frequencies can be assumed to dominated by the vibration of the muon (inspection

of the corresponding eigenvectors showed that this was indeed the case). Therefore, within the harmonic approximation, the ZPE of muon can be estimated from the sum of the frequencies of the three highest frequency phonon modes.

Energy barriers between muon stopping sites were calculated using transition state searches [253]. Taking two different muon stopping sites as the reactant and product structures, a transition state search is used to identify an intermediate state and hence evaluate the energy barrier between the two configurations. Interpolation to maximum energy is carried out using the Linear Synchronous Transit (LST) method, with the transition state obtained optimised using a conjugate gradient minimisation and then further refined using the Quadratic Synchronous Transit (QST) method.

7.3 μ^+SR results

The muon spin relaxation is relatively slow in this material (Figure 7.4A), as found previously [248, 250, 254]. A detailed study of $\lambda(B_{\mathrm{LF}})$ at fixed T provides information about the character of the spin fluctuations [255]. This method has been used in μ^+SR for studying the propagation of spinons in several spin-1/2 Heisenberg antiferromagnetic chain systems [256, 92], where 1D diffusive motion leads to a weak power law dependence for $\lambda(B_{\mathrm{LF}})$, and the method can easily be extended to systems of greater dimensionality [255].

When a longitudinal field is applied, the nuclear contribution to the relaxation is fully quenched at fields above a few mT, leaving just the electronic contribution. Therefore, the relaxing part of the asymmetry can be fitted to a single exponential decay, i.e.

$$a(t) = a_0 \exp\left[-\lambda(B_{\mathrm{LF}})t\right] + a_{\mathrm{bg}}, \tag{7.13}$$

where the background term a_{bg} accounts for muons stopping outside of the sample. The relaxation rate $\lambda(B_{\mathrm{LF}})$ has a field dependence reflecting the spectral density function of the relaxation process $S(\omega)$ [23], with the spectral density being derived from the Fourier transform of the spin autocorrelation function $\Phi(t)$, i.e.

$$\lambda(B_{\mathrm{LF}}) \propto S(\omega) = \int_0^\infty \Phi(t)\cos(\omega t)dt, \tag{7.14}$$

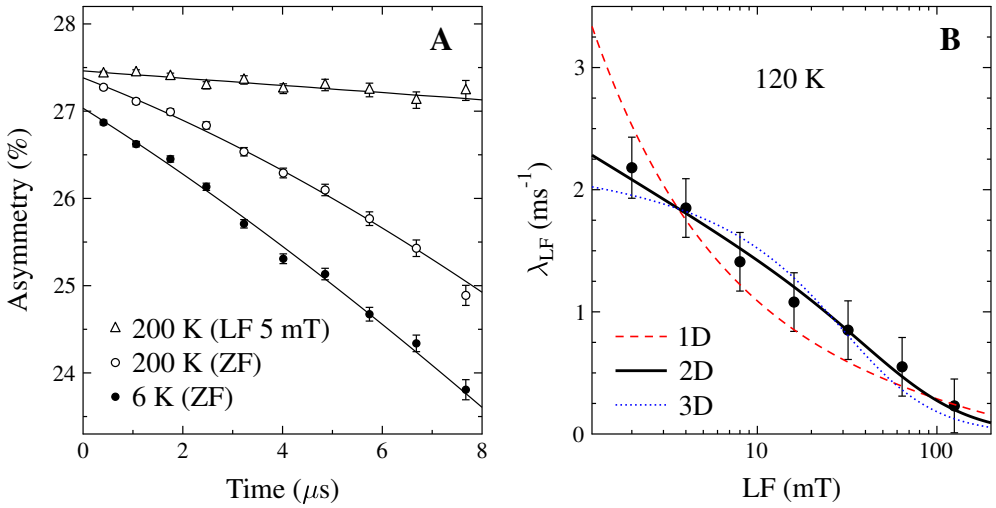

Figure 7.4: (A) ZF muon spin relaxation at 200 K and 6 K and the quenching effect of weak LF on the relaxation rate at 200 K. (B) LF dependence of the relaxation rate at 120 K with fits to 1D, 2D and 3D spinon diffusion models, demonstrating that the 2D model provides the best fit.

where ω is the probe frequency and scales with B_{LF}. To fit $\lambda(B_{\mathrm{LF}})$ in this case a model is considered in which spinons diffuse on an n-dimensional lattice where $n = 1$ is a chain, $n = 2$ is a square lattice and $n = 3$ is a cubic lattice. The spin autocorrelation function is then given by [255]

$$\Phi_n(t) = [e^{-2tD_{n\mathrm{D}}} I_0(2tD_{n\mathrm{D}})]^n \tag{7.15}$$

where I_0 is the zeroth order Bessel function and $D_{n\mathrm{D}}$ is the diffusion rate (more precisely, the nearest-neighbour hopping rate). The corresponding spectral density for n-dimensional diffusion is

$$S_{\mathrm{diff}}(\omega, n) = \int_0^\infty \Phi_n(t) \cos(\omega t) dt. \tag{7.16}$$

Comparison was made between $\lambda(B_{\mathrm{LF}})$ obtained from fits to the measured data made using (7.13) and the form of the $\lambda(B_{\mathrm{LF}})$ predicted by the 1D, 2D and 3D spinon diffusion model, with the data measured at 120 K and the corresponding model fits shown in Figure 7.4B. The 1D model predicts $\lambda(B_{\mathrm{LF}}) \propto B_{\mathrm{LF}}^{-1/2}$, which is clearly inconsistent with the data, whereas 2D and 3D models show much better agreement with the measurements. Careful comparison with the data shows that

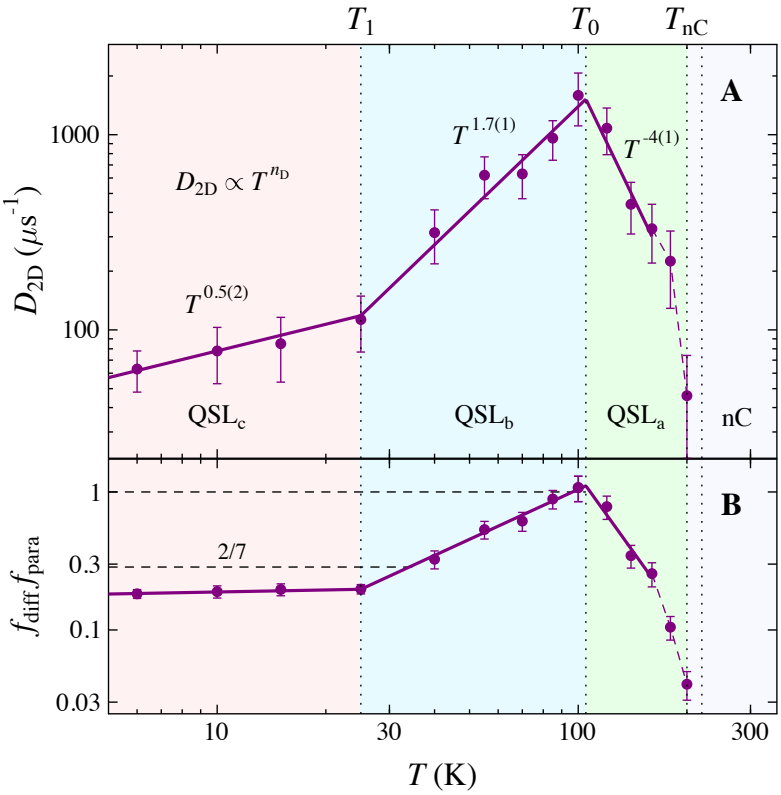

Figure 7.5: (A) Temperature dependence of the 2D spinon diffusion rate D_{2D} obtained from LF μ^+SR. The T exponent depends on the critical parameter ν and the DOS power law q. (B) The product of the diffusive fraction in the LF μ^+SR signal f_{diff} and the fraction of muon sites seeing unpaired spins f_{para}.

at every temperature the 2D model gives a significantly better fit than the 3D model. Thus D_{2D} versus temperature may be obtained from LF scans at a series of temperatures.

In general both diffusive and localised excitations contribute to $\lambda(B_{LF})$. Localised excitations are represented by a Lorentzian spectral density centred on zero field [257], whereas fast-diffusing excitations have spectral density $S_{diff}(\omega)$ extending to higher fields. When the isotropic hyperfine coupling $\bar{A}$ dominates over the dipolar coupling and the diffusion rate is much faster than $\bar{A}$, the diffusive contribution to the LF relaxation rate from the spin-1/2 electronic spins can be expressed as

$$\lambda_{diff}(B_{LF}) = f_{diff} f_{para} \bar{A}^2 S_{diff}(\omega, 2)/2, \tag{7.17}$$

where the probe frequency is the electronic Larmor frequency $\omega = \gamma_e B_{LF}$ with

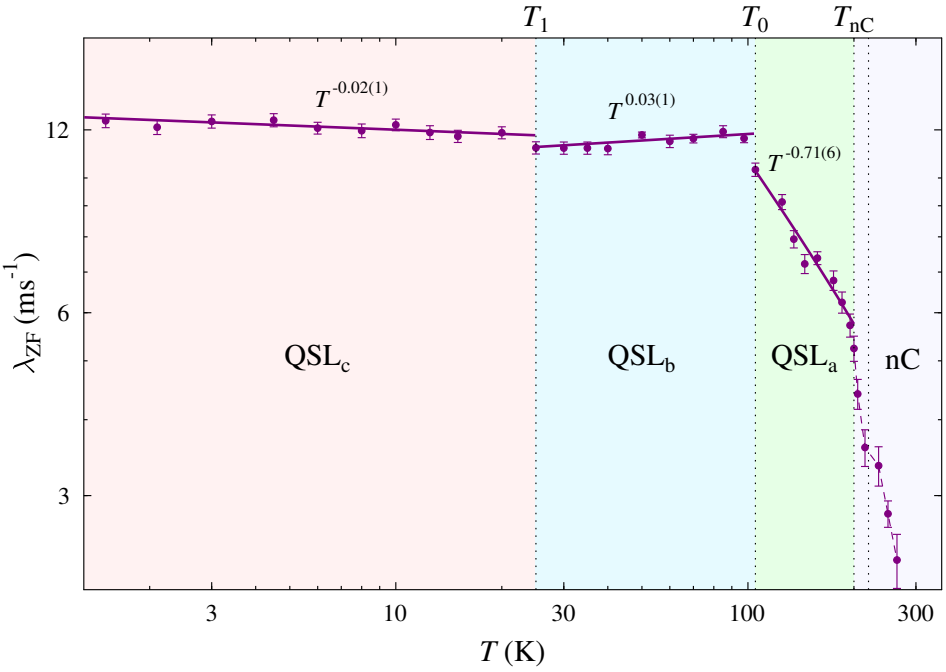

Figure 7.6: Temperature dependent ZF muon spin relaxation shows a significant change in behaviour at T_0 and a more subtle change at T_1.

$\gamma_e/2\pi = 2.802 \times 10^{10}$ s^{-1} T^{-1}, f_{diff} ranging from 0 to 1 describes the diffusive fraction and f_{para} is the fraction of muon sites coupled to unpaired electron spins. Both the diffusion rate D_{2D} and the $f_{\text{diff}} f_{\text{para}}$ product are evaluated via (7.17) at each temperature. The 2D diffusion rate D_{2D} obtained from fits to the LF μ^+SR scans is shown in Figure 7.5A. On cooling through the transition into the C-CDW phase a dramatic rise is seen in D_{2D}, consistent with a QSL state supporting diffusing spinons. The diffusion rate increases on cooling through region QSLa until a maximum is reached at $T_0 \approx 110$ K. The region below T_0 is labelled QSLb and shows a relatively strong power law T^{n_D} with $n_D = 1.74(14)$. On cooling further another transition takes place below $T_1 \approx 25$ K where a weaker power law $n_D = 0.47(17)$ is found. This region is labelled QSLc.

While the diffusion rate depends only on the shape of $S_{\text{diff}}(\omega, 2)$, obtaining absolute values of the product $f_{\text{diff}} f_{\text{para}}$ requires knowledge of hyperfine coupling $\bar{A}$ of the muon to the electronic spins. We used a site-averaged value obtained from DFT calculations as $\bar{A} = 4.5(6)$ MHz (see Section 7.4). The temperature dependence of $f_{\text{diff}} f_{\text{para}}$ is shown in Figure 7.5B and shows a multi-region behaviour that matches

that of D_{2D}. The distinct T regions found in the diffusion properties are also seen in the ZF μ^+SR data in Figure 7.6.

7.4 Muon stopping sites

In order to better understand the sensitivity of the implanted muon to the diffusing spinons, muon stopping sites were calculated using DFT. The obtained final sites form four distinct groups (Figure 7.7). Muons in site 1 [Figure 7.7(a)] bond to one S atom in each layer, forming a linear S$-\mu^+-$S state with unequal μ^+-S bond lengths of 1.56 Å and 1.65 Å. Site 1 comprises two crystallographically distinct subclasses of sites that are made distinct by the CDW distortions. However, the local geometry of the muon is nearly identical in the two cases, resulting in similar hyperfine coupling. In site 2 [Figure 7.7(b)] the muon is bonded to only a single S atom (with a μ^+-S bond length of 1.4 Å), with these sites being around 0.03 eV higher in energy than site 1. In site 3 [Figure 7.7(c)], the muon stops inside the S layer, slightly displaced from the centre of the triangle defined by three S atoms, whereas for site 4 [Figure 7.7(d)] the muon sits around 0.7 Å above the centre of the triangle defined by three Ta atoms.

Hyperfine coupling tensors are calculated using the GIPAW method [258]. The dipolar coupling is much smaller than the contact hyperfine coupling for all sites. The hyperfine coupling is averaged over the members of each group to give a value

Table 7.1: Muon sites and their hyperfine couplings and zero-point energies. The fraction of muons stopping in each type of site is estimated from the number of random initial muon positions that resulted in the muon occupying this type of site after structural relaxation.

Site type	Energy (eV)	Fraction (%)	Average hyperfine coupling (MHz)	Zero-point energy (eV)
1 (interlayer)	0.03	34	6.25	0.35
2 (interlayer)	0.06	12	7.60	0.41
3 (S layer)	0.09	47	7.70	0.51
4 (Ta layer)	0.13	7	−0.92	0.65

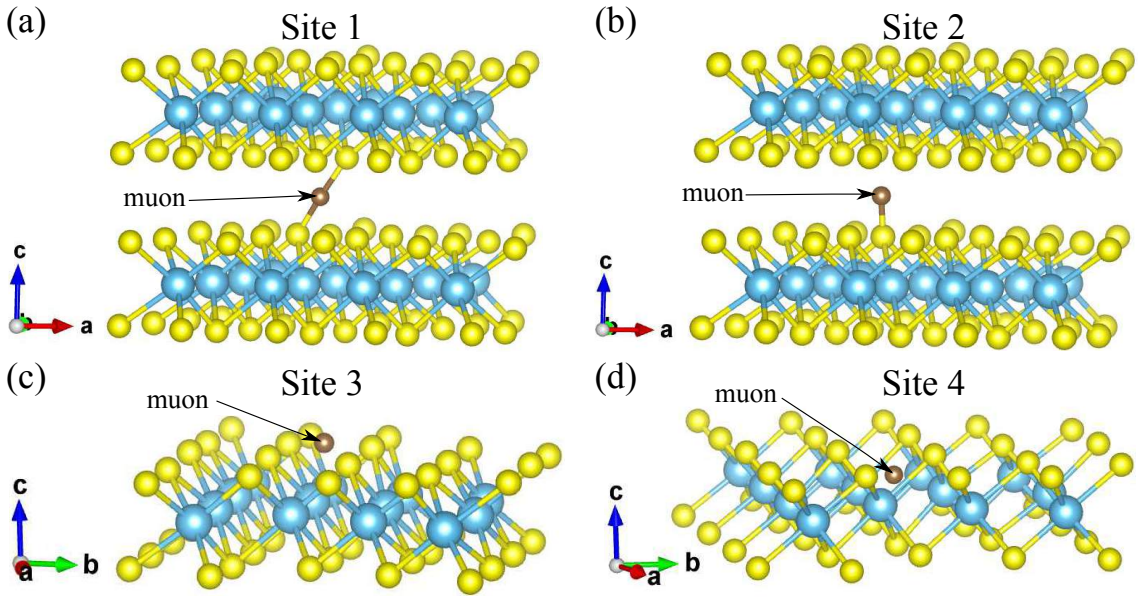

Figure 7.7: Muon stopping sites calculated using density functional theory. Ta and S are represented by blue and yellow spheres respectively. Sites 1 and 2 occupy the interlayer region. Site 3 is associated with the S layer and site 4 with the Ta layer.

for each site (Table 7.1). The calculated hyperfine coupling constants were found to be highly sensitive to the k-point grid used (varying by about 20%) and the $5\times5\times5$ grid used in our calculations is insufficient to ensure convergence of the hyperfine coupling. However, larger k-point grids are computationally prohibitive and this limits the accuracy of our estimate to around 1 MHz, so we can take $\bar{A} = 7(1)$ MHz for coupling to the adjacent layer. Table 7.1 also reports the zero-point energy (ZPE) of the muon at each site, determined from phonon calculations.

To investigate the possibility of muon diffusion within the temperature range of the experiment, I carried out transition state searches [253] between pairs of distinct muon stopping sites. Here, the lowest energy site within each cluster is chosen as the representative member of this cluster (Table 7.2). Energy barriers denoted as $i \to j$ correspond to those between adjacent sites of type i and j within the structure. For the cases where $i = j$, energy barriers were calculated between adjacent sites of the same type in the same layer. Energy barriers are illustrated in Figure 7.8(a). We find that the energy barrier between sites 1 and 2 is very close to the difference in energy between the two. This, coupled with the large ZPEs (0.35 eV and 0.51 eV respectively) of both sites means that the muon is likely to be delocalised between

Table 7.2: Energy barriers between muon stopping sites. Energy barriers denoted as $i \rightarrow j$ correspond to those between adjacent sites of type i and j within the structure.

	Energy barrier (eV)
$1 \rightarrow 1$	1.14
$1 \rightarrow 2$	0.03
$1 \rightarrow 3$	0.44
$1 \rightarrow 4$	1.29
$2 \rightarrow 2$	1.25
$2 \rightarrow 3$	0.39
$2 \rightarrow 4$	1.34
$3 \rightarrow 3$	1.49
$3 \rightarrow 4$	0.58
$4 \rightarrow 4$	2.01

these two geometries, rather than them representing two distinct stopping sites. Similarly, the barrier between sites 2 and 3 is less than their ZPE. Thus sites 1, 2 and 3 are expected to form a single quantum delocalised state. For site 4 the ZPE is larger than the barrier to site 3 and thus a transition to site 3 is expected. Barriers between adjacent sites of the same type within the layer are all > 1 eV and hence large compared with the ZPE and thermal energy available to the muon. Long range muon diffusion is therefore expected to be strongly suppressed in this structure and thus cannot be responsible for the rapid fall in D_{2D} and $f_{\mathrm{diff}} f_{\mathrm{para}}$ with temperature that is found in the QSLa phase.

The S$-\mu^{+}-$S bond formed by muons in site 1 is asymmetric, with the muons in this site closer to one layer than the other. This suggests that there may be an energy barrier for muons moving along the line joining the two S atoms. I therefore attempted to calculate the barrier between two muon sites located on either side of the centre of this line. The second site (denoted $1'$) was obtained by pushing the muon along the line joining the S atoms and allowing the resulting structure to relax. However, the LST algorithm failed to bracket the maximum from both endpoints, with all structures generated from the interpolation between the two

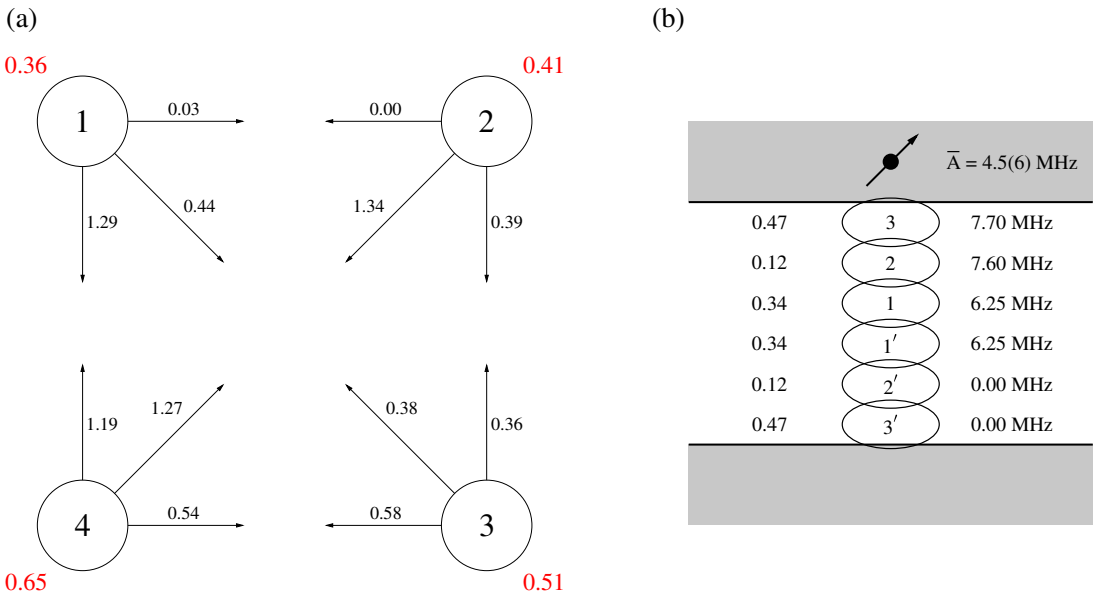

Figure 7.8: (a) Effective barrier heights in eV between the sites, taking the site energy differences into account. The corresponding ZPE of each site is shown in red. It can be seen that site 4 will be unstable against a transition to site 3 and that sites 1, 2 and 3 will combine to form a single quantum delocalised site. (b) A model of the quantum delocalised state for the muon, showing how it can be considered a superposition of the classical muon sites between two layers. The hyperfine coupling to an unpaired spin in the upper layer for each site is indicated and these are weighted by the fraction of muons in each site (left-hand column) to obtain $\bar{A} = 4.5(6)$ MHz.

muon sites being degenerate to within 0.005 eV. Thus, considering the large ZPE of the muon at these sites, we expect it to delocalise between sites 1 and 1′ and we therefore need to allow for the possibility of a further level of delocalisation across the interlayer region, linking the two sets of sites 1–3 above and below the midpoint between the layers. This would result in the muon wave function and hyperfine coupling being shared between the two layers. This is modelled in Figure 7.8(b), where it is assumed that muons in site 1 can couple to either layer, whereas muons in sites 2 or 3 couple only to the nearest layer. Taking the weighted average of the hyperfine coupling to one of the two layers for each type of site, where the weights are proportional to the number of initial positions that resulted in a site of this type, gives a best estimate $\bar{A} = 4.5(6)$ MHz for the hyperfine coupling between the muon and an unpaired spin in a single layer, which in turn determines the amplitude of

the diffusion term in the LF-dependent μ^+SR relaxation rate.

7.5 Discussion

Our LF μ^+SR measurements, combined with my calculations of the muon stopping sites, allowed us to extract the temperature dependence of the spinon diffusion rate D_{2D}. This enabled an interpretation of the data in terms of the predictions of QSL models (with this analysis carried out by Francis Pratt), which I report here. The many possible 2D QSL states for a triangular lattice can be broadly classified [231] as $SU(2)$, $U(1)$ or Z_2. Of these, the Z_2 states are expected to be most stable and there are also well-developed theories for the quantum critical properties of Z_2 QSL phases [259, 260, 261]. Thus Z_2 models provide a natural starting point for interpreting the present data. For a Z_2 QSL the spinon transport in the quantum critical (QC) regime [261] leads to $D_{2D} \propto T^{n_D}$ where $n_D = 2/\nu - 2$, with ν the critical exponent for the correlation length. To allow for an energy dependent DOS this can be extended to

$$n_D = 2/\nu - 2 + q, \tag{7.18}$$

where $q = 1$ for a linear Dirac DOS [Figure 7.2(a)] and $q = 0$ for a constant DOS, as would be expected for cases of quadratic dispersion or a large spinon Fermi surface [Figure 7.2(a)].

The ν exponent for bosonic spinons in a Z_2 QSL model for the triangular lattice is expected to be that of the $O(2N)$ criticality class [259, 260, 261], i.e.

$$\nu = 1 - \frac{16}{3\pi^2 N}, \tag{7.19}$$

where integer N is the dimension of the order parameter, which is 2 for the basic spin-only model. Collaborators at the Instituto de Ciencia Molecular, Universidad de Valencia (ICMol) carried out measurements of specific heat on 1T-TaS_2. The corresponding critical exponent for the specific heat, $C_p \propto T^{\alpha+q}$, can be obtained from (7.19) via the hyperscaling relation $\alpha = 2 - 3\nu$,

$$\alpha = \frac{16}{\pi^2 N} - 1. \tag{7.20}$$

Experimental values for α and ν are compared with the model values in Figure 7.9.

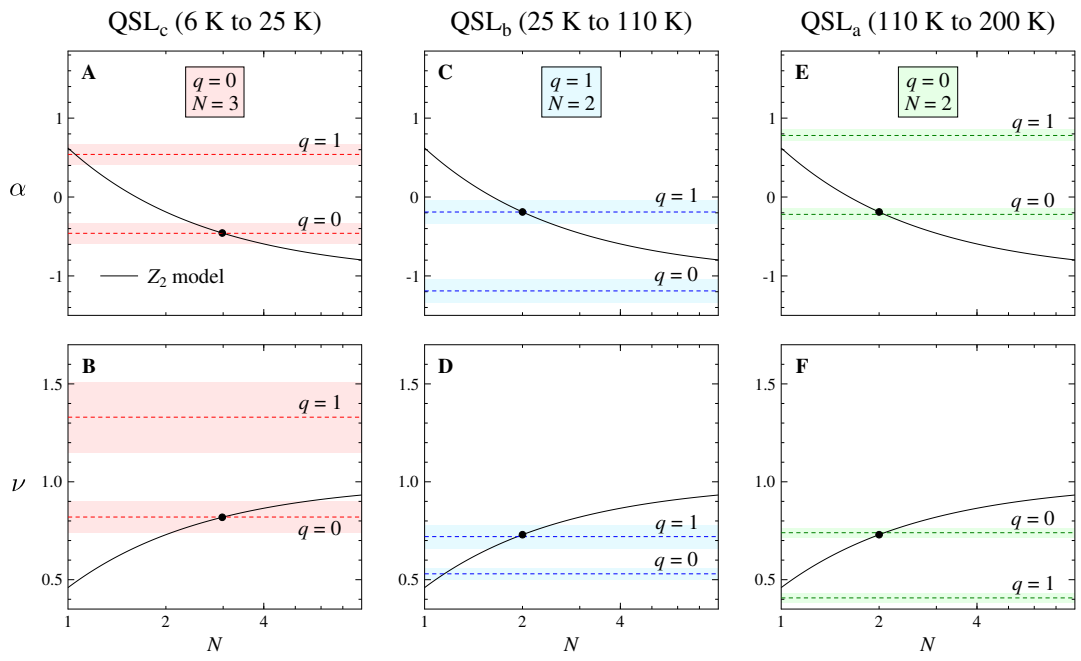

Figure 7.9: The exponent α from specific heat and the exponent ν from LF μ^+SR are compared with the Z_2 model values (solid lines). Dashed lines and shading indicate measured values and uncertainty, derived for $q = 0$ and $q = 1$. Solid points indicate the best model in each phase. For QSLc both measurements (A, B) require $q = 0$ and $N = 3$. For QSLb the data indicate $q = 1$ and $N = 2$ (C, D). For QSLa a return to $q = 0$ is found (E), keeping $N = 2$. Since LF μ^+SR in QSLa gives no realistic ν value, panel F shows $\nu = (2 - \alpha)/3$.

For QSLc the experimental values for α and ν are both consistent with $q = 0$ and $N = 3$ (Figure 7.9A,B). This suggests a Z_2-gapless QSL with an additional degree of freedom, possibly related to the effects of spin-orbit coupling. For QSLb, the ν exponent matches $q = 1$ and $N = 2$, indicating a Z_2-linear QSL (Figure 7.9D). The corresponding value for α is shown in Figure 7.9C. In QSLa it is found that $q = 0$ and $N = 2$ (Figure 7.9E) reflecting a Z_2-gapless QSL. The strong negative power for D_{2D} in QSLa (Figure 7.5A) is not predicted within this model, but may reflect inter-plane spin correlations sensed by the muon that will be discussed shortly. Another possibility for QSLa is a $U(1)$-gapless state with fermionic spinons, for which $n_D = -1/3$ is expected [262], but this is still much smaller than measured and the corresponding prediction $\alpha = 1/3$ [263] is not found (Figure 7.9E).

The survival of the QSL state in bulk 1T-TaS_2 is complicated by the interactions between layers and hence the possible CDW stacking configurations (hereafter referred to as the *electronic* stacking), as discussed in Section 7.1.2. A recent scanning tunneling microscopy (STM) study of the cleavage planes of 1T-TaS_2 at 77 K found large-gap surfaces assigned to band-insulator strongly-coupled spin-paired bilayers and narrow-gap surfaces assigned to unpaired Mott-gapped layers, that could support the QSL state [264]. The ratio of these two types of surface was found to be 3 to 1. The bilayers have A-mode stacking and the weaker stacking between the bilayers is C-mode (the center Ta site of the SD of the lower layer is located below the Ta sited in one of the tips of the SD of the upper layer). If the regular stacking sequence has the form ACACAC then cleavage is expected at the C planes, giving only A-mode bilayer surfaces [Figure 7.10(a)]. If the *electronic* stacking along the c axis is more complex, for example, of the form ACACCAC (or, in general, ACA$\perp\perp$AC, where $\perp$ is a layer with a stacking different than A), then a fraction of the cleavage planes will be unpaired monolayers and the experimental ratio of 3 to 1 is consistent with an average density of *electronic* stacking defects around this 1 in 7 level [Figure 7.10(b)]. For muons implanting in such a sequence, 2 out of 7 interlayer sites will see the unpaired layer and couple to the paramagnetic electronic relaxation and the remaining 5 sites will see the diamagnetic spin-paired bilayers, showing only nuclear relaxation. These site ratios are consistent with our muon measurements, which show a significant Kubo-Toyabe nuclear relaxation term that is assigned to the bilayers and a relatively weak Lorentzian relaxation term that is assigned to the QSL monolayers. Referring to Figure 7.5B and noting that f_{diff} can be no larger than 1, it can be seen that, whereas the data points at 40 K and below are compatible with $f_{\mathrm{para}} \approx 2/7$, higher temperatures around T_0 require a rather larger value of f_{para}, approaching 1 at T_0. This suggests a steady increase in the concentration of QSL layers with temperature. Example configurations with increased QSL layer concentration are shown in Figure 7.10(c) and Figure 7.10(d).

As discussed in Section 7.4, the rapid fall-off in the muon relaxation signal with increasing temperature above 110 K is not related to muon diffusion. The sensitivity of the muon probe state to spins in two adjacent layers was highlighted in Section 7.4

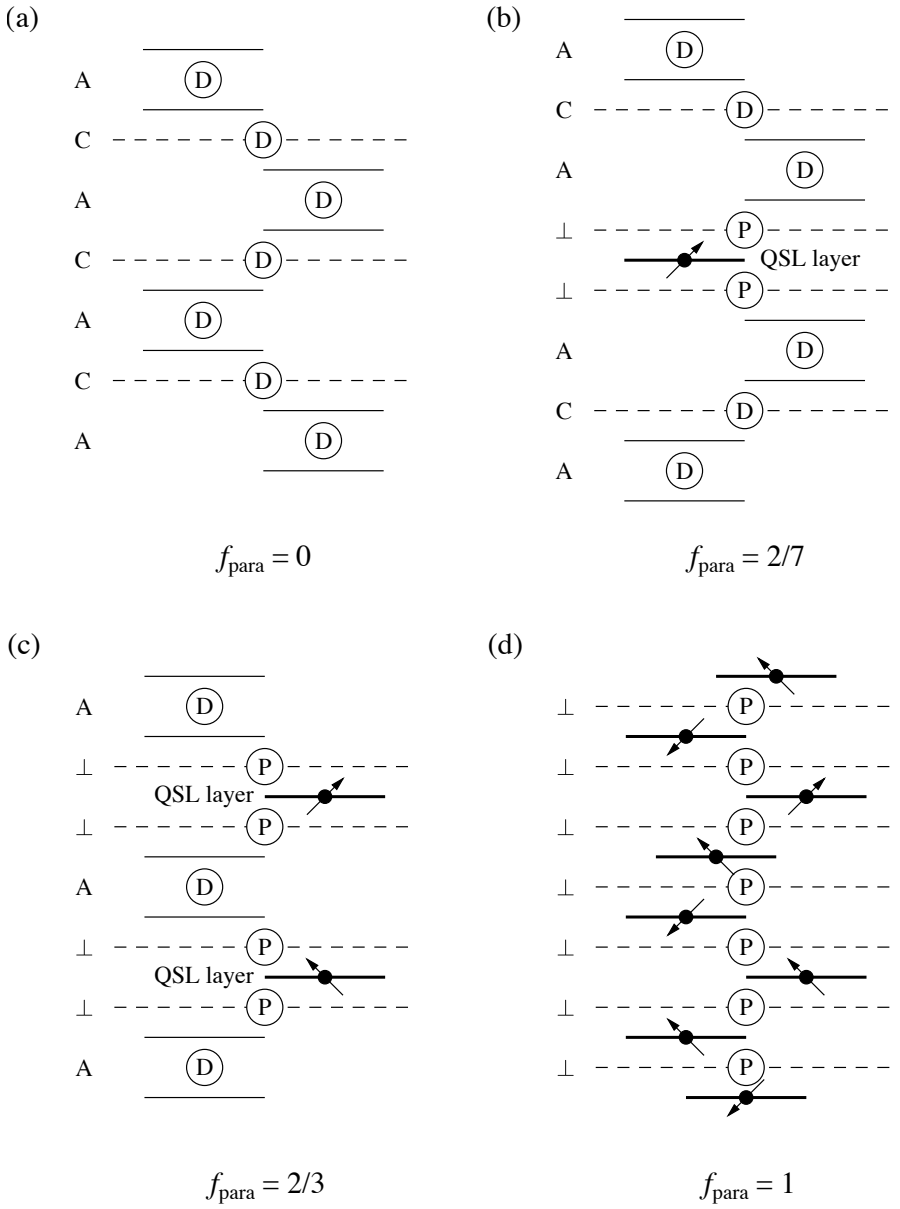

Figure 7.10: (a) Regular ACACAC stacking of the triangular-lattice layers of Star-of-David (SD) clusters produces completely spin-paired bilayers that do not support the QSL state. Cleavage at C planes (dashed lines) in such a structure results in bilayer surfaces. Muon sites in this case are all diamagnetic (shown as D). (b) A defect in the SD stacking sequence at the level of one in seven layers on average gives a sequence such as ACA⊥⊥AC for which 1 in 4 cleaved surfaces are unpaired monolayers that can support the QSL state. This ratio matches that seen in a recent STM study [264]. The muon stopping sites in this case split between diamagnetic (D) and paramagnetic (P), with f_{para}, the P to D site ratio, being 2/7 for this concentration of stacking defects. (c,d) Example sequences with greater concentrations of the electronic stacking defects that produce more unpaired QSL layers and larger values of f_{para}.

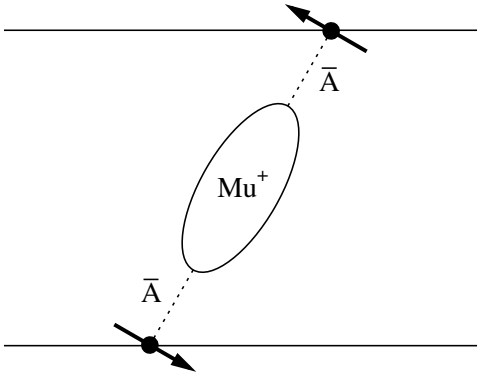

Figure 7.11: The extended muon probe state coupling to two unpaired electronic spins in two adjacent layers that show AF spin correlation. The hyperfine couplings of the two electronic spins to the muon will cancel out in this case.

and this characteristic is likely to be behind the reduced response in the higher temperature phase. In particular, if unpaired spins are present in two adjacent layers that show antiferromagnetic correlation, then the hyperfine couplings of the muon to the spins in the two layers will tend to cancel, leading to a loss of muon relaxation signal (Figure 7.11). This would imply that the bilayer spin coupling is breaking up in the QSLa phase as it approaches the 200 K transition to the incommensurate phase, as illustrated in Figure 7.10(d).

7.6 Conclusion

In conclusion, we have demonstrated that a consistent picture of the emergent QC exponents of a QSL can be obtained using the local-probe LF μ^+SR technique (with knowledge of the muon stopping site) alongside bulk specific heat measurements (carried out by coworkers). Establishing these exponents for a QSL allows a close engagement to be made with theory. For 1T-TaS_2 three distinct phases are suggested between 200 K and 6 K. A Z_2-gapless phase above 100 K, a Z_2-linear phase between 100 K and 25 K and another Z_2-gapless phase below 25 K. These results are in sharp contrast with the common assumption that a QSL maintains a single topological phase at all temperatures. Inter-QSL transitions like those suggested here represent

a novel class of non-symmetry-breaking thermal phase transition, which may be associated with finely-balanced temperature-dependent competing interactions and with marginally stable symmetric QSL states, where instabilities such as spinon pairing [265, 266] are likely to occur. The thermal transitions between distinct quantum phases observed in this study thus provide a new perspective on spin liquid behaviour.

The insight gained from the muon-probe is significantly enhanced by knowledge of its stopping site, obtained here from DFT calculations. These calculations also highlight the importance of the quantum nature of the muon. The large ZPE of the muon can increase the probability of it tunnelling between minima or, as seen here, can result in the formation of a quantum delocalised state. While the methods employed in this chapter may be best viewed as quantum mechanical corrections to results obtained using a "classical" muon, they represent a first step towards a fully quantum mechanical treatment of the muon.

Chapter 8

Conclusion and further work

The results presented in this thesis demonstrate that the interpretation of μ^+SR experiments can be significantly enhanced by the knowledge of the muon stopping site, which can be calculated using DFT. In Chapter 5, DFT calculations reassure us that the muon acts as a faithful probe of the magnetic properties of the 'nonmetallic metal' FeCrAs, as the muon does not introduce any significant structural distortions into the system. The muon is able to detect the onset of long-range magnetic order, and is also sensitive to fluctuating magnetism and the freezing of dynamics above and below this transition, respectively. This is to be contrasted with the case of the molecular spin ladder compound $(Hpip)_2CuBr_4$, discussed in Chapter 6, where it was found that the muon induces significant structural and electronic distortions to its host. It was proposed that the the muon, when taken together with the local distortion it produces, leads to a local probe unit with good sensitivity to the magnetic state. This results in transverse-field μ^+SR spectra displaying characteristic behaviour in each of the regions of the phase diagram. In the μ^+SR study of the charge density wave system 1T-TaS_2, presented in Chapter 7, the muon provides sensitivity to the diffusing spinons, with the temperature dependence of the diffusion rate demonstrating three distinct phases. DFT identified a quantum delocalised state of the muon between TaS_2 layers, which allowed us to construct models that help to explain the differing muon response in each of these phases.

In the context of DFT+μ as a whole, there are a number of conclusions that can be drawn from the examples presented in this thesis. Of these examples, Fe-

CrAs is one of the more straightforward cases, as it appears as though the muon is well-behaved in this system and does not introduce any pecularities to the observed spectra. Still, knowledge of this fact is reassuring for the results obtained from the μ^+SR study, particularly as the local magnetic field observed in these measurements is similar to the dipolar field calculated from the previously-proposed magnetic structure. These calculations also demonstrate that the minimum of the electrostatic potential can provide a good first estimate of the muon stopping site in specific cases, as found previously [93, 94, 95]. This is also the case in the heavy-fermion systems URu_2Si_2 and $CeRu_2Si_2$ (discussed in Chapter 4) where the muon stopping sites calculated using structural relaxations were found to be close to, but not identical to, the minima of the electrostatic potential. In these examples it was possible to compare properties associated with these sites with the results of μ^+SR experiments. In the case of URu_2Si_2, the dipolar field at the proposed site is found to lie almost entirely along the c axis, in agreement with the findings of a recent μ^+SR study [134]. For $CeRu_2Si_2$, closer comparison can be made, as a stopping site was previously proposed on the basis of muon Knight shift measurements [84]. While the two sites differ in this case, similar comparisons of sites for the other heavy-fermion compounds included in the same study [84] would provide a useful assessment of the agreement between the two approaches.

A useful finding of the calculations on URu_2Si_2 and $CeRu_2Si_2$ is that the muon stopping sites in these isostructual compounds are nearly identical. This suggests that it should be possible to propose muon stopping sites in a material on the basis of sites calculated for an isostructural compound. This is supported by the results of calculations on the skyrmion-hosting compounds GaV_4S_8 and GaV_4Se_8, in which the same four distinct sites are found in both compounds. A complication here is that the chemical subsitution of S for Se changes the energetic ordering of these sites, which may affect which site is realised in practice (though it is not yet known how to translate the relative energies of multiple stopping sites into occupation probabilities). The sites calculated for GaV_4S_8 have since been used by my colleague Thomas Hicken [267] to simulate the expected field distribution seen by the muon in the skyrmion phase, with the preliminary results showing good agreement with the

measured spectra. This is similar to what was done previously for Cu_2OSeO_3 [268], where the calculated field distributions for the skyrmion phase and the surrounding helical phases were compared to the spectral intensities in TF μ^+SR spectra. We aim to be able to analyse μ^+SR spectra in terms of field distributions arising from spin textures, instead of relying solely on idealised model field distributions (such as those discussed in Chapter 2).

I have also introduced new tools for carrying out muon site calculations (see Chapter 4). These take the form of the MuFinder program, which aims to make it easier for non-experts to carry out calculations similar to those presented in this thesis. The site generation algorithm used by MuFinder aims to reduce the computational cost of these calculations by limiting the number of initial positions required in order to sufficiently sample the potential energy landscape for the muon. Despite this, each geometry optimisation calculation can be quite time-consuming and represents the rate-determining step in obtaining muon sites. Work has been done exploring alternative methods of carrying out these calculations, such as replacing DFT with the much faster lower-level approximation of Density Functional Tight Binding (DFTB) [109]. However, the limited number of elements available in a given basis set prevents this from being a general solution. It is clear that a fine balance between accuracy and computational cost will need to be struck in order for these techniques to become a routine part of carrying out μ^+SR experiments.

For the muon sites in 1T-TaS_2 (Chapter 7), evaluation of the muon's zero-point energy (ZPE) and the energy barriers between sites suggests the formation of a quantum delocalised state for the muon. The quantum nature of the muon is likely to be important in a number of cases, given that its mass is only one-ninth of the proton mass. Investigations into the use of path integral molecular dynamics (PIMD) [269] to enable a fully quantum mechanical treatment of the muon are ongoing, with calculations involving muonium of various charge states in solid nitrogen, carried out by my colleague Matjaž Gomilšek, showing promising results [270]. A fully quantum mechanical treatment of the muon is likely to be computationally prohibitive for many systems. In these cases, attempts should be made to estimate the ZPE associated with the muon at each site using a less expensive method, such

as phonon calculations (as was done for 1T-TaS_2 in Chapter 7). The muon's ZPE is an important factor to consider when comparing the energetics of multiple local minima, as it is possible that not all of these minima will be stable once the ZPE is taken into account.

The distortions induced by the muon to its local environment are also an important factor to consider. In most examples in this thesis, these distortions are found to be insignificant, with the one notable exception being for the muon sites in the molecular spin ladder $(Hpip)_2CuBr_4$ (Chapter 6). In contrast to the distortions induced in pyrochlore oxides [91], which serve to mask the true magnetic behaviour of the sample under study, my analysis suggests that the distortions in $(Hpip)_2CuBr_4$ are responsible for the sensivity of the muon to the magnetic phases in this system. However, muon-induced distortions are unlikely to be as benevolent as this in general and are particularly important to understand in systems on the verge of an instability, or where doping is a critical parameter. An interesting case to consider is that of non-centrosymmetric superconductors, where μ^+SR measurements have indicated the presence of time-reversal symmetry (TRS) breaking [271, 272, 273]. These measurements reveal the spontaneous appearance of a magnetic field below the transition temperature and, while there is also evidence for TRS breaking in Sr_2RuO_4 from the polar Kerr effect [274], this has only been observed using muons in the vast majority of cases. These spontaneous fields are thought to be generated by supercurrents associated with variation of the superconducting order parameter near dilute imperfections in the material [275], with the locality of the probe making μ^+SR ideal for their detection. However, we might ask if the muon instead introduces signficant structural or electronic distortions that modify the local physics of the system we are trying to measure. With the recent advances in the calculation of muon stopping sites using DFT, including those made through the studies presented in this thesis, we are now in a much stronger position to answer this question.

Bibliography

[1] S. J. Blundell, Contemp. Phys. **40**, 175 (1999).

[2] J. S. Möller, P. Bonfà, D. Ceresoli, F. Bernardini, S. J. Blundell, T. Lancaster, R. D. Renzi, N. Marzari, I. Watanabe, S. Sulaiman, and M. I. Mohamed-Ibrahim, Phys. Scr. **88**, 68510 (2013).

[3] C. D. Anderson and S. H. Neddermeyer, Phys. Rev. **50**, 263 (1936).

[4] S. H. Neddermeyer and C. D. Anderson, Phys. Rev. **51**, 884 (1937).

[5] H. Yukawa, Proc. Phys. Math. Soc. Jpn. **17**, 48 (1935).

[6] R. L. Garwin, L. M. Lederman, and M. Weinrich, Phys. Rev. **105**, 1415 (1957).

[7] A. Hillier, D. Paul, and K. Ishida, Microchem. J. **125**, 203 (2016).

[8] A. Yaouanc and P. D. de Réotier, *Muon Spin Rotation, Relaxation and Resonance* (OUP, 2010).

[9] M. Heming, E. Roduner, B. D. Patterson, W. Odermatt, J. Schneider, H. Baumeler, H. Keller, and I. M. Savi, Chem. Phys. Lett. **128**, 100 (1986).

[10] R. F. Kiefl, S. Kreitzman, M. Celio, R. Keitel, G. M. Luke, J. H. Brewer, D. R. Noakes, P. W. Percival, T. Matsuzaki, and K. Nishiyama, Phys. Rev. A **34**, 681 (1986).

[11] J. E. Sonier, J. H. Brewer, and R. F. Kiefl, Rev. Mod. Phys. **72**, 769 (2000).

[12] S. F. J. Cox, R. L. Lichti, J. S. Lord, E. A. Davis, R. C. Vilão, J. M. Gil, T. D. Veal, and Y. G. Celebi, Phys. Scr. **88**, 68503 (2013).

[13] S. J. Blundell, *Magnetism in Condensed Matter*, 1st ed. (Oxford University Press, Oxford, UK, 2000).

[14] B. I. Bleaney and B. Bleaney, *Electricity and Magnetism* (Oxford University Press, Oxford, UK, 1989).

[15] T. D. Lee and C. N. Yang, Phys. Rev. **104**, 254 (1956).

[16] C. S. Wu, E. Ambler, R. W. Hayward, D. D. Hoppes, and R. P. Hudson, Phys. Rev. **105**, 1413 (1957).

[17] S. L. Lee, S. H. Kilcoyne, and R. Cywinski, eds., *Muon Science: Muons in Physics, Chemistry and Materials* (1999).

[18] A. E. Pifer, T. Bowen, and K. R. Kendall, Nucl. Instrum. Methods **135**, 39 (1976).

[19] T. D. Lee and C. N. Yang, Phys. Rev. **105**, 1671 (1957).

[20] B. D. Patterson, Rev. Mod. Phys. **60**, 69 (1988).

[21] D. Brice, Phys. Lett. A **66**, 53 (1978).

[22] J. S. Lord, I. McKenzie, P. J. Baker, S. J. Blundell, S. P. Cottrell, S. R. Giblin, J. Good, A. D. Hillier, B. H. Holsman, P. J. C. King, T. Lancaster, R. Mitchell, J. B. Nightingale, M. Owczarkowski, S. Poli, F. L. Pratt, N. J. Rhodes, R. Scheuermann, and Z. Salman, Rev. Sci. Instrum. **82**, 73904 (2011).

[23] P. Dalmas de Réotier and A. Yaouanc, J. Phys.: Condens. Matter **9**, 9113 (1997).

[24] M. A. Ruderman and C. Kittel, Phys. Rev. **96**, 99 (1954).

[25] T. Kasuya, Prog. Theor. Phys. **16**, 45 (1956).

[26] K. Yosida, Phys. Rev. **106**, 893 (1957).

[27] R. Kubo and T. Toyabe, in *Magnetic Resonance and Relaxation*, edited by R. Blinc (North-Holland, Amsterdam, 1967) pp. 810–823.

[28] R. S. Hayano, Y. J. Uemura, J. Imazato, N. Nishida, T. Yamazaki, and R. Kubo, Phys. Rev. B **20**, 850 (1979).

[29] K. W. Kehr, G. Honig, and D. Richter, Z. Phys. B **32**, 49 (1978).

[30] J. Lord, S. Cottrell, and W. Williams, Physica B **289290**, 495 (2000).

[31] M. Celio and P. F. Meier, Hyperfine Interact. **18**, 435 (1984).

[32] J. H. Brewer, S. R. Kreitzman, D. R. Noakes, E. J. Ansaldo, D. R. Harshman, and R. Keitel, Phys. Rev. B **33**, 7813 (1986).

[33] W. Hayes and A. M. Stoneham, *Defects and defect processes in nonmetallic solids* (Dover Publications, New York, NY, 2004).

[34] E. Roduner and H. Fischer, Chem. Phys. **54**, 261 (1981).

[35] T. Lancaster, S. J. Blundell, P. J. Baker, M. L. Brooks, W. Hayes, F. L. Pratt, J. L. Manson, M. M. Conner, and J. A. Schlueter, Phys. Rev. Lett. **99**, 267601 (2007).

[36] J. S. Möller, D. Ceresoli, T. Lancaster, N. Marzari, and S. J. Blundell, Phys. Rev. B **87**, 121108 (2013).

[37] F. Bernardini, P. Bonfà, S. Massidda, and R. De Renzi, Phys. Rev. B **87**, 115148 (2013).

[38] B. M. Huddart, J. Brambleby, T. Lancaster, P. A. Goddard, F. Xiao, S. J. Blundell, F. L. Pratt, J. Singleton, P. Macchi, R. Scatena, A. M. Barton, and J. L. Manson, Phys. Chem. Chem. Phys. **21**, 1014 (2019).

[39] F. Pratt, Physica B **289-290**, 710 (2000).

[40] J. L. Manson, J. A. Schlueter, K. A. Funk, H. I. Southerland, B. Twamley, T. Lancaster, S. J. Blundell, P. J. Baker, F. L. Pratt, J. Singleton, R. D. McDonald, P. A. Goddard, P. Sengupta, C. D. Batista, L. Ding, C. Lee, M.-H. Whangbo, I. Franke, S. Cox, C. Baines, and D. Trial, J. Am. Chem. Soc. **131**, 6733 (2009).

[41] P. A. Goddard, J. Singleton, P. Sengupta, R. D. McDonald, T. Lancaster, S. J. Blundell, F. L. Pratt, S. Cox, N. Harrison, J. L. Manson, H. I. Southerland, and J. A. Schlueter, New J. Phys. **10**, 83025 (2008).

[42] P. A. Goddard, J. Singleton, I. Franke, J. S. Möller, T. Lancaster, A. J. Steele, C. V. Topping, S. J. Blundell, F. L. Pratt, C. Baines, J. Bendix, R. D. McDonald, J. Brambleby, M. R. Lees, S. H. Lapidus, P. W. Stephens, B. W. Twamley, M. M. Conner, K. Funk, J. F. Corbey, H. E. Tran, J. A. Schlueter, and J. L. Manson, Phys. Rev. B **93**, 94430 (2016).

[43] G. Müller, H. Thomas, H. Beck, and J. C. Bonner, Phys. Rev. B **24**, 1429 (1981).

[44] E. Manousakis, Rev. Mod. Phys. **63**, 1 (1991).

[45] T. Giamarchi, *Quantum physics in one dimension* (OUP, 2003).

[46] N. D. Mermin and H. Wagner, Phys. Rev. Lett. **17**, 1133 (1966).

[47] H. J. Schulz, Phys. Rev. Lett. **77**, 2790 (1996).

[48] P. Sengupta, A. W. Sandvik, and R. R. P. Singh, Phys. Rev. B **68**, 94423 (2003).

[49] S. J. Blundell, T. Lancaster, F. L. Pratt, P. J. Baker, M. L. Brooks, C. Baines, J. L. Manson, and C. P. Landee, J. Phys. Chem. Solids **68**, 2039 (2007).

[50] T. Lancaster, S. J. Blundell, and F. L. Pratt, Phys. Scr. **88**, 68506 (2013).

[51] T. Lancaster, B. M. Huddart, R. C. Williams, F. Xiao, K. J. A. Franke, P. J. Baker, F. L. Pratt, S. J. Blundell, J. A. Schlueter, M. B. Mills, A. C. Maahs, and K. E. Preuss, J. Phys.: Condens. Matter **31**, 394002 (2019).

[52] P. R. Hammar, M. B. Stone, D. H. Reich, C. Broholm, P. J. Gibson, M. M. Turnbull, C. P. Landee, and M. Oshikawa, Phys. Rev. B **59**, 1008 (1999).

[53] T. Lancaster, S. J. Blundell, M. L. Brooks, P. J. Baker, F. L. Pratt, J. L. Manson, C. P. Landee, and C. Baines, Phys. Rev. B **73**, 20410 (2006).

[54] T. Otieno, A. M. Gipson, and S. Parkin, J. Chem. Crystallogr. **32**, 81 (2002).

[55] C. Yasuda, S. Todo, K. Hukushima, F. Alet, M. Keller, M. Troyer, and H. Takayama, Phys. Rev. Lett. **94**, 217201 (2005).

[56] M. Born and R. Oppenheimer, Annalen der Physik **389**, 457 (1927).

[57] E. A. Hylleraas, Z. Physik **54**, 347 (1929).

[58] H. M. James and A. S. Coolidge, J. Chem. Phys. **1**, 825 (1933).

[59] W. Kohn, Rev. Mod. Phys. **71**, 1253 (1999).

[60] L. H. Thomas, Proc. Cambridge Philos. Soc. **23**, 542548 (1927).

[61] E. Fermi, Atti Accad. Naz. Lincei, Cl. Sci. Fis. Mat. Nat. Rend. **6**, 602 (1927).

[62] P. Hohenberg and W. Kohn, Phys. Rev. **136**, B864 (1964).

[63] W. Kohn, in *Proceedings of the International School of Physics,* "Enrico Fermi," Course LXXXIX (1985) p. 4.

[64] W. Kohn and L. J. Sham, Phys. Rev. **140**, A1133 (1965).

[65] U. von Barth and L. Hedin, J Phys. C **5**, 1629 (1972).

[66] D. M. Ceperley and B. J. Alder, Phys. Rev. Lett. **45**, 566 (1980).

[67] J. P. Perdew, K. Burke, and M. Ernzerhof, Phys. Rev. Lett. **77**, 3865 (1996).

[68] S. J. Clark, M. D. Segall, C. J. Pickard, P. J. Hasnip, M. J. Probert, K. Refson, and M. Payne, Z. Kristallogr. **220**, 567 (2005).

[69] H. J. Monkhorst and J. D. Pack, Phys. Rev. B **13**, 5188 (1976).

[70] R. M. Martin, *Electronic Structure: Basic Theory and Practical Methods* (Cambridge University Press, 2004).

[71] M. C. Payne, M. P. Teter, D. C. Allan, T. Arias, and J. D. Joannopoulos, Rev. Mod. Phys. **64**, 1045 (1992).

[72] J. C. Phillips, Phys. Rev. **112**, 685 (1958).

[73] J. C. Phillips and L. Kleinman, Phys. Rev. **116**, 287 (1959).

[74] V. Heine, Solid State Phys. **24**, 1 (1970).

[75] D. R. Hamann, M. Schlüter, and C. Chiang, Phys. Rev. Lett. **43**, 1494 (1979).

[76] D. Vanderbilt, Phys. Rev. B **41**, 7892 (1990).

[77] R. P. Feynman, Phys. Rev. **56**, 340 (1939).

[78] S. Baroni, S. de Gironcoli, A. Dal Corso, and P. Giannozzi, Rev. Mod. Phys. **73**, 515 (2001).

[79] X. Gonze, Phys. Rev. B **55**, 10337 (1997).

[80] O. H. Nielsen and R. M. Martin, Phys. Rev. B **32**, 3780 (1985).

[81] B. G. Pfrommer, M. Cote, S. G. Louie, and M. L. Cohen, J. Comput. Phys. **131**, 233 (1997).

[82] C. K. Gan, P. D. Haynes, and M. C. Payne, Comput. Phys. Commun. **134**, 33 (2001).

[83] R. De Renzi, G. Guidi, P. Podini, R. Tedeschi, C. Bucci, and S. F. J. Cox, Phys. Rev. B **30**, 186 (1984).

[84] A. Amato, R. Feyerherm, F. Gygax, and A. Schenck, Hyperfine Interact. **104**, 115 (1997).

[85] R. F. Kiefl, M. Celio, T. L. Estle, S. R. Kreitzman, G. M. Luke, T. M. Riseman, and E. J. Ansaldo, Phys. Rev. Lett. **60**, 224 (1988).

[86] J. H. Brewer, R. F. Kiefl, J. F. Carolan, P. Dosanjh, W. N. Hardy, S. R. Kreitzman, Q. Li, T. M. Riseman, P. Schleger, H. Zhou, E. J. Ansaldo, D. R. Noakes, L. P. Le, G. M. Luke, Y. J. Uemura, K. Hepburn-Wiley, and C. E. Stronach, Hyperfine Interact. **63**, 177 (1991).

[87] A. J. Fisher, Curr. Opin. Solid. St. M. **1**, 841 (1996).

[88] R. M. Valladares, M. I. J. Probert, and A. J. Fisher, Mater. Sci. Eng. B **37**, 247 (1996).

[89] M. I. J. Probert and A. J. Fisher, J. Phys.: Condens. Matter **9**, 3241 (1997).

[90] S. J. Blundell, J. S. Möller, T. Lancaster, P. J. Baker, F. L. Pratt, G. Seber, and P. M. Lahti, Phys. Rev. B **88**, 64423 (2013).

[91] F. R. Foronda, F. Lang, J. S. Möller, T. Lancaster, A. T. Boothroyd, F. L. Pratt, S. R. Giblin, D. Prabhakaran, and S. J. Blundell, Phys. Rev. Lett. **114**, 17602 (2015).

[92] F. Xiao, J. S. Möller, T. Lancaster, R. C. Williams, F. L. Pratt, S. J. Blundell, D. Ceresoli, A. M. Barton, and J. L. Manson, Phys. Rev. B **91**, 144417 (2015).

[93] H. Maeter, H. Luetkens, Y. G. Pashkevich, A. Kwadrin, R. Khasanov, A. Amato, A. A. Gusev, K. V. Lamonova, D. A. Chervinskii, R. Klingeler, C. Hess, G. Behr, B. Büchner, and H.-H. Klauss, Phys. Rev. B **80**, 94524 (2009).

[94] R. D. Renzi, P. Bonfà, M. Mazzani, S. Sanna, G. Prando, P. Carretta, R. Khasanov, A. Amato, H. Luetkens, M. Bendele, F. Bernardini, S. Massidda, A. Palenzona, M. Tropeano, and M. Vignolo, Supercond. Sci. Technol. **25**, 84009 (2012).

[95] G. Lamura, T. Shiroka, P. Bonfà, S. Sanna, F. Bernardini, R. D. Renzi, R. Viennois, E. Giannini, A. Piriou, N. Emery, M. R. Cimberle, and M. Putti, J. Phys.: Condens. Matter **25**, 156004 (2013).

[96] P. Dalmas de Réotier, A. Maisuradze, A. Yaouanc, B. Roessli, A. Amato, D. Andreica, and G. Lapertot, Phys. Rev. B **93**, 144419 (2016).

[97] P. Dalmas de Réotier, A. Maisuradze, A. Yaouanc, B. Roessli, A. Amato, D. Andreica, and G. Lapertot, Phys. Rev. B **95**, 180403 (2017).

[98] A. Amato, P. Dalmas de Réotier, D. Andreica, A. Yaouanc, A. Suter, G. Lapertot, I. M. Pop, E. Morenzoni, P. Bonfà, F. Bernardini, and R. De Renzi, Phys. Rev. B **89**, 184425 (2014).

[99] F. Lang, P. J. Baker, A. A. Haghighirad, Y. Li, D. Prabhakaran, R. Valentí, and S. J. Blundell, Phys. Rev. B **94**, 20407 (2016).

[100] F. K. K. Kirschner, R. D. Johnson, F. Lang, D. D. Khalyavin, P. Manuel, T. Lancaster, D. Prabhakaran, and S. J. Blundell, Phys. Rev. B **99**, 64403 (2019).

[101] F. Lang, L. Jowitt, D. Prabhakaran, R. D. Johnson, and S. J. Blundell, Phys. Rev. B **100**, 94401 (2019).

[102] G. Prando, P. Bonfà, G. Profeta, R. Khasanov, F. Bernardini, M. Mazzani, E. M. Brüning, A. Pal, V. P. S. Awana, H.-J. Grafe, B. Büchner, R. De Renzi, P. Carretta, and S. Sanna, Phys. Rev. B **87**, 64401 (2013).

[103] P. Bonfà, F. Sartori, and R. De Renzi, J. Phys. Chem. C **119**, 4278 (2015).

[104] I. J. Onuorah, P. Bonfà, R. De Renzi, L. Monacelli, F. Mauri, M. Calandra, and I. Errea, Phys. Rev. Materials **3**, 73804 (2019).

[105] C. J. Pickard and R. J. Needs, J. Phys.: Condens. Matter **23**, 53201 (2011).

[106] L. Liborio, S. Sturniolo, and D. Jochym, J. Chem. Phys. **148**, 134114 (2018).

[107] O. K. Andersen and O. Jepsen, Phys. Rev. Lett. **53**, 2571 (1984).

[108] G. Seifert, J. Phys. Chem. A **111**, 5609 (2007).

[109] S. Sturniolo, L. Liborio, and S. Jackson, J. Chem. Phys. **150**, 154301 (2019).

[110] A. H. Larsen, J. J. Mortensen, J. Blomqvist, I. E. Castelli, R. Christensen, M. Dułak, J. Friis, M. N. Groves, B. Hammer, C. Hargus, E. D. Hermes, P. C. Jennings, P. B. Jensen, J. Kermode, J. R. Kitchin, E. L. Kolsbjerg, J. Kubal, K. Kaasbjerg, S. Lysgaard, J. B. Maronsson, T. Maxson, T. Olsen, L. Pastewka, A. Peterson, C. Rostgaard, J. Schiøtz, O. Schtt, M. Strange, K. S. Thygesen, T. Vegge, L. Vilhelmsen, M. Walter, Z. Zeng, and K. W. Jacobsen, J, Phys.: Condens. Matter **29**, 273002 (2017).

[111] S. Sturniolo, "Soprano - a library to crack crystals," URL https://ccp-nc.github.io/soprano/.

[112] P. Bonfà, I. J. Onuorah, and R. D. Renzi, JPS Conf. Proc. **21**, 11052 (2018).

[113] J. Hopcroft and R. Tarjan, Commun. ACM **16**, 372 (1973).

[114] A. A. Hagberg, D. A. Schult, and P. J. Swart, in *Proceedings of the 7th Python in Science Conference*, edited by G. Varoquaux, T. Vaught, and J. Millman (Pasadena, CA USA, 2008) pp. 11–15.

[115] Wills, A., J. Phys. IV France **11**, Pr9 (2001).

[116] K. J. A. Franke, B. M. Huddart, T. J. Hicken, F. Xiao, S. J. Blundell, F. L. Pratt, M. Crisanti, J. A. T. Barker, S. J. Clark, A. Štefančič, M. C. Hatnean, G. Balakrishnan, and T. Lancaster, Phys. Rev. B **98**, 54428 (2018).

[117] I. Dzyaloshinskii, J. Phys. Chem. Solids **4**, 241 (1958).

[118] T. Moriya, Phys. Rev. **120**, 91 (1960).

[119] A. N. Bogdanov and D. A. Yablonskii, Sov. Phys. JETP **68**, 101 (1989).

[120] T. Kurumaji, T. Nakajima, V. Ukleev, A. Feoktystov, T.-h. Arima, K. Kakurai, and Y. Tokura, Phys. Rev. Lett. **119**, 237201 (2017).

[121] I. Kézsmárki, S. Bordács, P. Milde, E. Neuber, L. M. Eng, J. S. White, H. M. Rønnow, C. D. Dewhurst, M. Mochizuki, K. Yanai, H. Nakamura, D. Ehlers, V. Tsurkan, and A. Loidl, Nat. Mater. **14**, 1116 (2015).

[122] J. S. White, A. Butykai, R. Cubitt, D. Honecker, C. D. Dewhurst, L. F. Kiss, V. Tsurkan, and S. Bordács, Phys. Rev. B **97**, 20401 (2018).

[123] S. Bordács, A. Butykai, B. G. Szigeti, J. S. White, R. Cubitt, A. O. Leonov, S. Widmann, D. Ehlers, H.-A. Krug von Nidda, V. Tsurkan, A. Loidl, and I. Kézsmárki, Sci. Rep. **7**, 7584 (2017).

[124] R. Pocha, D. Johrendt, and R. Pöttgen, Chem. Mater. **12**, 2882 (2000).

[125] A. Butykai, S. Bordács, I. Kézsmárki, V. Tsurkan, A. Loidl, J. Döring, E. Neuber, P. Milde, S. C. Kehr, and L. M. Eng, Sci. Rep. **7**, 44663 (2017).

[126] H. Nakamura, R. Ikeno, G. Motoyama, T. Kohara, Y. Kajinami, and Y. Tabata, J. Phys.: Conf. Ser. **145**, 12077 (2009).

[127] Y. Fujima, N. Abe, Y. Tokunaga, and T. Arima, Phys. Rev. B **95**, 180410 (2017).

[128] D. Ehlers, I. Stasinopoulos, V. Tsurkan, H.-A. Krug von Nidda, T. Fehér, A. Leonov, I. Kézsmárki, D. Grundler, and A. Loidl, Phys. Rev. B **94**, 14406 (2016).

[129] D. Bichler, Magnetismus und strukturelle Phasenumwandlungen von Verbindungen mit tetraedrischen Metallclustern, Ph.D. thesis, Ludwig-Maximilians-Universitat Munchen, 2010.

[130] J. T. Zhang, J. L. Wang, X. Q. Yang, W. S. Xia, X. M. Lu, and J. S. Zhu, Phys. Rev. B **95**, 85136 (2017).

[131] A. Amato, M. J. Graf, A. de Visser, H. Amitsuka, D. Andreica, and A. Schenck, J. Phys.: Condens. Matter **16**, S4403 (2004).

[132] D. E. MacLaughlin, D. W. Cooke, R. H. Heffner, R. L. Hutson, M. W. McElfresh, M. E. Schillaci, H. D. Rempp, J. L. Smith, J. O. Willis, E. Zirngiebl, C. Boekema, R. L. Lichti, and J. Oostens, Phys. Rev. B **37**, 3153 (1988).

[133] G. M. Luke, A. Keren, L. P. Le, Y. J. Uemura, W. D. Wu, D. Bonn, L. Taillefer, J. D. Garrett, and Y. Ōnuki, Hyperfine Interact. **85**, 397 (1994).

[134] M. N. Wilson, T. J. Williams, Y.-P. Cai, A. M. Hallas, T. Medina, T. J. Munsie, S. C. Cheung, B. A. Frandsen, L. Liu, Y. J. Uemura, and G. M. Luke, Phys. Rev. B **93**, 64402 (2016).

[135] A. Amato, Rev. Mod. Phys. **69**, 1119 (1997).

[136] A. Amato, R. Feyerherm, F. N. Gygax, A. Schenck, J. Flouquet, and P. Lejay, Phys. Rev. B **50**, 619 (1994).

[137] A. Amato, C. Baines, R. Feyerherm, J. Flouquet, F. Gygax, P. Lejay, A. Schenck, and U. Zimmermann, Physica B **186-188**, 276 (1993).

[138] J. A. Mydosh and P. M. Oppeneer, Rev. Mod. Phys. **83**, 1301 (2011).

[139] T. T. M. Palstra, A. A. Menovsky, J. v. d. Berg, A. J. Dirkmaat, P. H. Kes, G. J. Nieuwenhuys, and J. A. Mydosh, Phys. Rev. Lett. **55**, 2727 (1985).

[140] T. T. M. Palstra, A. A. Menovsky, and J. A. Mydosh, Phys. Rev. B **33**, 6527 (1986).

[141] M. B. Maple, J. W. Chen, Y. Dalichaouch, T. Kohara, C. Rossel, M. S. Torikachvili, M. W. McElfresh, and J. D. Thompson, Phys. Rev. Lett. **56**, 185 (1986).

[142] H. Amitsuka, M. Sato, N. Metoki, M. Yokoyama, K. Kuwahara, T. Sakakibara, H. Morimoto, S. Kawarazaki, Y. Miyako, and J. A. Mydosh, Phys. Rev. Lett. **83**, 5114 (1999).

[143] N. P. Butch, J. R. Jeffries, S. Chi, J. B. Leão, J. W. Lynn, and M. B. Maple, Phys. Rev. B **82**, 60408 (2010).

[144] K. Matsuda, Y. Kohori, T. Kohara, K. Kuwahara, and H. Amitsuka, Phys. Rev. Lett. **87**, 87203 (2001).

[145] S. Dhar, R. Begum, P. Raj, P. Suryanarayana, L. Gupta, and R. Vijayaraghavan, Solid State Commun. **83**, 965 (1992).

[146] J. G. Park and B. R. Coles, J. Phys.: Condens. Matter **6**, 1425 (1994).

[147] M. Ocko and J.-G. Park, Physica B **230-232**, 71 (1997).

[148] H. Amitsuka, K. Kuwahara, M. Yokoyama, K. Tenya, T. Sakakibara, M. Mihalik, and A. Menovsk, Physica B **281-282**, 326 (2000).

[149] H. Amitsuka, K. Hyomi, T. Nishioka, Y. Miyako, and T. Suzuki, J. Magn. Magn. Mater. **76-77**, 168 (1988).

[150] Y. Dalichaouch, M. Maple, R. Guertin, M. Kuric, M. Torikachvili, and A. Giorgi, Physica B **163**, 113 (1990).

[151] Y. Dalichaouch, M. B. Maple, J. W. Chen, T. Kohara, C. Rossel, M. S. Torikachvili, and A. L. Giorgi, Phys. Rev. B **41**, 1829 (1990).

[152] J. G. Park, J. Phys.: Condens. Matter **6**, 3403 (1994).

[153] S. Elgazzar, J. Rusz, M. Amft, P. M. Oppeneer, and J. A. Mydosh, Nature Mat. **8**, 337 (2009).

[154] K. Momma and F. Izumi, J. Appl. Crystallogr. **44**, 1272 (2011).

[155] W. D. Knight, Phys. Rev. **76**, 1259 (1949).

[156] P. Das, R. E. Baumbach, K. Huang, M. B. Maple, Y. Zhao, J. S. Helton, J. W. Lynn, E. D. Bauer, and M. Janoschek, New J. Phys. **15**, 53031 (2013).

[157] K. Hanzawa, J. Phys. Soc. Jpn. **86**, 44702 (2017).

[158] K. A. Ross, L. Harriger, Z. Yamani, W. J. L. Buyers, J. D. Garrett, A. A. Menovsky, J. A. Mydosh, and C. L. Broholm, Phys. Rev. B **89**, 155122 (2014).

[159] B. M. Huddart, M. T. Birch, F. L. Pratt, S. J. Blundell, D. G. Porter, S. J. Clark, W. Wu, S. R. Julian, P. D. Hatton, and T. Lancaster, J. Phys.: Condens. Matter **31**, 285803 (2019).

[160] G. R. Stewart, Rev. Mod. Phys. **73**, 797 (2001).

[161] R. Zhi-An, L. Wei, Y. Jie, Y. Wei, S. Xiao-Li, Zheng-Cai, C. Guang-Can, D. Xiao-Li, S. Li-Ling, Z. Fang, and Z. Zhong-Xian, Chin. Phys. Lett. **25**, 2215 (2008).

[162] M. Rotter, M. Tegel, and D. Johrendt, Phys. Rev. Lett. **101**, 107006 (2008).

[163] K. Sasmal, B. Lv, B. Lorenz, A. M. Guloy, F. Chen, Y.-Y. Xue, and C.-W. Chu, Phys. Rev. Lett. **101**, 107007 (2008).

[164] N. P. Butch, K. Jin, K. Kirshenbaum, R. L. Greene, and J. Paglione, Proc. Natl. Acad. Sci. U.S.A. **109**, 8440 (2012).

[165] S. Friedemann, T. Westerkamp, M. Brando, N. Oeschler, S. Wirth, P. Gegenwart, C. Krellner, C. Geibel, and F. Steglich, Nat. Phys. **5**, 465 (2009).

[166] J. Custers, P. Gegenwart, C. Geibel, F. Steglich, P. Coleman, and S. Paschen, Phys. Rev. Lett. **104**, 186402 (2010).

[167] B. C. Sales, A. S. Sefat, M. A. McGuire, R. Y. Jin, D. Mandrus, and Y. Mozharivskyj, Phys. Rev. B **79**, 94521 (2009).

[168] S. Rößler, D. Cherian, W. Lorenz, M. Doerr, C. Koz, C. Curfs, Y. Prots, U. K. Rößler, U. Schwarz, S. Elizabeth, and S. Wirth, Phys. Rev. B **84**, 174506 (2011).

[169] E. E. Rodriguez, D. A. Sokolov, C. , M. A. Green, O. Sobolev, J. A. Rodriguez-Rivera, H. Cao, and A. Daoud-Aladine, Phys. Rev. B **88**, 165110 (2013).

[170] J.-X. Zhu, R. Yu, H. Wang, L. L. Zhao, M. D. Jones, J. Dai, E. Abrahams, E. Morosan, M. Fang, and Q. Si, Phys. Rev. Lett. **104**, 216405 (2010).

[171] E. E. McCabe, C. Stock, E. E. Rodriguez, A. S. Wills, J. W. Taylor, and J. S. O. Evans, Phys. Rev. B **89**, 100402 (2014).

[172] C. Stock and E. E. McCabe, J. Phys.: Condens. Matter **28**, 453001 (2016).

[173] B. Keimer, S. A. Kivelson, M. R. Norman, S. Uchida, and J. Zaanen, Nature (London) **518**, 179 (2015).

[174] P. Dai, Rev. Mod. Phys. **87**, 855 (2015).

[175] M. Vojta, Rep. Prog. Phys. **81**, 64501 (2018).

[176] F. Steglich and S. Wirth, Rep. Prog. Phys. **79**, 84502 (2016).

[177] A. Akrap, Y. M. Dai, W. Wu, S. R. Julian, and C. C. Homes, Phys. Rev. B **89**, 125115 (2014).

[178] W. Wu, A. McCollam, I. Swainson, P. M. C. Rourke, D. G. Rancourt, and S. R. Julian, EPL **85**, 17009 (2009).

[179] L. Hollan, Ann. Chim. (Paris) **1**, 437 (1966).

[180] M. A. Nylund, M. Roger, J. Sénateur, and R. Fruchart, Solid State Chem. **4**, 115 (1972).

[181] R. Guérin and M. Sergent, Mater. Res. Bull. **12**, 381 (1977).

[182] I. P. Swainson, W. Wu, A. McCollam, and S. R. Julian, Can. J. Phys. **88**, 701 (2010).

[183] D. G. Raincourt, Hyperfine field fluctuations in the Mössbauer spectrum of magnetic materials: Application to small particles and to the bulk antiferromagnetic $Fe_{(2-x)}Cr_xAs$, Doctoral Thesis, Toronto, 1984.

[184] H. Gretarsson, A. Lupascu, J. Kim, D. Casa, T. Gog, W. Wu, S. R. Julian, Z. J. Xu, J. S. Wen, G. D. Gu, R. H. Yuan, Z. G. Chen, N.-L. Wang, S. Khim, K. H. Kim, M. Ishikado, I. Jarrige, S. Shamoto, J.-H. Chu, I. R. Fisher, and Y.-J. Kim, Phys. Rev. B **84**, 100509 (2011).

[185] L. A. A. Redpath R E, Hopkinson J M and K. H-Y, arXiv:1105.3974 [cond-mat.str-el] (2011).

[186] J. G. Rau and H.-Y. Kee, Phys. Rev. B **84**, 104448 (2011).

[187] A. H. Nevidomskyy and P. Coleman, Phys. Rev. Lett. **103**, 147205 (2009).

[188] Z. P. Yin, K. Haule, and G. Kotliar, Nat. Mater. **10**, 932 EP (2011).

[189] K. W. Plumb, C. Stock, J. A. Rodriguez-Rivera, J.-P. Castellan, J. W. Taylor, B. Lau, W. Wu, S. R. Julian, and Y.-J. Kim, Phys. Rev. B **97**, 184431 (2018).

[190] H. Katsuraki and N. Achiwa, J. Phys. Soc. Jpn **21**, 2238 (1966).

[191] J. Major, J. Mundy, M. Schmolz, A. Seeger, K. P. Döring, K. Fürderer, M. Gladisch, D. Herlach, and G. Majer, Hyperfine Interact. **31**, 259 (1986).

[192] W. L. Wu, A. McCollam, I. P. Swainson, and S. R. Julian, in *Solid Compounds of Transition Elements*, Solid State Phenom., Vol. 170 (Trans Tech Publications Ltd, 2011) pp. 276–281.

[193] F. Xiao, T. Lancaster, P. J. Baker, F. L. Pratt, S. J. Blundell, J. S. Möller, N. Z. Ali, and M. Jansen, Phys. Rev. B **88**, 180401 (2013).

[194] T. Lancaster, S. R. Giblin, G. Allodi, S. Bordignon, M. Mazzani, R. De Renzi, P. G. Freeman, P. J. Baker, F. L. Pratt, P. Babkevich, S. J. Blundell, A. T. Boothroyd, J. S. Möller, and D. Prabhakaran, Phys. Rev. B **89**, 20405 (2014).

[195] T. Lancaster, S. J. Blundell, D. Andreica, M. Janoschek, B. Roessli, S. N. Gvasaliya, K. Conder, E. Pomjakushina, M. L. Brooks, P. J. Baker, D. Prabhakaran, W. Hayes, and F. L. Pratt, Phys. Rev. Lett. **98**, 197203 (2007).

[196] T. Lancaster, F. Xiao, B. M. Huddart, R. C. Williams, F. L. Pratt, S. J. Blundell, S. J. Clark, R. Scheuermann, T. Goko, S. Ward, J. L. Manson, C. Regg, and K. W. Krmer, New J. Phys. **20**, 103002 (2018).

[197] C. Rüegg, K. Kiefer, B. Thielemann, D. F. McMorrow, V. Zapf, B. Normand, M. B. Zvonarev, P. Bouillot, C. Kollath, T. Giamarchi, S. Capponi, D. Poilblanc, D. Biner, and K. W. Krämer, Phys. Rev. Lett. **101**, 247202 (2008).

[198] B. Thielemann, C. Rüegg, K. Kiefer, H. M. Rønnow, B. Normand, P. Bouillot, C. Kollath, E. Orignac, R. Citro, T. Giamarchi, A. M. Läuchli, D. Biner, K. W. Krämer, F. Wolff-Fabris, V. S. Zapf, M. Jaime, J. Stahn, N. B. Christensen, B. Grenier, D. F. McMorrow, and J. Mesot, Phys. Rev. B **79**, 20408 (2009).

[199] M. Klanjšek, H. Mayaffre, C. Berthier, M. Horvatić, B. Chiari, O. Piovesana, P. Bouillot, C. Kollath, E. Orignac, R. Citro, and T. Giamarchi, Phys. Rev. Lett. **101**, 137207 (2008).

[200] T. Lancaster, P. A. Goddard, S. J. Blundell, F. R. Foronda, S. Ghannadzadeh, J. S. Möller, P. J. Baker, F. L. Pratt, C. Baines, L. Huang, J. Wosnitza, R. D. McDonald, K. A. Modic, J. Singleton, C. V. Topping, T. A. W. Beale, F. Xiao, J. A. Schlueter, A. M. Barton, R. D. Cabrera, K. E. Carreiro, H. E. Tran, and J. L. Manson, Phys. Rev. Lett. **112**, 207201 (2014).

[201] A. J. Steele, T. Lancaster, S. J. Blundell, P. J. Baker, F. L. Pratt, C. Baines, M. M. Conner, H. I. Southerland, J. L. Manson, and J. A. Schlueter, Phys. Rev. B **84**, 64412 (2011).

[202] F. L. Pratt, P. J. Baker, S. J. Blundell, T. Lancaster, S. Ohira-Kawamura, C. Baines, Y. Shimizu, K. Kanoda, I. Watanabe, and G. Saito, Nature **471**, 612 (2011).

[203] A. Stoykov, R. Scheuermann, K. Sedlak, J. Rodriguez, U. Greuter, and A. Amato, Physics Procedia **30**, 7 (2012).

[204] A. Zheludev and T. Roscilde, Comptes Rendus Physique **14**, 740 (2013).

[205] S. J. Blundell *et al.*, Unpublished.

[206] B. R. Patyal, B. L. Scott, and R. D. Willett, Phys. Rev. B **41**, 1657 (1990).

[207] R. D. Willett, C. Galeriu, C. P. Landee, M. M. Turnbull, and B. Twamley, *Inorganic Chemistry*, Inorg. Chem. **43**, 3804 (2004).

[208] D. Andreica, N. Cavadini, H. Güdel, F. Gygax, K. Krämer, M. Pinkpank, and A. Schenck, Physica B **289-290**, 176 (2000).

[209] S. Eggert and S. Rommer, Phys. Rev. Lett. **81**, 1690 (1998).

[210] S. Rommer and S. Eggert, Phys. Rev. B **62**, 4370 (2000).

[211] J. A. Chakhalian, R. F. Kiefl, R. Miller, J. Brewer, S. R. Dunsiger, G. Morris, W. A. MacFarlane, J. E. Sonier, S. Eggert, I. Affleck, A. Keren, and M. Verdaguer, Phys. Rev. Lett. **91**, 27202 (2003).

[212] L. Balents, Nature **464**, 199 (2010).

[213] P. Anderson, Mater. Res. Bull. **8**, 153 (1973).

[214] Y. Zhou, K. Kanoda, and T.-K. Ng, Rev. Mod. Phys. **89**, 25003 (2017).

[215] L. Savary and L. Balents, Rep. Prog. Phys. **80**, 16502 (2016).

[216] Y. Shimizu, K. Miyagawa, K. Kanoda, M. Maesato, and G. Saito, Phys. Rev. Lett. **91**, 107001 (2003).

[217] Y. Shimizu, T. Hiramatsu, M. Maesato, A. Otsuka, H. Yamochi, A. Ono, M. Itoh, M. Yoshida, M. Takigawa, Y. Yoshida, and G. Saito, Phys. Rev. Lett. **117**, 107203 (2016).

[218] T. Itou, A. Oyamada, S. Maegawa, M. Tamura, and R. Kato, Phys. Rev. B **77**, 104413 (2008).

[219] T. Isono, H. Kamo, A. Ueda, K. Takahashi, M. Kimata, H. Tajima, S. Tsuchiya, T. Terashima, S. Uji, and H. Mori, Phys. Rev. Lett. **112**, 177201 (2014).

[220] S. Nakatsuji, K. Kuga, K. Kimura, R. Satake, N. Katayama, E. Nishibori, H. Sawa, R. Ishii, M. Hagiwara, F. Bridges, T. U. Ito, W. Higemoto, Y. Karaki, M. Halim, A. A. Nugroho, J. A. Rodriguez-Rivera, M. A. Green, and C. Broholm, Science **336**, 559 (2012).

[221] Y. Ishiguro, K. Kimura, S. Nakatsuji, S. Tsutsui, A. Q. R. Baron, T. Kimura, and Y. Wakabayashi, Nature Comm. **4**, 2022 (2013).

[222] Y. Li, D. Adroja, P. K. Biswas, P. J. Baker, Q. Zhang, J. Liu, A. A. Tsirlin, P. Gegenwart, and Q. Zhang, Phys. Rev. Lett. **117**, 97201 (2016).

[223] Y. Shen, Y.-D. Li, H. Wo, Y. Li, S. Shen, B. Pan, Q. Wang, H. C. Walker, P. Steffens, M. Boehm, Y. Hao, D. L. Quintero-Castro, L. W. Harriger, M. D. Frontzek, L. Hao, S. Meng, Q. Zhang, G. Chen, and J. Zhao, Nature **540**, 559 EP (2016).

[224] X. G. Wen, Phys. Rev. B **39**, 7223 (1989).

[225] X. G. Wen, Phys. Rev. B **44**, 2664 (1991).

[226] G. Baskaran, Z. Zou, and P. Anderson, Solid State Commun. **63**, 973 (1987).

[227] M. C. Gutzwiller, Phys. Rev. **134**, A923 (1964).

[228] M. C. Gutzwiller, Phys. Rev. **137**, A1726 (1965).

[229] A. A. Abrikosov, Physics **2**, 5 (1965).

[230] G. Baskaran and P. W. Anderson, Phys. Rev. B **37**, 580 (1988).

[231] X.-G. Wen, Phys. Rev. B **65**, 165113 (2002).

[232] I. Affleck, Z. Zou, T. Hsu, and P. W. Anderson, Phys. Rev. B **38**, 745 (1988).

[233] X.-G. Wen, *Quantum field theory of many-body systems: from the origin of sound to an origin of light and electrons* (Oxford University Press, Oxford, 2007).

[234] S. A. Kivelson, D. S. Rokhsar, and J. P. Sethna, Phys. Rev. B **35**, 8865 (1987).

[235] N. Read and S. Sachdev, Phys. Rev. B **42**, 4568 (1990).

[236] T. Senthil and M. P. A. Fisher, Phys. Rev. B **62**, 7850 (2000).

[237] F. Jellinek, J. Less-Common Met. **4**, 9 (1962).

[238] J. Wilson, F. D. Salvo, and S. Mahajan, Adv. Phys. **24**, 117 (1975).

[239] A. Spijkerman, J. L. de Boer, A. Meetsma, G. A. Wiegers, and S. van Smaalen, Phys. Rev. B **56**, 13757 (1997).

[240] P. Fazekas and E. Tosatti, Philosophical Magazine B **39**, 229 (1979).

[241] K. Rossnagel, J. Phys.: Condens. Matter **23**, 213001 (2011).

[242] P. Darancet, A. J. Millis, and C. A. Marianetti, Phys. Rev. B **90**, 45134 (2014).

[243] M. Bovet, S. van Smaalen, H. Berger, R. Gaal, L. Forró, L. Schlapbach, and P. Aebi, Phys. Rev. B **67**, 125105 (2003).

[244] J. K. Freericks, H. R. Krishnamurthy, Y. Ge, A. Y. Liu, and T. Pruschke, physica status solidi (b) **246**, 948 (2009).

[245] A. S. Ngankeu, S. K. Mahatha, K. Guilloy, M. Bianchi, C. E. Sanders, K. Hanff, K. Rossnagel, J. A. Miwa, C. Breth Nielsen, M. Bremholm, and P. Hofmann, Phys. Rev. B **96**, 195147 (2017).

[246] S.-H. Lee, J. S. Goh, and D. Cho, Phys. Rev. Lett. **122**, 106404 (2019).

[247] K. T. Law and P. A. Lee, Proc. Natl. Acad. Sci. U.S.A **114**, 6996 (2017).

[248] M. Kratochvilova, A. D. Hillier, A. R. Wildes, L. Wang, S.-W. Cheong, and J.-G. Park, npj Quantum Materials **2**, 42 (2017).

[249] W.-Y. He, X. Y. Xu, G. Chen, K. T. Law, and P. A. Lee, Phys. Rev. Lett. **121**, 46401 (2018).

[250] M. Klanjšek, A. Zorko, R. Žitko, J. Mravlje, Z. Jagličić, P. K. Biswas, P. Prelovšek, D. Mihailovic, and D. Arčon, Nature Physics **13**, 1130 EP (2017).

[251] T. Ishiguro and H. Sato, Phys. Rev. B **44**, 2046 (1991).

[252] D. C. Miller, S. D. Mahanti, and P. M. Duxbury, Phys. Rev. B **97**, 45133 (2018).

[253] N. Govind, M. Petersen, G. Fitzgerald, D. King-Smith, and J. Andzelm, Comput. Mater. Sci **28**, 250 (2003).

[254] A. Ribak, I. Silber, C. Baines, K. Chashka, Z. Salman, Y. Dagan, and A. Kanigel, Phys. Rev. B **96**, 195131 (2017).

[255] M. A. Butler, L. R. Walker, and Z. G. Soos, J. Chem. Phys. **64**, 3592 (1976).

[256] F. L. Pratt, S. J. Blundell, T. Lancaster, C. Baines, and S. Takagi, Phys. Rev. Lett. **96**, 247203 (2006).

[257] F. L. Pratt, J. Phys.: Condens. Matter **16**, S4779 (2004).

[258] C. Bonhomme, C. Gervais, F. Babonneau, C. Coelho, F. Pourpoint, T. Azaïs, S. E. Ashbrook, J. M. Griffin, J. R. Yates, F. Mauri, and C. J. Pickard, Chem. Rev. **112**, 5733 (2012).

[259] A. V. Chubukov, S. Sachdev, and T. Senthil, Nucl. Phys. B **426**, 601 (1994).

[260] C. Xu and S. Sachdev, Phys. Rev. B **79**, 64405 (2009).

[261] Y. Qi, C. Xu, and S. Sachdev, Phys. Rev. Lett. **102**, 176401 (2009).

[262] C. P. Nave and P. A. Lee, Phys. Rev. B **76**, 235124 (2007).

[263] T. Senthil, M. Vojta, and S. Sachdev, Phys. Rev. B **69**, 35111 (2004).

[264] C. J. Butler, M. Yoshida, T. Hanaguri, and Y. Iwasa, arXiv:1908.08221 [cond-mat.str-el] (2019).

[265] S.-S. Lee, P. A. Lee, and T. Senthil, Phys. Rev. Lett. **98**, 67006 (2007).

[266] V. Galitski and Y. B. Kim, Phys. Rev. Lett. **99**, 266403 (2007).

[267] T. J. Hicken, private communication (2019).

[268] T. Lancaster, R. C. Williams, I. O. Thomas, F. Xiao, F. L. Pratt, S. J. Blundell, J. C. Loudon, T. Hesjedal, S. J. Clark, P. D. Hatton, M. Ciomaga Hatnean, D. S. Keeble, and G. Balakrishnan, Phys. Rev. B **91**, 224408 (2015).

[269] D. Marx and M. Parrinello, J. Chem. Phys. **104**, 4077 (1996).

[270] M. Gomilšek, private communication (2019).

[271] G. M. Luke, Y. Fudamoto, K. M. Kojima, M. I. Larkin, J. Merrin, B. Nachumi, Y. J. Uemura, Y. Maeno, Z. Q. Mao, Y. Mori, H. Nakamura, and M. Sigrist, Nature **394**, 558 (1998).

[272] A. D. Hillier, J. Quintanilla, and R. Cywinski, Phys. Rev. Lett. **102**, 117007 (2009).

[273] R. P. Singh, A. D. Hillier, B. Mazidian, J. Quintanilla, J. F. Annett, D. M. Paul, G. Balakrishnan, and M. R. Lees, Phys. Rev. Lett. **112**, 107002 (2014).

[274] J. Xia, Y. Maeno, P. T. Beyersdorf, M. M. Fejer, and A. Kapitulnik, Phys. Rev. Lett. **97**, 167002 (2006).

[275] M. Sigrist and K. Ueda, Rev. Mod. Phys. **63**, 239 (1991).